UNIVERSITÀ DEGLI STUDI DELL'INSUBRIA

Facoltà di Scienze Matematiche, Fisiche e Naturali

Dottorato di Ricerca in Astronomia e Astrofisica

Exploring accretion theory with a new subclass of High Mass X-ray Binaries: interpretation of *INTEGRAL* observations of the Supergiant Fast X-ray Transients

Supervisor:
Dott.ssa Lara SIDOLI (INAF-IASF Milano)

Tesi di Dottorato di:
Lorenzo DUCCI
Matr. 708042

Codice P.A.C.S.: 97.80.Jp

XXIII ciclo

This thesis is based on work performed at the
Istituto di Astrofisica Spaziale e Fisica Cosmica (IASF) of Milan,
between October 2007 and September 2010.

Contents

Introduction

In the last eight years the Galactic plane monitoring performed by the *INTErnational Gamma-Ray Astrophysics Laboratory (INTEGRAL)*, launched in 2002, has allowed to discover many new hard X-ray sources (Bird et al. 2010). In particular, almost 10% of the new discovered sources are *High Mass X-ray Binaries (HMXBs)*, which were not detected in earlier observations. Among these, *INTEGRAL* discovered several new sources associated with OB supergiants, undetectable for long periods of time, which occasionally exhibit short flares (with duration of a few hours) reaching luminosities of $10^{36} - 10^{37}$ erg s^{-1}. The fast X-ray transient behaviour of these sources, remarkably different from the classical HMXBs with supergiant companions (which are bright persistent sources), led to establish the existence of a new class of X-ray binaries called *Supergiant Fast X-ray Transients (SFXTs)* (Sguera et al. 2005; Negueruela et al. 2006a). SFXTs display an high dynamic range, spanning 3-5 orders of magnitude from a quiescent luminosity of 10^{32} erg s^{-1} up to the peak luminosity, and they spend most of the time in an intermediate flaring level of emission at around $10^{33} - 10^{34}$ erg s^{-1}. Up to now, there are nine confirmed members in the class of SFXTs and several candidates. Seven are the SFXTs displaying orbital periodicity ranging from ~ 3.32 days (IGR J16479-4514) up to ~ 165 days (IGR J11215-5952).

Different mechanisms have been proposed to explain the peculiar SFXT behaviour.

in't Zand (2005) proposed that the SFXTs flares are produced by the accretion of dense blobs of matter from the companion wind. Sidoli et al. (2007) proposed that the outbursts are due to the presence of an equatorial wind component, denser than the spherically symmetric wind from the supergiant. If this wind component is inclined with respect to the orbital plane of the system, when the compact object crosses it, there is enhanced accretion and an outburst is triggered. Another possibility involves the onset of gated mechanisms where the accretion is halted because of the presence of a magnetic or a centrifugal barrier (Grebenev & Sunyaev 2007; Bozzo et al. 2008a).

The aim of this thesis is to gain more informations about the peculiar transient behaviour of SFXTs and to explore the accretion mechanisms involved in these enigmatic X-ray sources.

The first two Chapters of this thesis provide a brief review of the current knowledge on High Mass X-ray Binaries (Chapter 1) and Supergiant Fast X-ray Transients (Chapter 2).

In Chapter 3 I briefly describe the main characteristics of the instruments on board the *INTEGRAL* satellite used to observe many of the HMXBs studied in this thesis.

In Chapter 4 I present a new clumpy wind model for OB supergiants, with both spherical and non-spherical geometry, that I have developed to investigate the effects of accretion from a clumpy wind on the X-ray variability of SFXTs. I assumed that the clumps are confined by ram pressure of the ambient gas, and I assumed for the first time that a fraction of the stellar wind is in form of clumps with power law mass and radius distributions. I found that clump size increases with the distance from the supergiant star, then for each mass of the clump, I derived the upper-limit and the lower-limit for the clump radius. I computed the expected X-ray lightcurves in the framework of the Bondi-Hoyle accretion theory, modified to take into account the presence of clumps, then I explored different distributions for mass and radius of the clumps. The resulting variability properties are found to depend not only on the assumed orbital parameters, but also on the wind characteristics. I have then applied this model to reproduce the X-ray lightcurves of four representative HMXBs: two persistent supergiant systems (Vela X-1 and 4U 1700-377), the SFXTs IGR J11215-5952 and IGR J18483-0311. The model can reproduce the observed lightcurves well, but requiring in all cases an overall mass loss from the supergiants about a factor 3-10 smaller than the values inferred from UV lines studies that assume homogeneous wind, but in agreement with recent studies that assume clumpy winds (Lépine & Moffat 2008; Hamann et al. 2008).

In Chapter 5 I report the systematic analysis of all *INTEGRAL* observations from 2003 to 2009 of 14 SFXTs (confirmed and candidates), implying a net exposure time of about 30 Ms. This analysis led to discover several new outbursts from SFXTs, and has allowed to discuss the emerging X-ray behaviour of IGR J16479-4514 in the framework of the clumpy wind model presented in Chapter 4. I discussed the effects of X-ray photoionization on the accretion in close binary systems such as IGR J16479-4514 and IGR J17544-2619. Then, I have applied the accretion model of Ho & Arons (1987), that I have partly modified, to IGR J16479-4514, discovering that, because of X-ray photoionization, there is a high probability of formation of transient accretion disks from the capture of angular momentum in this source. This result suggests that the formation of transient accretion disks could be responsible for the flaring activity in SFXTs with narrow orbits or in SFXTs with higher orbital periods and high eccentricities, when the neu-

tron star is close to periastron. I also proposed an alternative way to explain the origin of flares with peculiar shapes observed with *INTEGRAL* applying the intermittent accretion model of Lamb et al. (1977), originally proposed to explain Type II bursts. The *INTEGRAL* analysis of these SFXTs has allowed to place constraints on the total population number of SFXTs in our Galaxy.

In Chapter 6 I report the study of the candidate SFXT IGR J16418-4532, for which I obtained a refined estimate of the orbital period from *Swift*/BAT data, and I confirmed the presence of a region of the orbital lightcurve with a low flux, probably due to an eclipse, or due to the onset of the centrifugal inhibition of accretion. Then I found a spin period of $P_{\rm spin} = 1213.5 \pm 1$ s in the IBIS/ISGRI lightcurve (15-40 keV) of this source, improving the previous estimate obtained by Walter et al. (2006) ($P_{\rm spin} = 1246 \pm 100$ s). The uncertainties of the results from infrared observations performed by (Rahoui et al. 2008; Chaty et al. 2008) do not allow an assessment of the spectral class of the counterpart of IGR J16418-4532, which could be a main sequence, giant, or O8.5 supergiant. From considerations involving the expected X-ray luminosities, the duration of the likely eclipse, and the onset of the centrifugal inhibition of accretion, I found that in all these cases it is possible to exclude the presence of a O8.5 V star, and the presence of a supergiant is favoured.

Chapter 1

High Mass X-ray binaries

1.1 X-ray binaries classification

The X-ray binaries are composed by a compact object (a neutron star or a black hole) and a companion star which transfers matter onto the compact object. They are usually divided in two classes, depending on the mass of the companion star:

- *High Mass X-ray Binaries (HMXBs)*: the companion star is massive, $M \geq 10 M_{\odot}$ (spectral types O-B, of main sequence, giant or supergiant), and belongs to population I. The compact object is a neutron star or a black hole. HMXBs are usually located along the Galactic plane, in particular along the spiral arms, where there is an high rate of star formation. HMXBs have a low galactic latitude $< |b| > \approx 2 - 3°$. Based on evolutionary considerations Dalton & Sarazin (1995) estimated that there are $\geq 10^3$ HMXBs in the Galaxy, and the majority of them are inactive.

- *Low Mass X-ray Binaries (LMXBs)*: the companion star has a mass of $M \lesssim 1 M_{\odot}$, and belongs to the stars of population II. Sometimes can be a white dwarf. The compact object can be a neutron star or a black hole. LMXBs have a galactic latitude interval of $< |b| > \approx 10°$, and they are highly concentrated at the Galactic center. Moreover, they have been observed in several globular clusters.

1.2 Accretion physics

A particle of the gas with mass m infalling into a point mass potential

$$\Phi = -\frac{G M_{\rm x} m}{R_{\rm x}}$$

from a distance R_0 to a distance $R_{\rm x}$, converts gravitational into kinetic energy, by an amount $\Delta\Phi = GM_{\rm x}m(1/R_{\rm x} - 1/R_0)$. Assuming that the starting distance is large, $\Delta\Phi = GM_{\rm x}m/R_{\rm x}$, the speed of arrival (the *free-fall speed*) $v_{\rm ff}$, is given by:

$$\frac{1}{2}mv_{\rm ff}^2 = \frac{GM_{\rm x}m}{R_{\rm x}} \ .$$

When the gas is brought to rest at the surface of a star, the amount of energy ΔE dissipated is:

$$\Delta E = \frac{1}{2}mv_{\rm ff}^2 = \frac{GM_{\rm x}m}{R_{\rm x}} \ .$$

If, instead, it goes into a circular Kepler orbit at distance $R_{\rm x}$:

$$\Delta E = \frac{1}{2}\frac{GM_{\rm x}m}{R_{\rm x}} \ .$$

The dissipated energy may go into internal energy of the gas, and into radiation which escapes to infinity (usually in the form of photons, but neutrino losses can also play a role in some cases). The luminosity given by the accretion of a particle is:

$$L_{\rm x} \approx \frac{GM}{r}\dot{m} \tag{1.1}$$

From Equation (1.1), the formula for the *accretion luminosity* is:

$$L_{\rm x} \approx \frac{GM_{\rm x}}{R_{\rm x}}\dot{M}_{\rm acc} \tag{1.2}$$

where $\dot{M}_{\rm acc} = \sum_{i=1}^{n} \dot{m}_i$ is the accretion rate, given by the sum of the accretion rate of n particles.

For a solar mass neutron star the accretion has an efficiency of:

$$\varepsilon = \frac{L_{\rm x}}{\dot{M}_{\rm acc}c^2} \approx 0.15 \ . \tag{1.3}$$

The efficiency in the conversion of a rest mass in energy in nuclear fusion reactions in the Sun (burning of hydrogen to helium) is ≈ 0.007. Hence, in neutron stars and black holes the accretion is more efficient than nuclear burning by a factor ≈ 20.

1.2.1 The Eddington luminosity

Eddington luminosity is the maximum luminosity which a spherically symmetric source of mass $M_{\rm x}$ can emit in a steady state, and it results from the balance between the inward force of gravity and the outward radiation

pressure. The inward gravitational force acting on an electron-proton pair at distance r from the compact object is:

$$f_{\rm grav} = \frac{GM_{\rm x}}{r^2}(m_{\rm p} + m_{\rm e}) \simeq \frac{GM_{\rm x}m_{\rm p}}{r^2} \tag{1.4}$$

where $m_{\rm p}$ and $m_{\rm e}$ are the proton and electron masses, respectively. The radiation pressure is provided by Thomson scattering. The radiation force acting on the electron is given by:

$$f_{\rm rad} = \sigma_{\rm Th} N_{\rm ph} p \tag{1.5}$$

where $\sigma_{\rm Th}$ is the Thomson scattering cross-section, $N_{\rm ph}$ is the flux of photons, $p = \hbar\nu/c$ is the momentum given by each photon to the electron in each collision. The flux of photons at distance r from the source is:

$$N_{\rm ph} = \frac{L_{\rm x}}{4\pi r^2 \hbar\nu} \tag{1.6}$$

where $L_{\rm x}$ is the source luminosity. Equating the gravitational force (Equation 1.4) and the radiation force (Equation 1.5) and taking into account the Equation (1.6), it is possible to obtain the Eddington luminosity $L_{\rm E}$:

$$L_{\rm E} = \frac{4\pi G M_{\rm x} m_{\rm p} c}{\sigma_{\rm Th}} \simeq 1.3 \times 10^{38} \left(\frac{M}{M_\odot}\right) \text{ erg/s} \, . \tag{1.7}$$

The Eddington luminosity can be also interpreted as a mass accretion limit:

$$\dot{M}_{\rm Edd} = \frac{4\pi r m_{\rm p} c}{\sigma_{\rm Th}} \simeq 1.5 \times 10^{-8} \ {\rm M}_\odot \ {\rm yr}^{-1} \, . \tag{1.8}$$

In case of helium atmosphere, the radiation pressure acts on two free electrons; then, the electrons communicate the radiation force to the helium nucleus (with four times the mass of a proton) by means of the electrostatic force. Thus, twice the usual Eddington luminosity would be needed to drive off an atmosphere of pure He (Tauris & van den Heuvel 2003; Longair 1994).

1.3 Accretion from stellar wind and accretion disks

There are two main mechanisms for the transfer of matter in X-ray binaries (Figure 1.1):

1. **Stellar wind accretion**: the companion star of the compact object may, at some evolutionary phase, eject much of its mass in the form of a stellar wind; some of this material will be captured gravitationally by the compact object;

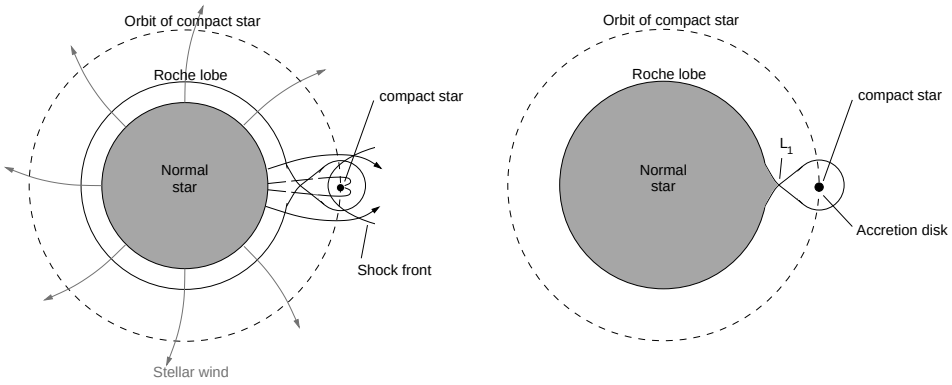

Figure 1.1: Illustration of the two ways in which accretion onto stars in binary systems may take place. *Left panel*: the primary star has a strong stellar wind and the neutron star is embedded in the strong outflow from the primary. *Right panel*: the primary fills its Roche lobe and matter passes from the primary to the secondary star through the Lagrangian point L_1. In this case an accretion disk forms around the compact star.

2. **Roche Lobe overflow**: in the course of its evolution, the companion star of the compact object may increase in radius, or the binary separation shrink, to the point where the gravitation of the compact object remove the outer layers of the envelope of the companion star. In this framework, the compact object accretes from an accretion disk; however, at the same time, the compact object may accrete the stellar wind emitted by the companion star.

1.3.1 Stellar wind accretion

The accretion from a stellar wind is particularly relevant for systems containing an OB star (main sequence or supergiant). The stellar wind of these stars is intense, with mass loss rates of $\dot{M} \approx 10^{-6} - 10^{-7}$ $M_\odot$ yr^{-1} and highly supersonic, with velocity of $v_w \approx 1700 - 2000$ km s^{-1} (see Section 1.3.2). The accretion in these X-ray binary systems can be described with the Bondi-Hoyle-Lyttleton accretion theory, originally developed by Hoyle & Lyttleton (1939) to explain the Earth's climatic variations with the possible change in luminosity of the Sun due to its passage through an interstellar cloud. This theory, further developed by Bondi (1952), can be applied to the case of a neutron star accreting matter from the companion wind.

In the framework of the Bondi-Hoyle-Lyttleton accretion theory, the gravity of the compact object focuses the flow as shown in Figure 1.2. Following Edgar (2004), a streamline with impact parameter ζ follows a ballistic orbit if pressure effects are negligible. Thus, the equations of the streamline

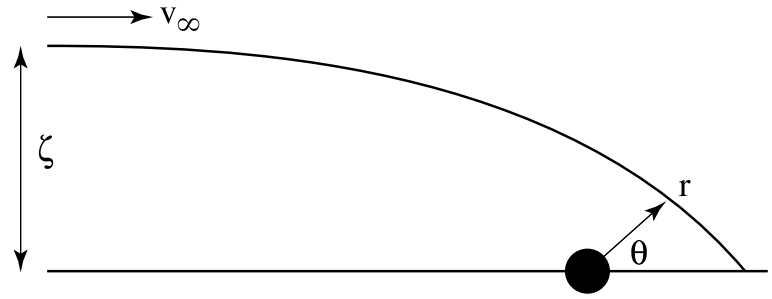

Figure 1.2: Schematic representation of the Bondi-Hoyle-Lyttleton accretion geometry (Edgar 2004).

in the radial and polar directions are:

$$\ddot{r} - r\dot{\theta}^2 = -\frac{GM_{\rm x}}{r^2} \tag{1.9}$$

$$r^2\dot{\theta} = \zeta v_\infty \ . \tag{1.10}$$

Setting $h = \zeta v_\infty$ and making the substitution $u = 1/r$, Equation (1.9) can be written as:

$$\frac{d^2u}{d\theta^2} + u = \frac{GM_{\rm x}}{h^2} \ . \tag{1.11}$$

The general solution of Equation (1.11) is $u = A\cos\theta + B\sin\theta + C$, where A, B, C are arbitrary constants. The substitution of this general solution into Equation (1.9) shows that $C = GM_{\rm x}/h^2$. The values of A and B are fixed by the boundary conditions:

$$\begin{aligned} u &\overset{\theta\to\pi}{\longrightarrow} 0 \\ \dot{r} = -h\frac{du}{d\theta} &\overset{\theta\to\pi}{\longrightarrow} -v_\infty \end{aligned}$$

which are satisfied by:

$$u = \frac{GM_{\rm x}}{h^2}(1+\cos\theta) - \frac{v_\infty}{h}\sin\theta \ . \tag{1.12}$$

When the flow encounters the $\theta = 0$ axis, its θ-velocity goes to zero. Therefore, from Equation 1.12, the radius of the streamline results to be $r = h^2/(2GM_{\rm x})$. Only the material bound to the star can be accreted:

$$\frac{1}{2}v_\infty^2 - \frac{GM_{\rm x}}{r} < 0$$

which can be rewritten as follows:

$$\zeta < \zeta_{\rm HL} = \frac{2GM_{\rm x}}{v_\infty^2} \ . \tag{1.13}$$

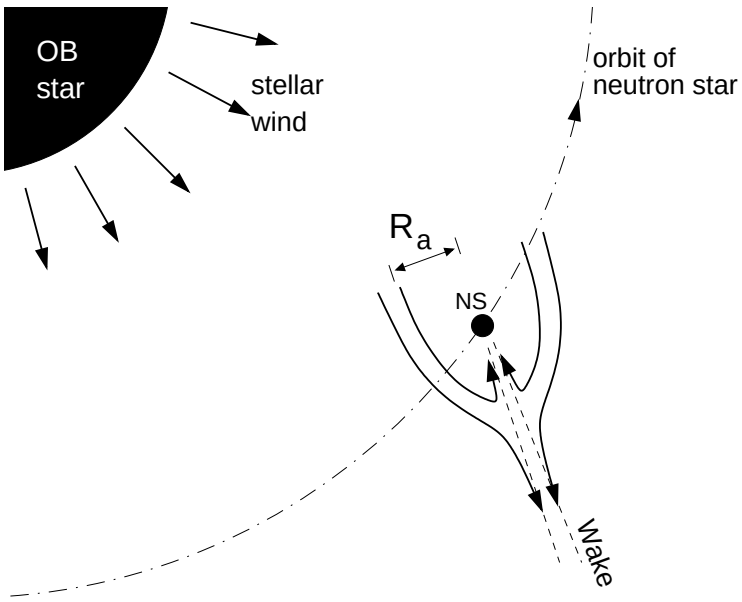

Figure 1.3: Streamlines of stellar wind material, relative to an accreting neutron star.

Equation (1.13) defines the critical impact parameter, known as the Hoyle-Lyttleton radius. Material with an impact parameter smaller than this value will be accreted.

Now consider a neutron star accreting mass from the stellar wind of the companion star. We assume that the companion star loses mass in the form of a steady, homogeneous and sperically symmetric wind, with a mass loss rate $\dot{M}$ given by:

$$\dot{M} = 4\pi r^2 \rho(r) v_{\rm w}(r) \tag{1.14}$$

where $v_{\rm w}$ and ρ are the stellar wind velocity and the mass density at a distance r from the companion star, respectively. Only matter within a distance smaller than the *accretion radius* $R_{\rm acc}$ is accreted (see Equation 1.13 and Figure 1.3):

$$R_{\rm acc} = \frac{2GM_{\rm x}}{v_{\rm rel}^2(r) + c_{\rm s}^2} \tag{1.15}$$

where $M_{\rm x}$ is the neutron star mass, $c_{\rm s}$ is the sound velocity through the wind, $v_{\rm rel}(r)$ is the relative velocity between the neutron star and the wind:

$$v_{\rm rel} = \sqrt{(v_{\rm w} - v_{\rm r})^2 + (v_{\rm rot,w} - v_\phi)^2} \tag{1.16}$$

where $v_{\rm r}$ and v_ϕ are the radial and tangential components of the orbital velocity, $v_{\rm w}$ and $v_{\rm rot,w}$ are the radial and tangential components of the wind velocity. The tangential velocity $v_{\rm rot,w}$ can be neglected in winds of OB

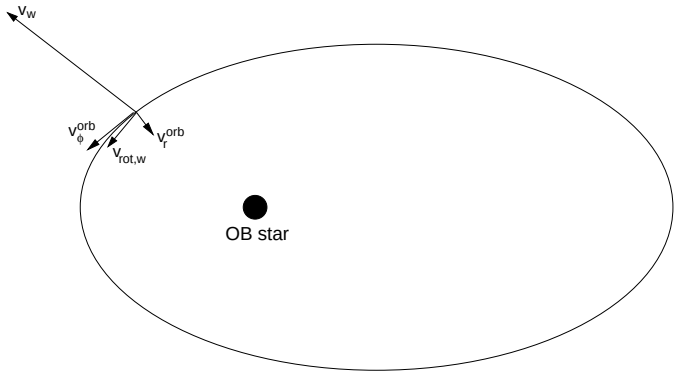

Figure 1.4: The different velocity components that constitute the relative wind velocity with respect to the neutron star. The wind velocity consists of a radial component $v_{\rm w}$, and a rotational component $v_{\rm rot,w}$ due to the rapid rotation of the companion star. The orbital velocity has a radial $v_{\rm r}$ and a tangential v_ϕ component.

supergiants because of the low rotational velocity of these stars. On the contrary, $v_{\rm rot,w}$ becomes important in Be/X-ray binary systems, where the rotational velocity of Be star (of the order of $\approx 10^2$ km s^{-1}, Waters et al. 1989) cannot be neglected. The different velocity components are explained in Figure 1.4.

In the framework of the Bondi-Hoyle accretion theory, the mass accretion rate $\dot{M}_{\rm acc}$ depends on the accretion radius $R_{\rm acc}$ and can be expressed with the equation:

$$\dot{M}_{\rm acc} = \rho v_{\rm rel} \pi R_{\rm acc}^2 \tag{1.17}$$

where $\rho v_{\rm rel}$ is the flux of the wind at a distance r from the OB star, and $\pi R_{\rm acc}^2$ is the accretion "cross section" of the compact object (Waters et al. 1989).

From Equations (1.2), (1.14), (1.15), and (1.17) it is possible to obtain the X-ray luminosity for wind-fed HMXBs:

$$L_{\rm x} = \frac{(GM_{\rm x})^3}{R_{\rm x}} \frac{\dot{M}}{r^2 v_{\rm rel}^3 v_{\rm w}} \tag{1.18}$$

where $M_{\rm x}$ and $R_{\rm x}$ are the mass and the radius of the compact object. The wind velocity is not constant with r, but follows the β-velocity law (Equation 1.28).

In addition, other structures in the stellar wind are expected because of the presence of the X-rays originating from the compact object and the compact object itself (see Figure 1.5):

- the **photoionization wake**, originated by the collisions between the undisturbed radiation-driven wind and the highly ionized plasma around

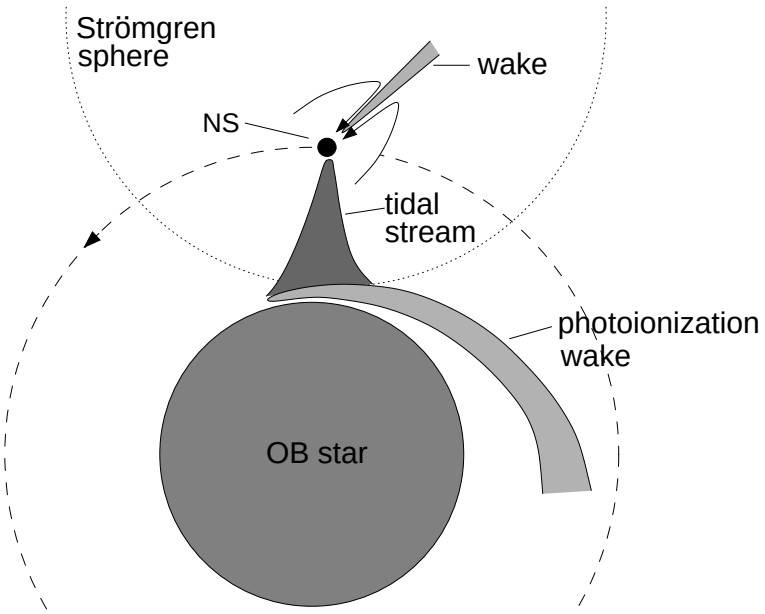

Figure 1.5: Schematic representation of the different structures in the stellar wind of a HMXBs. X-ray observations indicate the presence of an accretion wake, a possible tidal stream, a photoionization wake, and the Strömgren sphere.

the compact object, which result in strong shocks and creation of dense sheets of gas trailing the X-ray source (see Fransson & Fabian 1980; Kaper, Hammerschlag-Hensberge, & Zuiderwijk 1994).

The presence of a photoionization wake has been proposed to explain the presence of absorption components (in optical spectra of several X-ray binaries) which exhibit variations linked to the binary phase, and orbit-to-orbit variations.

Moreover, X-ray observations show an increase in the hardness ratio when the compact object is approaching the eclipse by the supergiant (see e.g. Haberl & White 1990): the increase of the hardness ratio is due to the partial absorption of the emitted soft X-ray photons by regions of higher density (i.e. the photoionization wake) in the line of sight towards the X-ray source.

- a gas **stream** that leaves the donor star at the side of the compact object and that is formed by tidal interactions between the two components of the binary system.

  The presence of a gas stream was originally proposed by Stevens (1988) to explain the transient X-ray emission of the Be/X-ray binary system A0538-66. Stevens (1988) argued that the spherically symmetric

models previously proposed to reproduce the recurrent X-ray transient behaviour of neutron stars in HMXBs did not account for the effects of the neutron star on the stellar wind. Then, he modified the Castor, Abbott, & Klein (1975) line-driven wind model to include the effects of the neutron star on the stellar wind, and he found that when the neutron star is close to periastron, the mass-loss rate of the donor star in the direction toward the neutron star can be enhanced by a factor of up to 200. Stevens (1988) proposed that this stream could be the responsible of large orbital variations in the X-ray flux.

Recently the stream model has been succesfully applied to explain the peculiar X-ray lightcurve of the HMXB GX 301-2 (Leahy 2002; Leahy & Kostka 2008).

1.3.2 Line driven winds

Hot stars emit the bulk of their radiation in the UV. The radiative acceleration in the winds of hot stars[1] is provided mainly by the absorption and re-emission of UV photons in the resonance lines of ions of abundant elements such as C, N, O, Ne, Si, P, S, and Fe-group elements. For this reason the winds of luminous hot stars are called *line driven winds*.

The ions which provide the dominant radiative acceleration in the winds of hot stars constitute about 10^{-5} of all ions by number and 10^{-4} by mass. In fact, the majority of the ions contribute very little to the radiative acceleration because they are fully ionized (e.g. H and He), or the strongest lines are in the extreme UV where the stellar flux is small.

The momentum gained by the ions most involved in the absorption and re-emission of UV photons is shared by the surrounding field particles (protons, helium ions and electrons) by means of Coulomb interactions with the field particles, producing a steady outflow.

The radiation force on ions would not be efficient in driving a stellar wind if it were not for the Doppler effect. In a static atmosphere, the radiation from the photosphere of the star is absorbed or scattered in the lower layers of the atmosphere, and the outer layers do not receive direct radiation from the photosphere at the wavelength of the line. This leads to a reduction of the radiative acceleration in the outer layers of the atmosphere. If the outer atmosphere is moving outward, because of its velocity gradient, the atoms in the atmosphere see the radiation from the photosphere as redshifted. Hence, the atoms in the outer atmosphere can absorb a not attenuated radiation from the photosphere. The Doppler shift thus allows the atoms to absorb undiminished continuum photons in their line transitions. This makes the radiative acceleration due to spectral lines in the atmospheres

[1]The radiative acceleration caused by spectral lines drives the winds of many different types of stars: main-sequence stars, giant and supergiants of type O, B, A, and central stars of planetary nebulae.

of hot luminous stars very efficient in driving a stellar wind (Castor et al. 1975).

The force due to spectral lines in stellar winds is the result of the contribution from a large number of lines. For any given spectral line, the radiative acceleration due to the absorption of the stellar radiation depends on the flux F_ν of the incoming radiation and on the optical depth. The flux of the stellar radiation at some distance r from the star depends on the flux emitted at the photosphere and on the absorption between the photosphere and a point at distance r. Castor et al. (1975) introduced the 'dimensionless optical depth parameter" t, which is independent of the line strength, and depends only on the structure of the wind (i.e. proportional to $\rho(dv/dr)$). t is related to the line optical depth $\tau_{\rm L}$ by:

$$t = \frac{\sigma_{\rm e}}{\kappa_{\rm L}} \tau_{\rm L}$$

where $\sigma_{\rm e}$ is the electron scattering opacity ($\sigma_{\rm e} = \sigma_{\rm Th}/(\mu_{\rm e} m_{\rm H}) \approx 0.34\,{\rm cm^2\ g^{-1}}$), and $\kappa_{\rm L}$ is the line opacity. In the static atmosphere, t is given by:

$$t \equiv \int_r^\infty \sigma_{\rm e} \rho dr \tag{1.19}$$

and in the expanding atmosphere by:

$$t \equiv \sigma_{\rm e}^{\rm ref} v_{\rm th} \rho (dr/dv) \tag{1.20}$$

where $\sigma_{\rm e}^{\rm ref} = 0.325\ {\rm cm^2\ g^{-1}}$ is a reference value for the electron scattering opacity (Abbott 1982), and the velocity $v_{\rm th}$ is the mean thermal velocity of the protons (with mass $m_{\rm H}$) in a wind with a temperature equal to the effective temperature of the star $T_{\rm eff}$:

$$v_{\rm th} = \sqrt{\frac{2 k_{\rm B} T_{\rm eff}}{m_{\rm H}}} \tag{1.21}$$

$k_{\rm B}$ is the Boltzmann constant.

The total radiative acceleration $g_{\rm L}$ due to all spectral lines is calculated by summing the contributions of all individual lines. This requires the computation of the degree of ionization and excitation for large numbers of energy levels for many different elements (Abbott 1982; Pauldrach et al. 1986; Shimada et al. 1994). These calculations allow to approximate $g_{\rm L}$ to an accuracy of 10% by the function:

$$g_{\rm L} \equiv g_{\rm e} \mathcal{M}(t) \tag{1.22}$$

where $g_{\rm e}$ is the radiative acceleration due to electron scattering (for the reference value of $\sigma_{\rm e}^{\rm ref}$):

$$g_{\rm e} \equiv \frac{\sigma_{\rm e}^{\rm ref} F}{c} = \frac{\sigma_{\rm e}^{\rm ref} L_*}{4\pi r^2 c}\ , \tag{1.23}$$

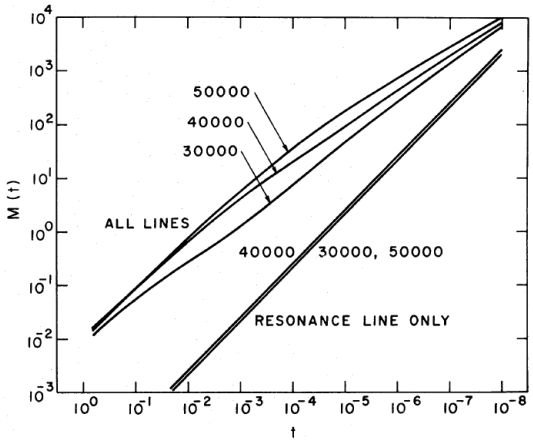

Figure 1.6: The ordinate is the force multiplier $\mathcal{M}(t)$, and the abscissa is the optical depth parameter t. The curves labeled "all lines" were computed by Castor et al. (1975) using 900 multiplets of CIII; the curves "resonance line only" included just the CIII resonance line $\lambda = 977$ nm. $\mathcal{M}(t)$ was computed for three temperature, as indicated in the figure (Castor et al. 1975).

L_* is the luminosity of the star, and $\mathcal{M}(t)$ is the *force multiplier*:

$$\mathcal{M}(t) = kt^{-\alpha}\left(10^{-11}\frac{n_e}{W}\right)^{\delta} \tag{1.24}$$

where the quantities k, α, δ are called *force multiplier parameters*, n_e is the electron density, and $W(r)$ is the geometrical dilution factor:

$$\begin{aligned} W(r) &= \frac{1}{2}\left[1-\sqrt{1-\left(\frac{R_*}{r}\right)^2}\right] \\ &= \left(\frac{R_*}{2r}\right)^2 \quad \text{if} \quad r \gg R_* \end{aligned} \tag{1.25}$$

where R_* is the radius of the hot star. $\mathcal{M}(t)$ depends on the chemical composition and on the ionization and excitation in the wind. The ionization depends on the stellar radiation, i.e. on T_eff and on the parameter n_e/W. This is because the photoionization rate depends on the flux of the star at distance r, which is proportional to $W(r)$, whereas the recombination rate depends on the electron density.

The values of $\mathcal{M}(t)$ calculated by Castor et al. (1975) are plotted in Figure 1.6 as a function of t.

The radiative acceleration due to lines (Equation 1.22) can thus be written as:

$$g_\mathrm{L} = \frac{\sigma_\mathrm{e}^\mathrm{ref} L_*}{4\pi c r^2} kt^{-\alpha}\left(10^{-11}\frac{n_\mathrm{e}}{W}\right)^{\delta} . \tag{1.26}$$

The values of the force multiplier parameters of Abbott (1982) and Shimada et al. (1994) are for solar abundances. The force multiplier depends on the metallicity[2] Z as $Z^{1.0}$:

$$\mathcal{M}(t) = \mathcal{M}_{\odot}(t) \left(\frac{Z}{Z_{\odot}} \right)^{1.0}$$

with $Z_{\odot} = 0.017$. Thus, the radiation pressure for stars in the Small Magellanic Cloud (SMC), which has a ten times lower metallicity than our Galaxy, is ten times smaller than for Galactic stars of the same mass, radius and temperature (Lamers & Cassinelli 1999).

The general properties of a radiation driven wind can be derived from the momentum equation of a radiation driven wind:

$$v\frac{dv}{dr} = -\frac{GM_*}{r^2} + \frac{1}{\rho}\frac{dp}{dr} + g_{\mathrm{e}} + g_{\mathrm{L}} \tag{1.27}$$

where M_* is the mass of the star, and $\frac{1}{\rho}\frac{dp}{dr}$ is the acceleration due to gas pressure.

From Equation (1.27) it is possible to derive the expected mass loss rate $\dot{M}$ of a hot star, the terminal velocity of the wind v_{∞} and the expression for the velocity law:

$$v(r) = v_{\infty} \left(1 - \frac{R_*}{r} \right)^{\beta} \tag{1.28}$$

Equation (1.28) is known as "β-velocity law" (Castor et al. 1975), where β determines how steeply the velocity reaches the terminal velocity (see Figure 1.7). For OB supergiants, the terminal velocities are typically $v_{\infty} \approx 1000 - 2000$ km s^{-1}, $\beta \approx 0.5 - 1.5$, and the mass loss rates are of the order of $\dot{M} \approx 10^{-6}$ M$_{\odot}$ yr^{-1}.

1.3.3 Centrifugal inhibition of accretion

The observed lightcurves of some sources show a much stronger variability related to the orbital motion than expected from the dependence of the accretion rate on the β-velocity law ($\dot{M}_{\mathrm{acc}} \propto v_{\mathrm{rel}}^{-3}$, Equations 1.17 and 1.15). This can be explained with the *centrifugal inhibition of accretion*. The accretion onto a magnetized rotating neutron star is characterized by three radii: the accretion radius R_{acc} (Equation 1.15), the magnetospheric radius R_{m}, and the corotation radius R_{c}.

- **Magnetospheric radius.** The accreting matter is a ionized plasma interacting with the neutron star magnetic field. Because of this interaction, the matter is dragged along the field lines. The magnetospheric

[2]The metallicity Z is defined as the mass fraction of all species other than H and He.

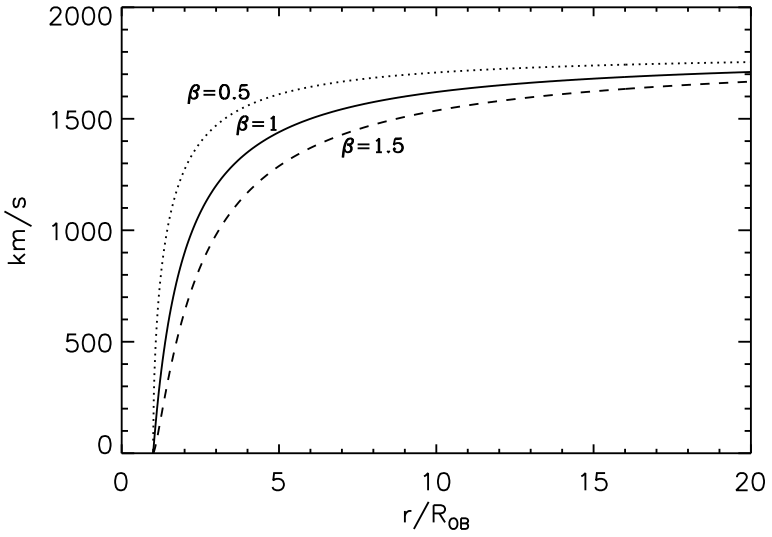

Figure 1.7: β-wind velocity (Equation 1.28) for three values of β (dotted line: $\beta = 0.5$, solid line: $\beta = 1$, dashed line: $\beta = 1.5$).

radius R_m (or *Alfvén radius*) is defined as the distance from the neutron star where the magnetic field pressure and the ram pressure of the accreted matter are in equilibrium (Davidson & Ostriker 1973), and can be obtained in the following way. Given the radius of the neutron star R_x, if B_0 is the surface magnetic field, the field at the magnetosphere is approximately given by:

$$B_\mathrm{m} = B_0 \frac{R_\mathrm{x}^3}{R_\mathrm{m}^3}$$

and the magnetic pressure is $B_\mathrm{m}/8\pi^2$. The ram pressure of the accreted matter at R_m is given by:

$$\rho v_\mathrm{rel}^2 \approx 2\rho \frac{GM_\mathrm{x}}{R_\mathrm{m}} \approx \frac{\dot{M}_\mathrm{acc}\sqrt{GM_\mathrm{x}}}{2\pi R_\mathrm{m}^{5/2}} \ .$$

Equating the magnetic pressure with the ram pressure:

$$B_\mathrm{m}^2/(8\pi) = \rho v_\mathrm{rel}^2/2 \ ,$$

and with the definition of the accretion radius (Equation 1.15) and the accretion rate (Equation 1.17), the magnetospheric radius can be written as:

$$R_\mathrm{m} \approx \left(\frac{B_0^2 R_\mathrm{x}^6}{4\dot{M}_\mathrm{acc}\sqrt{GM_\mathrm{x}}} \right)^{2/7} \ . \tag{1.29}$$

- **Corotation radius.** Consider a neutron star spinning at angular velocity Ω and period $P_{\rm spin} = 2\pi/\Omega$. The distance at which there is balance between the gravitational and the centrifugal forces is called *corotation radius*, and is defined as:

$$R_{\rm c} = \left(\frac{GM_{\rm x}}{\Omega^2}\right)^{1/3} = (GM_{\rm x})^{1/3}\left(\frac{P_{\rm spin}}{2\pi}\right)^{2/3} . \tag{1.30}$$

Different regimes of accretion, corresponding to the relative dimensions of these radii, can be identified. When $R_{\rm acc} > R_{\rm m}$ and $R_{\rm c} > R_{\rm m}$, there is direct accretion onto the neutron star surface, and the gravitational energy is converted into radiation with high efficiency:

$$L_{\rm x} \simeq \frac{GM_{\rm x}}{R_{\rm x}}\dot{M}_{\rm acc} . \tag{1.31}$$

If $R_{\rm c} < R_{\rm m} < R_{\rm acc}$, the neutron star is spinning too fast, and the magnetosphere rotates at a super-keplerian rate: in this case the wind material which penetrates through the accretion radius is stopped at the magnetospheric surface and cannot reach the neutron star surface. The X-ray luminosity produced by the magnetospheric impact is

$$L_{\rm x} \equiv \frac{GM_{\rm x}}{R_{\rm m}}\dot{M}_{\rm acc} . \tag{1.32}$$

Thus, when $R_{\rm c} < R_{\rm m}$, the centrifugal force inhibits matter from being accreted directly by the neutron star. This mechanism is the *centrifugal inhibition of accretion (c.i.)* (Stella et al. 1994; Illarionov & Sunyaev (1975); Campana et al. 1995).

Since $R_{\rm m}$ is inversely proportional to $\dot{M}_{\rm acc}$ (Equation 1.29), in an X-ray binary system with $\dot{M}_{\rm acc}$ that changes over time, the neutron star can accrete directly (when $\dot{M}_{\rm acc}$ is high enough) or can accrete onto the magnetosphere (when $\dot{M}_{\rm acc}$ is low enough). It is possible to have an accretion rate which changes over time in binary systems with high eccentricity: at periastron $\dot{M}_{\rm acc}$ is larger than at apastron (because $\dot{M}_{\rm acc} \propto \rho/v_{\rm rel}^3$, see Equations 1.17 and 1.15). The passage between these regimes of accretion can produce large luminosity gaps, of the order of $L_{\rm direct-accretion}/L_{\rm c.i.} \approx 10 - 10^4$ (see e.g. Raguzova & Lipunov 1998).

1.3.4 Accretion from a non-spherical wind

The stellar wind of the Be stars is composed by the polar wind and the equatorial wind. The velocity and density structures of these components are very different (Waters et al. 1989).

The velocity law of the polar wind can be described with the same equation used for the wind velocity of OB supergiant (Equation 1.28). From

observations of line profiles of UV resonance lines of Be stars $\beta \approx 1$, and $v_\infty \approx 600 - 2000$ km s^{-1} (e.g. Snow 1981), and mass loss rates of the order of $10^{-8} - 10^{-10}$ M$_\odot$ yr^{-1} (e.g. Howarth et al. 1984) were derived for the polar wind.

The density and velocity structure of the equatorial wind of Be stars was derived for the first time by Waters et al. (1988) from IR excess. They estimated a mass loss rate of the order of $\sim 10^{-7}$ M$_\odot$ yr^{-1}, a factor 10-100 larger than the mass loss rate of the polar region. Moreover, they found typical outflow velocities of $\sim 100 - 600$ km s^{-1}. Hence, the equatorial wind is denser and slower than the polar wind.

The density law in the equatorial region of the Be star is given by the equation:

$$\rho(r) = \rho_0 \left(\frac{r}{R_*}\right)^{-n} \tag{1.33}$$

where ρ_0 is the wind density at $r = R_*$ ($\rho_0 \approx 10^{-11}$ g cm^{-3}), and $2.1 \lesssim n \lesssim 3.5$.

From Equation (1.33), and assuming a steady state outflow, it is possible to obtain the *radial velocity law* in the equatorial region:

$$v_{\rm w}(r) = v_0 \left(\frac{r}{R_*}\right)^{n-2} \tag{1.34}$$

where the exact value of v_0 is unknown, but probably lies between 2 and 20 km s^{-1} (Lamers & Waters 1987).

The wind velocity of Be star is also composed by a rotational component $v_{\rm rot,w}$ due to the high rotational velocity of the star (equatorial velocity of Be star ≈ 300 km s^{-1}):

$$v_{\rm rot,w}(r) = v_{\rm rot,*} \left(\frac{r}{R_*}\right)^{-\alpha} \tag{1.35}$$

where $v_{\rm rot,*}$ is the rotational velocity at the photosphere of the Be star, $\alpha = 0.5$ in the case of keplerian rotation of the circumstellar disk, and $\alpha = 1$ if the angular momentum of the circumstelllar disk is conserved.

From Equations (1.2) and (1.17), it is possible to obtain the X-ray luminosity of Be/X-ray binaries, when the neutron star crosses the circumstellar disk along its orbit:

$$L_{\rm x} = 4\pi \frac{(GM_{\rm x})^3}{R_{\rm x}} \frac{\rho}{v_{\rm rel}^3} \tag{1.36}$$

where ρ is given by the Equation (1.33), $v_{\rm rel}$ by the Equations (1.16), (1.34), (1.35).

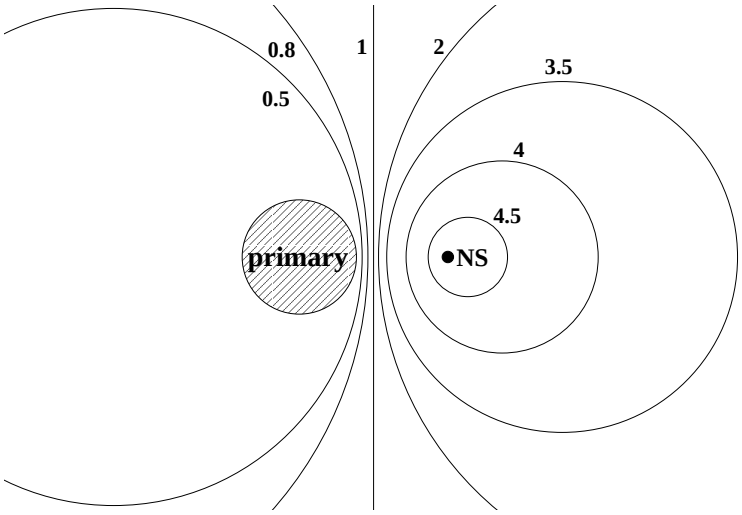

Figure 1.8: Ionization spheres of constant ξ. Lines are labeled by $\log \xi$.

1.3.5 X-ray ionization of stellar winds in HMXBs

The physics of the interaction of an accreting X-ray source with the stellar wind driven by a massive companion was clarified by the pioneering work of Hatchett & McCray (1977) and Kallman & McCray (1982).

The X-ray continuum ionizes the matter in the wind: if matter is optically thin to the ionizing radiation, then the ionization state at any point is determined by the *ionization parameter* ξ, defined by Tarter et al. (1969) as:

$$\xi \equiv \frac{L_{\rm x}}{nR^2} \tag{1.37}$$

where $L_{\rm x}$ is the luminosity of the ionizing X-ray source, and n is the number density in the wind at a distance R from the source.

Contours of constant ξ are isothermal surfaces which delineate distinct ionization zones with characteristics line-emission properties (see Figure 1.8). The shape of these contours depends on the density profile $n(R)$ of the wind, which, in turn depends on the velocity profile $v(r)$ of the wind (Equation 1.28) by the continuity equation:

$$n(r) = \frac{\dot{M}}{4\pi\mu m_{\rm p} r^2 v(r)} \ , \tag{1.38}$$

where $\dot{M}$ is the wind mass-loss rate from the massive companion, μ is the mean atomic weight of the wind-material, and r is the distance from the center of the companion.

Combining Equations (1.37), (1.38), and (1.28), it is possible to obtain

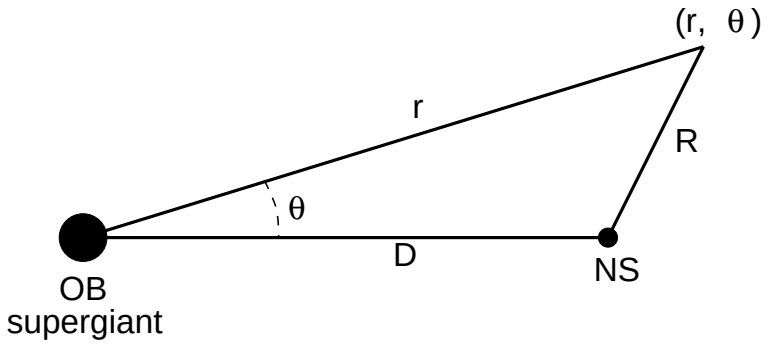

Figure 1.9: Schematic representation of the coordinate system $\vec{R} \equiv \vec{R}(r, \theta)$ used to obtain the ξ contour shapes.

for the ionization parameter:

$$\xi = \xi_0 \left(\frac{r}{R}\right)^2 \left(1 - \frac{R_*}{r}\right)^{\beta} \tag{1.39}$$

where:

$$\xi_0 \equiv \frac{4\pi\mu m_p v_\infty L_{\rm x}}{\dot{M}} \tag{1.40}$$

The distance R from the X-ray source is then given by

$$R = \sqrt{r^2 + D^2 - 2rD\cos\theta}\ , \tag{1.41}$$

where D is the orbital separation between the centers of the two stars (see Figure 1.9), and Equation (1.41) together with Equation (1.40), gives the contour-shapes.

The effect of X-ray photoionization on the accretion

The high ionization of the wind produced by the X-rays from the neutron star can strongly modify the wind-driven mechanism. As the atoms become highly ionized, their capability for absorbing the UV line-radiation from the companion star, which drives the wind, is reduced. This was pointed out in the original work of Hatchett & McCray (1977). This implies that the winds from the massive companion in HMXBs are different from those from isolated OB stars.

Several attempts have been made to include the effects of X-ray photoionization in HMXBs.

MacGregor & Vitello (1982) modified the wind theory of Castor, Abbott, & Klein (1975), including the effect of X-ray ionization on the wind structure. As a consequence of the small number of driving lines they considered in the calculations, MacGregor & Vitello (1982) found that at X-ray luminosities

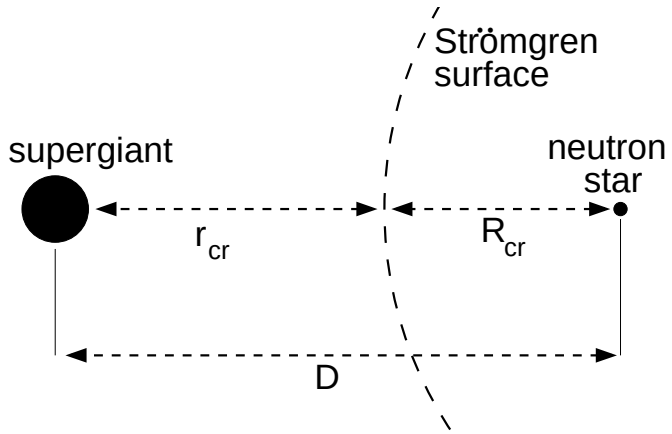

Figure 1.10: Schematic representation of a Strömgren surface produced by a neutron star orbiting around a supergiant. The labels indicate the distance of this surface which respect the two stars, accordingly to Ho & Arons (1987).

of $L_{\rm x} \simeq 10^{34}$ erg s^{-1} the radiative line force is extinguished and the wind ceases. This value is significantly lower than that observed in HMXBs, where $L_{\rm x} \simeq 10^{36}$ erg s^{-1} or greater.

Blondin et al. (1990) performed a two-dimensional hydrodynamic simulation of the winds in HMXBs and found that the X-ray ionization could distrupt the flow from the donor star, leading to the formation of dense wakes around the neutron star responsible of the episodes of enhanced absorption.

Stevens (1991) followed the approach of MacGregor & Vitello (1982), but considered a much larger number of driving lines and included the effects of the optical depth in the force multiplier calculations.

Ho & Arons (1987) developed an analytic model, assuming a spherically symmetric wind ionized by the X-ray photons from the neutron star. They assumed that the radiation line force (Equation 1.26) is turned off at a distance $R_{\rm cr}$ from the neutron star, where $\xi_{\rm cr} = 10^4$ erg cm s^{-1}. Thus, the wind follows the standard β-velocity law (Equation 1.28; they assumed $\beta = 0.5$) up to a distance $R_{\rm cr}$ (see Figure 1.10). At $R_{\rm cr}$ the wind is sufficiently ionized to become transparent to the UV photons. Hence, inside the sphere with radius $R_{\rm cr}$ and the neutron star in the centre, the wind velocity is assumed constant. $R_{\rm cr}$ and the associated wind terminal velocity depends on the luminosity of the X-ray source: if the X-ray luminosity increases, also $R_{\rm cr}$ increases, and consequently the terminal wind velocity decreases. In turn, the X-ray luminosity is determined by the relative wind velocity $v_{\rm rel}$: a lower wind velocity caused by the ionizing effects of the X-rays, implies an increase in the expected luminosity (Equation 1.18). Ho & Arons (1987) built a model to describe this feedback mechanism and to find self-consistent solutions for wind-fed accretion onto neutron star. This model is based on

the accretion X-ray luminosity equation

$$L_{\rm x} \simeq \frac{GM_{\rm x}}{R_{\rm x}}\dot{M}_{\rm acc} \tag{1.42}$$

and on the Equation 1.37, written in the form:

$$L_{\rm x} = \xi n R_{\xi}^2 \ . \tag{1.43}$$

They wrote Equations (1.42) and (1.43) in order to show their dependence on $R_{\rm x}$. From Equation (1.42), they obtained the *accretion equation*:

$$L_{\rm a}(x) = \frac{\hat{L}_{\rm a}}{(1-\alpha/x)^2} \tag{1.44}$$

where

$$\hat{L}_{\rm a} = \frac{(GM_{\rm x})^3}{R_{\rm x}}\frac{\dot{M}_*}{D^2 v_\infty^4 (1-r_*/r_\xi)^2} \ .$$

D is the distance of the neutron star from the companion star, r_* is the radius of the compaion star and $\dot{M}_*$ its mass loss rate; $\alpha \equiv r_*/D$ and $x \equiv r_\xi/D$. From Equation (1.43), they obtained the *feedback equation*:

$$L_{\rm b}(x) = \hat{L}_{\rm b}\left[\frac{(1-x)^2}{x^2(1-\alpha/x)^{1/2}}\right] \tag{1.45}$$

where

$$\hat{L}_{\rm b} = \frac{\dot{M}_* \xi_{\rm cr}}{4\pi\mu v_\infty}$$

and $\mu = m_{\rm p}$. The steady state solution is obtained by equating $L_{\rm a}$ (Equation 1.44) and $L_{\rm b}$ (Equation 1.45), and solving for x. Ho & Arons (1987) applied this model to six X-ray binaries (4U 1700-377, Cen X-3, Cyg X-1, SMC X-1, Vela X-1, 4U 1538-52) and predicted for these sources the existence of two stable luminosity states, called "high and low X-ray luminosity solutions".

1.3.6 Accretion disk

The formation of an accretion disk from Roche lobe overflow

In the case of Roche lobe overflow the matter from the mass-losing star leaves the critical lobe near the inner Lagrangian point L_1 (Figure 1.11). In this case, the specific angular momentum with respect to the orbiting neutron star is:

$$l = \Omega_{\rm orb}(a - R_{\rm L})(a - \lambda R_{\rm L}) \tag{1.46}$$

where $R_{\rm L}$ is the location of the inner Lagrangian point, a is the orbital separation, and λ is the ratio of the angular velocities of the rotational

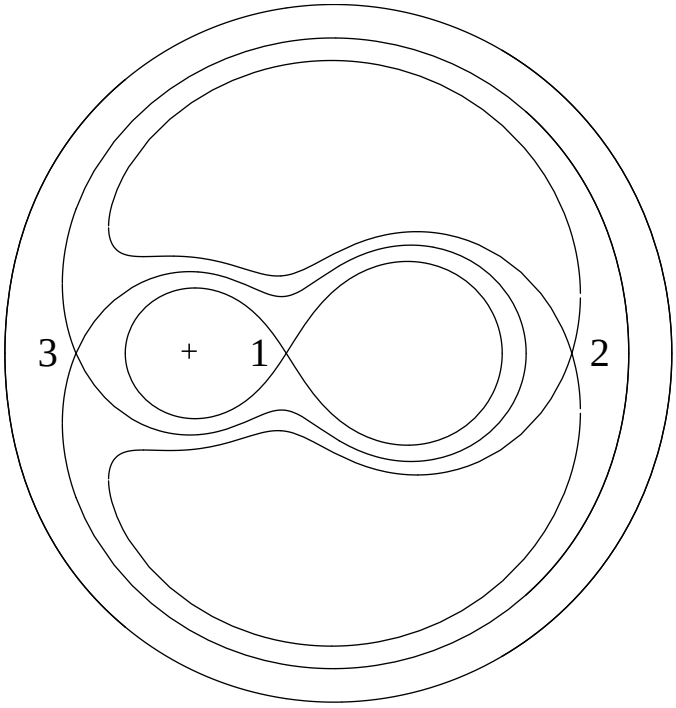

Figure 1.11: Section in the orbital plane of the Roche equipotentials for a binary system. The compact object is represented by the cross. The Lagrangian points are labelled 1, 2, and 3. Mass can flow through the Lagrangian point 1 from one star to its companion if the star fills its Roche lobe.

motion of the companion and of the orbital motion of the neutron star (see Henrichs 1983 and references therein).

Equation (1.46) gives a specific angular momentum which is roughly a factor of $(a/R_{\rm acc})^2$ higher than in the case of accretion from a wind. When Roche lobe overflow occurs, an accretion disk is expected to form if:

$$R_{\rm k} \equiv \frac{l^2}{GM_{\rm x}} > R_{\rm m} \tag{1.47}$$

where $R_{\rm k}$ is the radius at which the captured matter with angular momentum l goes into a keplerian orbit around a neutron star with mass $M_{\rm x}$. $R_{\rm L}$ can be described by the approximated formula obtained by Eggleton (1983) and accurate to within 1%:

$$R_{\rm L} = a\frac{0.49q^{2/3}}{0.6q^{2/3} + \ln(1+q^{1/3})} \quad 0 < q < \infty \tag{1.48}$$

where q is the mass ratio.

Transient disks

In wind-fed X-ray binary systems, the wind density and velocity both vary radially outwards from the mass-losing star; thus, the wind around the accreting star is not symmetric (especially in close binary systems), and the specific angular momentum of the captured matter is $J \neq 0$.

If the specific angular momentum is large enough, the chances of disk formation increase (Illarionov & Sunyaev 1975; Shapiro & Lightman 1976, Wang 1981). The specific angular momentum accreted by the compact object can be estimated with the equation:

$$J = \eta\frac{R_{\rm acc}^2}{4}\frac{2\pi}{P_{\rm orb}} \tag{1.49}$$

where $\eta \simeq 1$ is an efficiency factor (King 1995). Equation (1.49) shows that the specific angular momentum is inversely proportional to the relative wind velocity $v_{\rm rel}$ (since $R_{\rm acc} \propto 1/v_{\rm rel}^2$) and inversely proportional to the orbital period. Hence, the chances of disk formation is higher for X-ray binary systems with narrow orbits and low wind velocities. Moreover, in the case of asymmetric accretion, the accretion radius $R_{\rm acc}$ is not symmetric, thus Equation (1.49) is a reasonable estimate of J if the asymmetries are small.

Matsuda et al. (1987) and Taam et al. (1988) performed two-dimensional hydrodynamic simulations of the Bondi-Hoyle-Lyttleton geometry, with the condition of asymmetric stellar wind, and density and velocity gradients, to study the dynamics of the wind accretion in a close binary system. They found that the flow near the accreting star sporadically changes its direction of rotation: the authors called this phenomenon *accretion disk instability* or *flip-flop flow*.

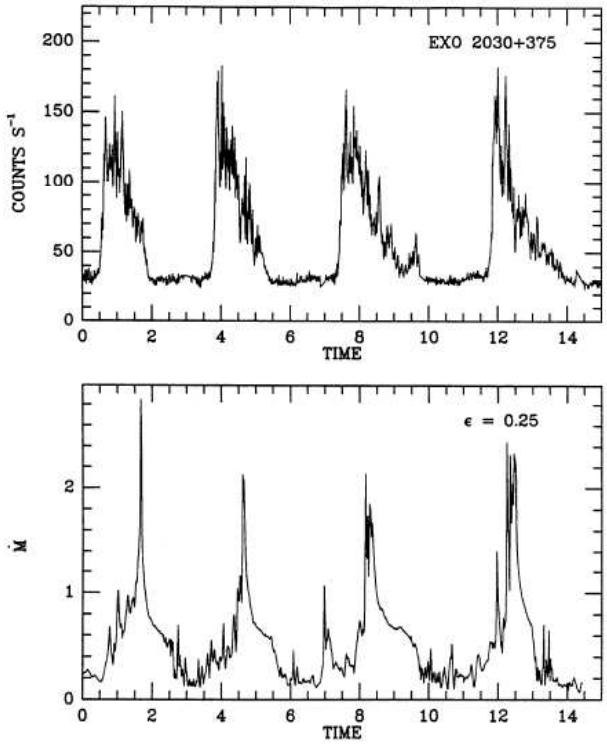

Figure 1.12: Comparison between the first four flares observed from EXO 2030+375 (upper panel) and the mass accretion rate $\dot{M}$ obtained from the numerical simulation of Taam et al. (1988). The time in both panel is measured in hours (Taam et al. 1988).

In particular Taam et al. (1988) proposed a mechanism for the production of quasi-periodic flares from Be/X-ray binaries. They demonstrate that the angular momentum capture from a wind with density and velocity inhomogeneities can be high for brief periods, when an accretion disk forms around the compact object. The instability in the flow leads to the formation of disks which circulate in either directions. Such flow reversals are a direct consequence of the interaction of the incident flow with the shock fronts of the accretion wake and the disk. When the matter of the disk is released onto the compact object a flare is produced.

Taam et al. (1988) found that the time scale for the duration of the flare can be approximately estimated by the equation:

$$\tau \sim \frac{3R_{\rm acc}}{v_{\rm rel}} \tag{1.50}$$

where $v_{\rm rel}$ is the relative wind velocity, and $R_{\rm acc}$ is the accretion radius.

The mechanism proposed by Taam et al. (1988) has been succesfully applied to the Be/X-ray binary system EXO 2030+375. In 1985 the *EXOSAT*

satellite observed a series of six flares that recurred quasi-periodically every ~ 3.96 hr from EXO 2030+375 (Parmar et al. 1989). Taam et al. (1988) interpreted the quasi-periodic flaring behaviour observed within the context of an instability in the accretion flow, which is the responsible for the formation of transient accretion disks. By means of two-dimensional numerical simulations, Taam et al. (1988) were able to reproduce the quasi-periodic flares assuming for the velocity of the outflowing matter a value of ~ 550 km s^{-1} (see Figure 1.12).

The accretion instability has been subsequently found in numerous hydrodynamic simulations of two-dimensional accretion (e.g. Zarinelli et al. 1995; Blondin & Pope 2009), but has not been unambiguosly identified in three-dimensional simulations (see Ruffert 1999).

1.4 High Mass X-ray Binaries

The HMXBs are composed by two subclasses, depending on the spectral type of the optical counterpart:

- The spectral type is O-B, and the luminosity class is I to III;
- The primary is a B-emission (Be) star, characterized by emission lines (mainly the Balmer series) which originate in circumstellar material.

1.4.1 HMXBs with OB supergiants

This class is divided in two subclasses:

- *Supergiant High Mass X-ray Binaries (SGXBs)*: they are characterized by their persistent X-ray luminosity, at a level of about $10^{36} - 10^{37}$ erg s^{-1}. The orbits are quasi-circular, with orbital periods of $P_{\rm orb} \approx 1 - 15$ days; the X-ray emission is produced by the accretion of matter from the supergiant, transferred via a strong stellar wind. The typical mass loss rate are $\dot{M} \approx 10^{-6}$ M$_\odot$ yr^{-1}. Some SGXBs show a short-lived phase of Roche lobe overflow, with the formation of an accretion disk. An interesting example is Cen X-3, where the accretion is produced by the wind together with an accretion disk around the neutron star.
- *Supergiant Fast X-ray Transients (SFXTs)* are transient HMXBs with OB supergiant and an accreting compact object. For more information see Chapter 2.

1.4.2 Be/X-ray binaries

The Be/X-ray binaries, first recognized as a class by Maraschi et al. (1976), are composed by a neutron star and a rapidly rotating B-emission star,

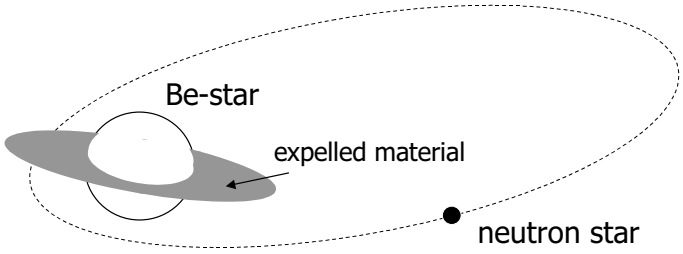

Figure 1.13: Schematic model of a Be/X-ray binary system. The neutron star moves in an eccentric orbit around the Be star. Near the periastron passage the neutron star accretes circumstellar matter, ejected from the rotating Be star, resulting in an X-ray outburst lasting several days (Tauris & van den Heuvel 2003).

situated on, or close to, the main-sequence. This is the most numerous class of HMXBs. The companion stars have masses in the range of $8 - 20$ $M_{\odot}$, which show spectral lines in emission, and in the infrared they are brighter than their non-Hα emitting counterparts of the same spectral type. The line emission and IR excess originate in extended circumstellar envelopes of ionised gas surrounding the equator of the B star (Figure 1.13).

Evolutionary calculations show that Be star + white dwarf or Be star + black-hole should also be common type of systems. However, no clear evidence of their existence has been shown yet (Zhang et al. 2004b).

Be/X-ray binaries are strong emitters of X-ray radiation, which is produced as the result of accretion of matter from the circumstellar disk of the companion star onto the neutron star.

The Be/X-ray binaries are transient sources often unobservable for months to years. This variability is most probably related to the irregular optical and IR outbursts generally observed in Be stars, and it is attributed to structural changes of the circumstellar disk. Sometimes the Be star loses the disk (Reig et al. 2001). When this occurs the Hα line shows an absorption profile and the X-ray activity ceases.

The long-term X-ray variability of the transient Be/X-ray binaries is characterized by two type of outbursting activity:

- ***Type I outbursts:*** These are regular and (quasi)-periodic outbursts, normally peaking at or close to periastron passage of the neutron star. They tend to cover a relatively small fraction of the orbital period $(0.2 - 0.3P_{\rm orb})$. The X-ray flux increases by up to two orders of magnitude with respect to the pre-outburst state, reaching peak luminosity of $L_{\rm x} \lesssim 10^{37}$ erg s^{-1}.

- ***Type II outbursts:*** They represent the major increase of the X-ray flux, $10^3 - 10^4$ times that at quiescence. They reach the Eddington luminosity for a neutron star ($L_{\rm x} \simeq 10^{38}$ erg s^{-1}).They do not show

any preferred orbital phase and last for a large fraction of an orbital period or even for several orbital periods. The formation of an accretion disk during Type II outbursts may occurr (see e.g. Motch et al. 1991), and the discovery of quasi-periodic oscillations in some systems would support this scenario (Angelini et al. 1989). The presence of an accretion disk can also explain the large and steady spin-up rates seen during the giant outbursts, which are difficult to account for by means of direct accretion.

The X-ray emission from the Be/X-ray binaries tends to be extremely variable, ranging from complete absence to giant transient outbursts lasting weeks to months. During such an outburst episode one often observes orbital modulation of the X-ray emission, due to the motion of the neutron star in an eccentric orbit.

Most Be/X-ray binaries are transient systems and present eccentric orbits ($e \gtrsim 0.3$), although persistent sources also exist. Persistent Be/X-ray binaries display much less X-ray variability and lower flux ($L_{\rm x} \lesssim 10^{35}$ erg s^{-1}) and contain slowly rotating neutron stars ($P_{\rm spin} > 10^2$ s; Reig & Roche 1999). The existence of a new class of Be/X-ray binaries has been suggested (Pfahl et al. 2002). The name of this class is *low-e Be/X-ray*, it is characterized by wide orbits ($P_{\rm orb} > 30$ d) and low eccentricity ($e \lesssim 0.2$).

1.5 Pulse profiles

For spherical accretion, the accreting material is probably stopped by collisionless shocks outside the magnetosphere. It is thought that plasma is channeled by the field lines to the magnetic poles in a narrow accretion column.

The field lines for a dipole field are defined by $\sin^2\theta/r$ =constant, where r is the distance of a generic point P from the neutron star and θ is the angle between r and the dipole moment (see Figure 1.14). The magnetic pole region is delimitated by the last field lines that are closed inside the magnetospheric radius $R_{\rm m}$ (hence, $\theta = \pi/2$ at $r = R_{\rm m}$); at the magnetic pole, these magnetic lines forms an angle $\theta_{\rm c}$ given by:

$$\sin^2\theta_{\rm c} = \frac{R_{\rm x}}{R_{\rm m}} \approx \frac{R_{\rm x}}{\left(\frac{B_0^2 R_{\rm x}^6}{4\dot{M}_{\rm acc}\sqrt{GM_{\rm x}}}\right)^{2/7}} \tag{1.51}$$

where B_0 is the magnetic field at the surface of the neutron star, and $R_{\rm x}$ is the radius of the neutron star. Thus, the area of the accretion column at the stellar surface is approximately given by:

$$A \approx \pi R_{\rm x}^2 \sin^2\theta_{\rm c} \tag{1.52}$$

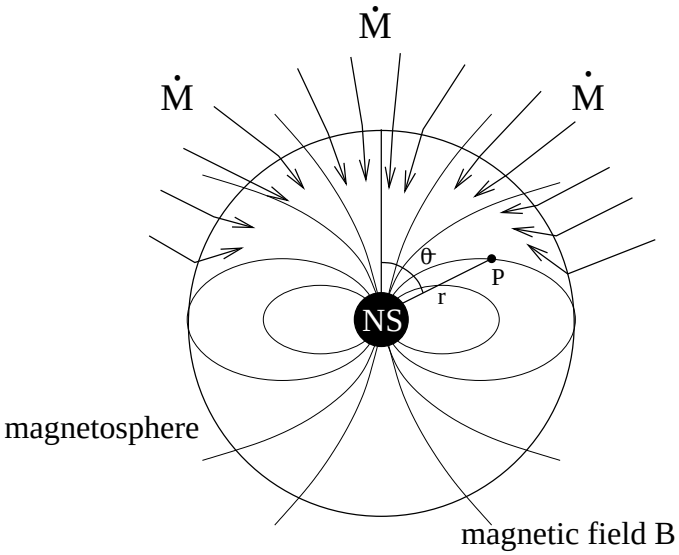

Figure 1.14: Schematic representation of the dipole magnetosphere around a neutron star which is accreting material. Infalling material is channeled by the field lines to the magnetic poles in a narrow accretion column.

Usually $A \approx 2 - 3$ km^2, which is a small fraction of the total spherical surface area. However, in the framework of the models of Arons & Lea (1976) and Elsner & Lamb (1977), the Rayleigh-Taylor instability allows blobs or filaments of plasma to penetrate the magnetosphere and fall toward the stellar surface without becoming attached to the field lines. Most of the accreted material falls predominantly near the magnetic poles, but the area on the surface of the neutron star over which the inflowing material impacts, exceeds that given by Equation (1.52).

The observations have shown that the pulse profile of an accretion powered X-ray pulsar depends on X-ray luminosity (or mass accretion rate; Wang & Welter 1981):

- $L_{\rm x} \lesssim 10^{36}$ erg s^{-1}: the pulse profiles are sinusoidal-like with little dependence on energy;
- $10^{36} \lesssim L_{\rm x} \lesssim 10^{37}$ erg s^{-1}: the profiles become more energy dependent: at high energies the modulations are still simple sine waves, but at lower energies the pulse profile shape become more complicated.
- $L_{\rm x} \gtrsim 10^{37}$ erg s^{-1}: the pulse profiles of some sources show a 180° phase reversal from one energy band to the next.

Figure 1.15 shows the high variability of the pulse shape with both energy

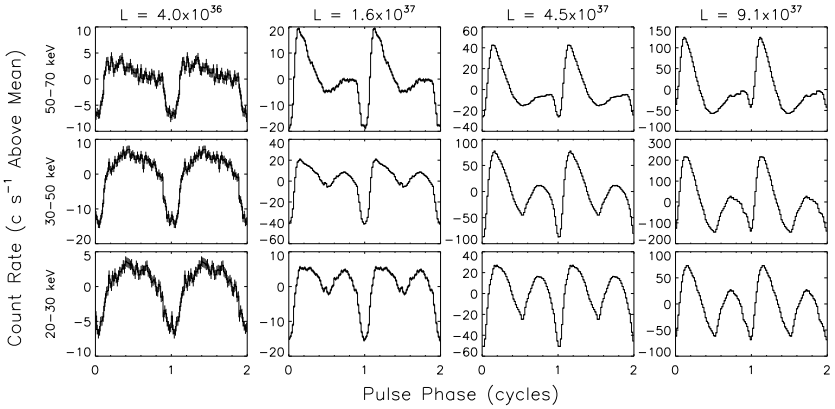

Figure 1.15: Pulse profiles of A0535+26 as a function of flux and energy during the giant outburst in 1994 February-March observed with *BATSE* on board the *Compton Gamma Ray Observatory (CGRO)* (Bildsten et al. 1997).

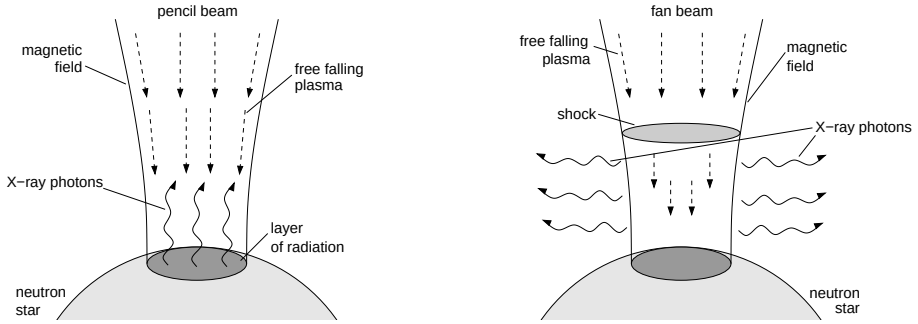

Figure 1.16: Possible geometries of the emission region. Pencil beam *(left panel)*: the radiation escapes outwards; Fan beam *(right panel)*: radiation is emitted sideways.

and flux of the Be/X-ray binary system A0535+26, observed with *BATSE* on board the *CGRO* satellite (Bildsten et al. 1997).

The luminosity dependence of the pulse profiles is usually explained with geometric models where the beam shape can be described in terms of *pencil beam*, when most of the radiation is emitted along the magnetic field ($L_{\rm x} \lesssim 10^{37}$ erg s^{-1}), or *fan beam*, when most of the radiation is emitted perpendicularly to the magnetic field ($L_{\rm x} \gtrsim 10^{37}$ erg s^{-1}; White et al. 1983; Figure 1.16). The beaming direction (pencil or fan) from the polar cap of the neutron star depends on whether a shock in the accretion column is present (see e.g. Meszaros 1984). For luminosities $L_{\rm x} \lesssim 10^{37}$ erg s^{-1} (i.e. low accretion rate), the emergent radiation pressure acting ong the infalling plasma is negligible, then the optical depth of the accreting plasma is low:

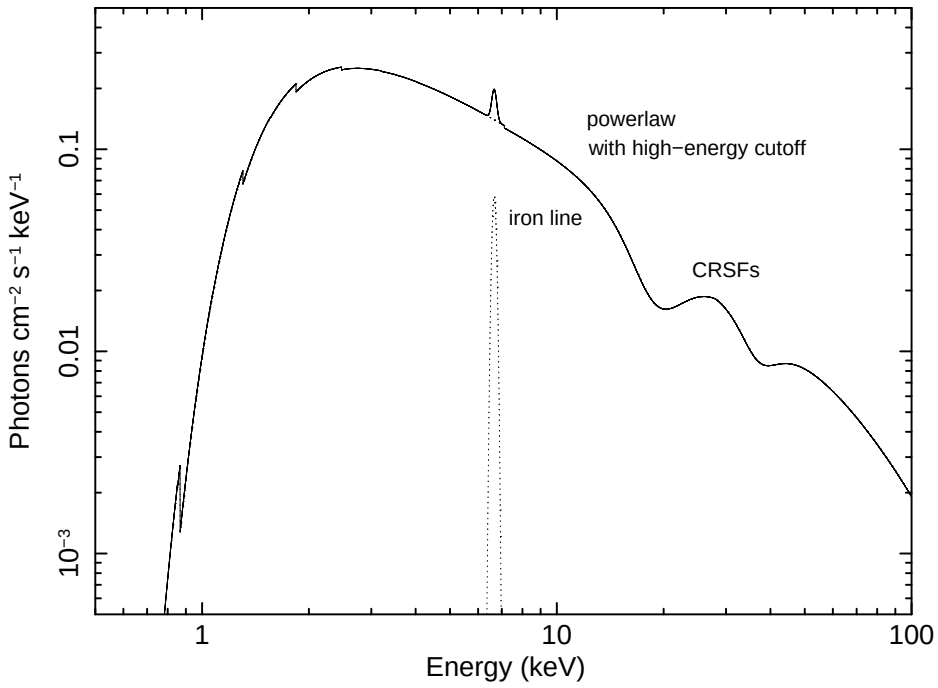

Figure 1.17: Photon spectrum: the plot includes the total spectrum (solid line), the individual components (dashed lines): powerlaw with highenergy cutoff (Equation 1.53), iron line, cyclotron resonant scattering features (CRSFs), photoelectric absorption.

the inflowing gas is not shocked and a pencil beam of emission is expected to form. For luminosities $L_{\rm x} \gtrsim 10^{37}$ erg s^{-1} (i.e. high accretion rate), the radiation pressure dominates, and the inflowing material dissipates its kinetic energy by inverse Compton scattering in a radiative shock. The photons emitted by the plasma below the shocked region escape in a fan beam from the sides of the column because of the large optical depth within the shock.

1.6 X-ray spectra of HMXBs

The X-ray spectra of the accreting neutron stars in HMXBs are usually well fitted by a power law with an exponential cutoff at energy $10 - 30$ keV:

$$f(E) = AE^{-\Gamma}, \qquad E < E_{\rm c} \tag{1.53}$$

$$f(E) = AE^{-\Gamma} \exp{(E_{\rm c} - E)/E_{\rm f}}, \qquad E \geq E_{\rm c} \tag{1.54}$$

where Γ is called power law index, $E_{\rm c}$ is the high energy cutoff and $E_{\rm f}$ is the folding energy. There are also indications of cyclotron features and iron emission lines from many HMXBs (see the photon spectrum in Figure 1.17).

The X-ray spectrum of HMXBs depends in a complicated way upon the flow geometry and upon the manner in which the incident plasma is decelerated near the neutron star surface. In the scenario proposed by Zel'Dovich & Shakura (1969), the accreting plasma falls towards the neutron star surface, decelerating via Coulomb collisions with electrons. When the infalling material is stopped by Coulomb collisions at the stellar surface, most of the energy is deposited and thermalized before escaping. Then, the photon energies can be described by a blackbody spectrum, and, for spherical flow, the effective blackbody temperature at the neutron star surface is given by:

$$T \gtrsim T_{\rm bb} = \left(\frac{L_{\rm x}}{4\pi R_{\rm x}^2 \sigma} \right)^{1/4} \approx 10^7 \times R_6^{-1/2} L_{37}^{1/4} \text{ K} \rightarrow 1 \times R_6^{-1/2} L_{37}^{1/4} \text{ keV} \quad (1.55)$$

where R_6 is the radius of the neutron star in units of 10^6 cm and L_{37} is the X-ray luminosity in units of 10^{37} erg s^{-1}.

The energy of the photons emitted by the neutron star surface increases because of the Thomson scattering by electrons in the "lower" atmosphere, and inverse Compton by hot electrons ($\lesssim 10^8$ K) in the "upper" atmosphere.

Many HMXBs display in their X-ray spectra iron emission between 6.4 and 6.7 keV. The iron emission line does not come from within a few stellar radii of the neutron star surface. In fact, the plasma above the magnetic pole is fully ionized by the X-ray photons emitted by the neutron star. On the contrary, the typical metallicity of the companion star allows the stellar wind of the primary, or the magnetosphere of the neutron star, to be the sources of the iron emission lines observed.

Becker & Wolff (2005) and Becker & Wolff (2007) developed a new theoretical model for the spectral formation process in accretion-powered X-ray pulsars (see Figure 1.18). In their model, blackbody seed photons are produced at the surface of the thermal mound located at the base of the accretion column, and cyclotron and bremsstrahlung seed photons are produced in the optically thin region above the thermal mound. Part of these photons experience Comptonization at the radiative shock, located above the stellar surface, where the infalling plasma is strongly compressed. In this Comptonization process, seed photons increase their energy if the velocity of the infalling electrons is much larger than their thermal velocity. The exponential cutoff at $10-30$ keV is due to thermal Comptonization processes, which transfer energy from high to low energy photons via electron scattering.

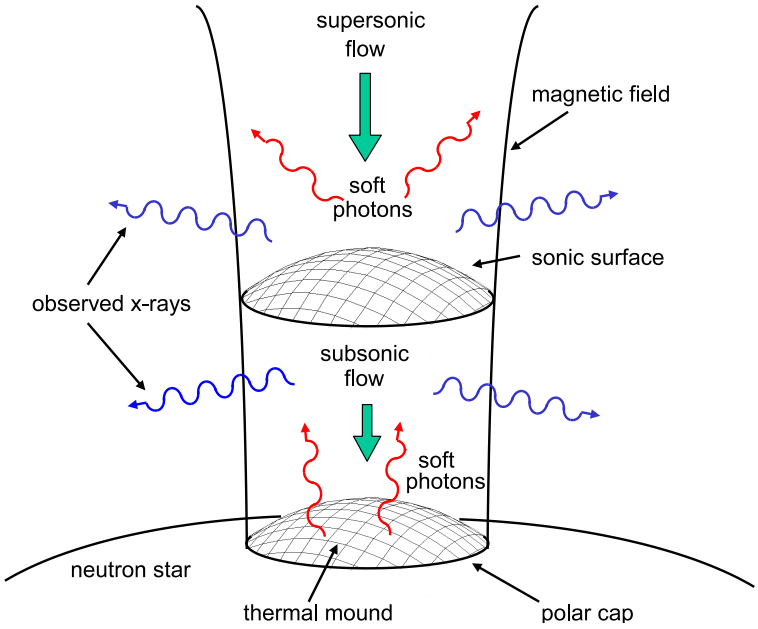

Figure 1.18: Schematic representation of the plasma accreting onto the magnetic polar cap of a neutron star. Seed photons are created throughout the accretion column via bremsstrahlung and cyclotron emission, and additional blackbody photons are emitted from the surface of the thermal mound near the base of the column (Becker & Wolff 2007).

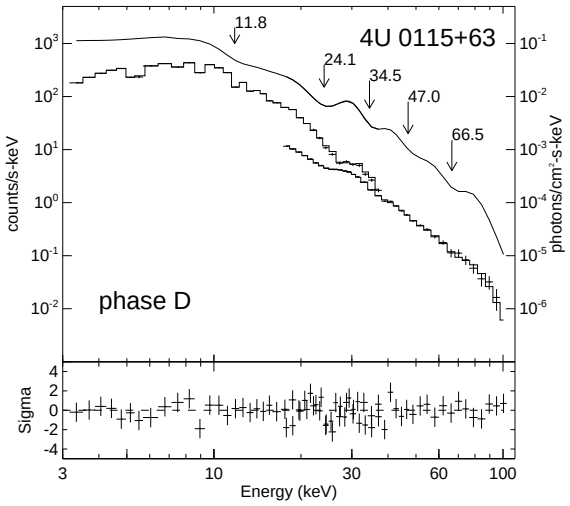

Figure 1.19: The spectrum of the HMXB 4U 0115+63 showing evidence for five CRSFs (Heindl et al. 1999).

1.6.1 Cyclotron Resonant Scattering Feature

Cyclotron Resonance Scattering Features (CRSFs), discovered for the first time through a balloon observation of Her X-1 (Truemper et al. 1978), are absorption lines in the spectra of accreting X-ray pulsars (see Figure 1.19), and provide a direct method for the determination of the magnetic field of the observed neutron star (see Schönherr et al. 2007 and references therein).

The line energy of the fundamental CRSF is related to the magnetic field strength by the equation

$$E_{\rm cyc} \approx \frac{\hbar e B}{m_{\rm e} c} \simeq 11.7 B_{12} \text{ keV} \tag{1.56}$$

where B_{12} is the magnetic field strength in units of 10^{12} G, e and $m_{\rm e}c$ are the electron charge and momentum, respectively.

Because of the strong magnetic field, the electron motion in the direction perpendicular to B is quantized, leading to the so-called *Landau levels* (see e.g. Mészáros 1992). In the non-relativistic case, the energy associated to the fundamental Landau level is given by Equation (1.56) and the higher harmonics have an energy n times the fundamental energy. The X-ray photons produced by the accretion undergo scattering processes with the electrons in the plasma of the accretion column. Photons with energies close to $\approx n\hbar eB/(m_{\rm e}c)$ (with $n = 1, 2, ...$, where $n = 1$ corresponds to the fundamental line) are scattered out of the line of sight, creating a drop in their number and an "absorption" line in the X-ray spectrum.

When relativistic corrections are taken into account, the expected absorption features in the photon spectrum are given by:

$$E_{\rm n} = m_{\rm e}c^2 \frac{\sqrt{1 + 2n\frac{Be\hbar}{m^2c^3}\sin^2\theta} - 1}{\sin^2\theta} \frac{1}{1+z} \tag{1.57}$$

where θ is the angle between the photon direction and the magnetic field vector. Equation (1.57) shows that the observed line energy is shifted by a factor $1/(1+z)$ because of the gravitational redshift z that, at the neutron star surface, is approximately $z = [1 - 2GM/(Rc^2)]^{-1/2} - 1 \approx 0.3$, assuming $M = 1.4$ M$_\odot$ and $R = 10$ km for the mass and radius of the neutron star.

Many HMXBs showing CRSFs are known. In most objects one line is seen, however some pulsars show more lines: for example, 4U 0115+63 shows five lines (Figure 1.19).

Chapter 2

Supergiant Fast X-ray Transients

During an observation of the black hole candidate 1E 1740.7-2942 with the *Proportional Counter Array (PCA)* on the *Rossi X-ray Timing Explorer (RXTE)*, Smith et al. (1998) discovered in 1997 August 12 the new X-ray transient XTE J1739-302. During the outburst, XTE J1739-302 was the brightest source in the direction of the Galactic center ($\sim 3 \times 10^{-9}$ erg cm^2 s^{-1} in the energy range $2-25$ keV), but the source apparently remained active only one day: it was not detectable in the previous scan of the region performed 9 days earlier and in the next scan performed 2 days later.

Although the counterpart was not known at other wavelengths, Smith et al. (1998) proposed that XTE J1739-302 was a Be/X-ray transient based upon the X-ray spectrum and the intensity reached during the outburst. Nevertheless, they were aware that the unusual short outburst displayed by the source was not typical for the class of Be/X-ray binaries.

In 2003 August 26, Sunyaev et al. (2003a) reported the discovery of the new transient source IGR J17391-3021 with the IBIS/ISGRI instrument (Ubertini et al. 2003) on board the *INTEGRAL* satellite. They noted that the position of IGR J17391-3021 was compatible with the location of XTE J1739-302. The association between these two sources was subsequently confirmed by Sguera et al. (2005) thanks to a refined position of IGR J17391-3021 obtained with IBIS/ISGRI.

A *Chandra* observation allowed to identify the optical counterpart of XTE J1739-302 as a supergiant (Smith et al. 2003). Further optical and infrared observations led to identify the counterpart of the X-ray transient binary as an O8Iab(f) at a distance of 2.3 kpc (Negueruela et al. 2006b).

During an observation of the Galactic Center field on 2003 September 17 performed by IBIS/ISGRI, Sunyaev et al. (2003b) reported the discovery of IGR J17544-2619. *XMM-Newton* observations provided a refined position (Gonzalez-Riestra et al. 2003), which allowed to associate IGR J17544-2619

with the optical near-infrared counterpart 2MASS J17542527-2619526, and with the *ROSAT* source 1RXS J175428.3-262035 (Wijnands 2003). From optical, near-infrared and X-ray observations, Pellizza et al. (2006) classified the counterpart as a O9Ib star at a distance of 3.6 kpc (Rahoui et al. 2008).

The discovery of XTE J1739-302 and IGR J17544-2619 led Smith et al. (2004) to speculate the existence of other sources with a similar behaviour in our Galaxy, belonging to a new class of X-ray binaries that they called *"High Mass Fast Transients"*.

The Galactic Plane monitoring performed by the *INTErnational Gamma-Ray Astrophysics Laboratory* (*INTEGRAL*), launched in 2002, has allowed to confirm the hypothesis of Smith et al. (2004), thanks to the discovery of other sources displaying similar properties to the prototypes XTE J1739-302 and IGR J17544-2619 (Sguera et al. 2005; Sguera et al. 2006; Negueruela et al. 2006a).

Further *XMM-Newton* and *Chandra* observations (e.g. Tomsick et al. 2006; Gonzalez-Riestra et al. 2003) allowed to refine the position of these sources, and to perform optical and infrared observations which permitted to associate these new X-ray transient sources to OB supergiants companions (e.g. Halpern et al. 2004, Pellizza et al. 2006, Masetti et al. 2006, Negueruela et al. 2006b, Nespoli et al. 2008).

Thus, the fast X-ray transient behaviour of these sources and the identification of their optical counterpart with OB supergiants led to establish the existence of a new sub-class of HMXBs, called *"Supergiant Fast X-ray Transients"* by Negueruela et al. (2006a).

The members of this class exhibit sporadic fast flares with durations of a few hours, and peak luminosity of $10^{36} - 10^{37}$ erg s^{-1} (Sguera et al. 2006). A very peculiar property of SFXTs is their high dynamic range, spanning 3-5 orders of magnitude during a very short time, from a quiescent luminosity of $\sim 10^{32}$ erg s^{-1} up to the flare peak luminosity (in't Zand 2005; Leyder et al. 2007). An example of this behaviour is the fast flare of the SFXT IGR J17544-2619 observed by in't Zand (2005) with *Chandra* and reported in Figure 2.1. During this observation, IGR J17544-2619 made a fast transition from a quiescent state with $L_{\rm x} \simeq 2 \times 10^{32}$ erg s^{-1} to a peak luminosity of $L_{\rm x} \simeq 4 \times 10^{37}$ erg s^{-1}, followed by a post-flare "tail" with $L_{\rm x} \simeq 2 \times 10^{36}$ erg s^{-1}.

The *Swift* monitoring of the outburst of the SFXTs IGR J11215-5952 has allowed to discover that the outburst last a few days and is composed by many flares lasting from minutes to hours (Romano et al. 2007). This source can be monitored during its outburst thanks to the fact that it displays periodic outbursts. This behaviour was discovered by Sidoli et al. (2006), thanks to *INTEGRAL* observations. Sidoli et al. (2008), Romano et al. (2009b), Romano et al. (2008) performed a *Swift* monitoring campaign of a sample of four SFXTs (XTE J1739-302, IGR J17544-2619, IGR J16479-4514, and AX J1841.0-0536). They demonstrated that these sources display the same

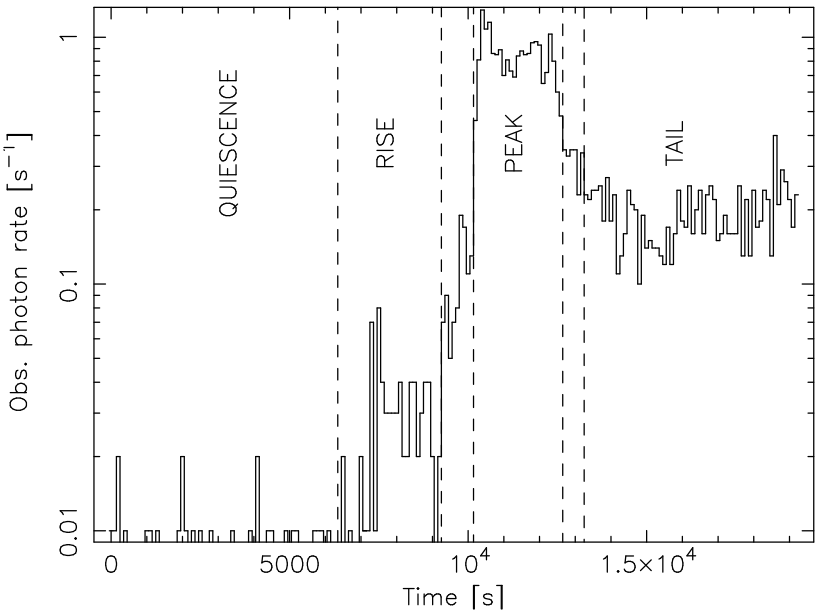

Figure 2.1: *Chandra* lightcurve of IGR J17544-2619. The photon rate at the peak is not corrected for pile-up (in't Zand 2005).

X-ray behaviour of IGR J11215-5952 on long timescales: the flares observed with *INTEGRAL* are only a part of a much larger outburst event.

Besides the bright outbursts, the *Swift* monitoring has allowed to discover that SFXTs display a fainter flaring activity with luminosity 10^{33} – 10^{34} erg s^{-1}, as shown in Figure 2.2.

The X-ray spectra display the typical shape of HMXBs hosting X-ray pulsars, with an absorbed power law with photon index of 0-1 with high energy cutoff of about 15-30 keV (see e.g. Walter & Zurita Heras 2007; Smith et al. 2006b).

Four SFXTs are X-ray pulsars: IGR J11215-5952 ($P_{\rm spin} = 186.78 \pm 0.3$ s, Swank et al. 2007), IGR J16465-4507 ($P_{\rm spin} = 228 \pm 6$ s, Lutovinov et al. 2005), AX J1841.0-0536 ($P_{\rm spin} = 4.7394 \pm 0.0008$ s, Bamba et al. 2001), IGR J18483-0311 ($P_{\rm spin} = 21.0526 \pm 0.0005$ s, Sguera et al. 2007).

To date, seven SFXTs display an orbital periodicity: IGR J11215-5952 ($P_{\rm orb} \simeq 165$ d, Sidoli et al. 2006; Romano et al. 2009c), IGR J16465-4507 ($P_{\rm orb} = 30.243 \pm 0.035$ d, La Parola et al. 2010; Clark et al. 2010), IGR J16479-4514 ($P_{\rm orb} = 3.319 \pm 0.001$ d, Jain et al. 2009), XTE J1739-302 ($P_{\rm orb} = 51.47 \pm 0.02$ d, Drave et al. 2010), IGR J17544-2619 ($P_{\rm orb} = 4.926 \pm 0.001$ d, Clark et al. 2009), SAX J1818.6-1703 ($P_{\rm orb} = 30 \pm 0.1$ d, Bird et al. 2009; Zurita Heras & Chaty 2009), IGR J18483-0311 ($P_{\rm orb} = 18.55 \pm 0.05$ d, Levine & Corbet 2006).

Up to now, there are 9 confirmed members in the class of SFXTs and

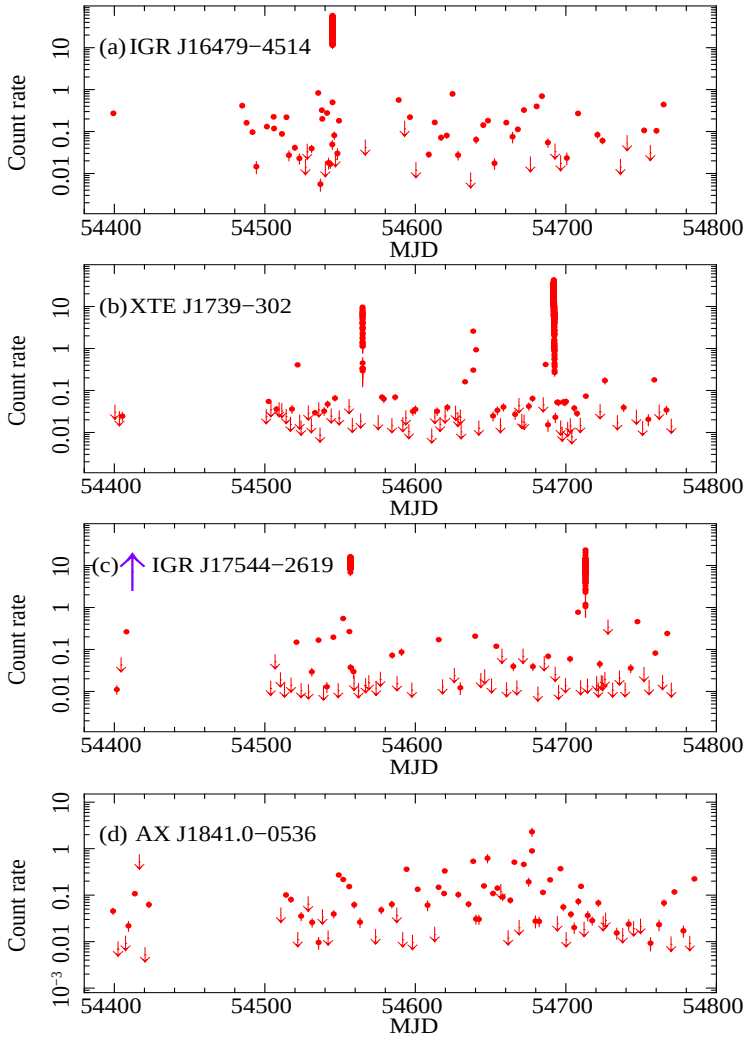

Figure 2.2: *Swift*/XRT (0.2-10 keV) lightcurves of XTE J1739-302, IGR J17544-2619, IGR J16479-4514, and AX J1841.0-0536, from 2007 October 26 to November 15. Besides the bright outbursts, it is possible to observe a fainter flaring activity. The downward-pointing arrows are $3-\sigma$ upper-limits (Romano et al. 2009b).

7 candidates. In Table 2.1 we report confirmed and candidates SFXTs together with their main properties (nature of the compact object, spectral type of the companion star, orbital period and spin period).

2.1 Accretion mechanisms in SFXTs

The accretion mechanisms at work in SFXTs are still poorly known. Up to now, different mechanisms have been proposed to explain the SFXTs properties (see Sidoli 2009 and references therein for a recent review).

2.1.1 Clumpy wind models

in't Zand (2005) proposed that the SFXTs flares are produced by accretion of clumps of matter from the companion wind. This hypothesis is supported by several observations in X-ray and other wavelenghts, which demonstrate that the winds of OB supergiants are strongly inhomogeneous. White et al. (1983) and Kreykenbohm et al. (2008) explained the X-ray variability observed in 4U 1700-37 and Vela X-1 in terms of wind inhomogeneities; further indications for the presence of clumps in the wind of OB supergiants come from X-ray spectroscopy (see e.g. Sako et al. 1999). Changes in the UV line profiles, revealing wind variability, have been observed on short time scales (< 1 d) in several observations (see e.g. Kudritzki & Puls 2000; Lépine & Moffat (2008); Markova et al. (2008) and references therein). The inhomogeneities of the wind was explained theoretically by Lucy & White (1980), which suggested that the wind acceleration is subject to a strong instability, since small perturbations in the velocity and density of the wind grow with time producing a variable and structured wind. Several time-dependent hydrodynamical simulations confirmed the hypothesis that the line driven instability produces the highly structured wind, with shocks that compress the gas into clumps (see e.g. Runacres & Owocki 2002).

Walter & Zurita Heras (2007) explain the behaviour of SFXTs as due to a neutron star with a large orbital period (i.e. orbiting at a distance 10 R_* from the donor star), accreting clumps with masses of $\sim 10^{22} - 10^{23}$ g and with a density ratio between the clumps and the outer wind of $10^2 - 10^4$.

Negueruela et al. (2008) proposed a similar model, based on the work of Oskinova et al. (2007). In this model, what distinguishes the SFXTs from the persistent HMXBs with supergiant companion is their different orbital separation: in persistent HMXBs the compact object orbits the companion star at a small distance (< 2 stellar radii) where there is a high number density of clumps. They assumed that in SFXTs the compact object orbits outside the region where the supergiant wind is denser (> 2 stellar radii). In the latter case, because of a much lower probability to accrete a single clump, the compact object show a transient behaviour with long quiescent intervals and sporadic emission of flares. However, the recent discovery of SFXTs with

Table 2.1: Known SFXTs (confirmed and candidates) and their most important parameters.

Confirmed				
Source	NS/BH	Supergiant	$P_{\rm orb}$ (d)	$P_{\rm spin}$ (s)
IGR J08408-4503 [1]	?	O8.5Ib(f) [2]	?	?
IGR J11215-5952 [3]	NS	B0.7Ia [4]	165 [5]	186.78 ± 0.3 [6]
IGR J16465-4507 [7]	NS	B0.5I/O9.5Ia [8]	30.243 ± 0.035 [9]	228 ± 6 [10]
IGR J16479-4514 [11]	?	O8.5I [12]	3.319 ± 0.001 [13]	?
XTE J1739-302 [14]	?	O8Iab [15]	51.47 ± 0.02 [16]	?
IGR J17544-2619 [17]	?	O9Ib [18]	4.926 ± 0.001 [19]	?
SAX J1818.6-1703 [20]	?	B0.5/B1 Iab [21]	30.0 ± 0.1 [22]	?
AX J1841.0-0536 [23]	NS	B0I/B1Ib [24]	?	4.7394 ± 0.0008 [23]
IGR J18483-0311 [25]	NS	B0.5 Ia [12]	18.55 ± 0.05 [27]	21.0526 ± 0.0005 [28]
Candidates				
Source	NS/BH	Supergiant	$P_{\rm orb}$ (d)	$P_{\rm spin}$ (s)
AX J1820.5-1434 [29]	NS	?	?	152.26 ± 0.04 [30]
AX J1845.0-0433 [31]	?	O9.5I [32]	?	?
IGR J16195-4945 [33]	?	B1I [12]	?	?
IGR J16207-5129 [33]	?	O7.5I [12]	?	?
IGR J17407-2808 [34]	?	?	?	?
XTE J1743-363 [35]	?	?	?	?
IGR J16418-4532 [36]	NS	O8.5 [12]	3.753 ± 0.004 [37]	1246 ± 100 [38]

[1] Gotz et al. (2006), [2] Walborn (1973), [3] Lubinski et al. (2005), [4] Negueruela et al. (2007), [5] Romano et al. (2009c), [6] Smith et al. (2006a); Swank et al. (2007), [7] Lutovinov et al. (2004), [8] Negueruela et al. (2005); Nespoli et al. (2008), [9] La Parola et al. (2010); Clark et al. (2010), [10] Lutovinov et al. (2005), [11] Molkov et al. (2003), [12] Rahoui et al. (2008), [13] Jain et al. (2009), [14] Smith et al. (1998), [15] Negueruela et al. (2006b); Smith et al. (2003), [16] Drave et al. (2010), [17] Sunyaev et al. (2003b), [18] Pellizza et al. (2006), [19] Clark et al. (2009), [20] in 't Zand et al. (1998), [21] Masetti et al. (2008); Negueruela & Smith (2006), [22] Bird et al. (2009); Zurita Heras & Chaty (2009), [23] Bamba et al. (2001), [24] Nespoli et al. (2007); Nespoli et al. (2008), [25] Chernyakova et al. (2003), [26] Rahoui & Chaty (2008), [27] Levine & Corbet (2006), [28] Sguera et al. (2007), [29] Torii et al. (1997), [30] Kinugasa et al. (1998), [31] Yamauchi et al. (1995), [32] Coe et al. (1996), [33] Walter et al. (2004), [34] Gotz et al. (2004), [35] Markwardt et al. (1999), [36] Tomsick et al. (2004), [37] Corbet et al. (2006), [38] Walter et al. (2006) .

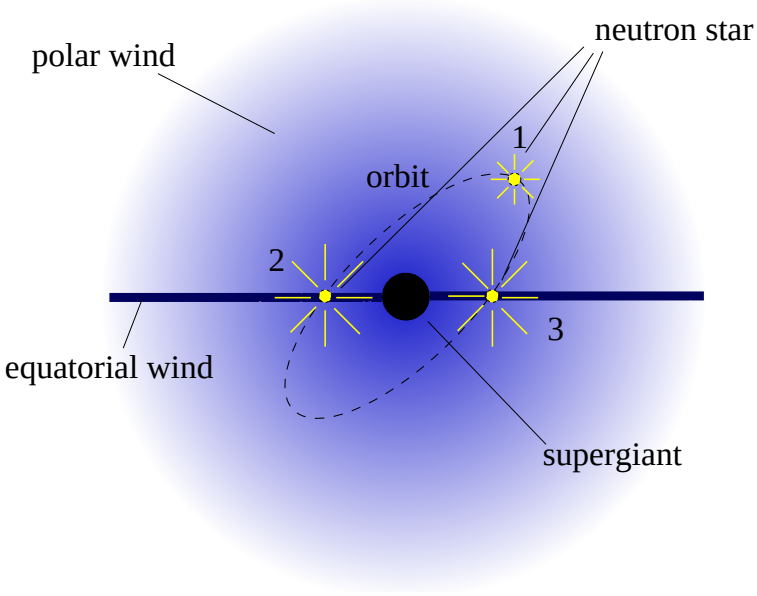

Figure 2.3: Schematic representation of the geometry for the equatorial component proposed by Sidoli et al. (2007). Labels 1, 2, 3, correspond to different positions of the neutron star along the orbit: when the neutron star is outside the equatorial plane of the supergiant the source is in a low luminosity state (1); when the neutron star crosses the equatorial wind bright outbursts are triggered (2 and 3).

short orbital periods ($P_{\rm orb} \sim 4.9$ d of IGR J17544-2619 Clark et al. 2009, and $P_{\rm orb} \sim 3.32$ d of IGR J16479-4514 Jain et al. 2009) poses problems to this explanation.

Ducci et al. (2009) developed a more detailed clumpy wind model, compared to the previous models of Walter & Zurita Heras (2007) and Negueruela et al. (2008) (see Chapter 4).

2.1.2 Anisotropic winds

Sidoli et al. (2007) proposed that the outbursts of some SFXTs could be due to the presence of a further wind component, overimposed on the spherically symmetric wind of the supergiant (Figure 2.3). The equatorial component displays a denser and slower wind than the polar wind of the supergiant. If the orbital plane of the compact object is inclined with respect to the equatorial wind component, the outbursts are produced when the compact object crosses the enhanced wind outflow. This model was proposed to explain the lightcurve of the periodic SFXT IGR J11215-5952 (Sidoli et al. 2007). Particularly interesting is the shape of the folded lightcurve of XTE J1739-302, which shows three peaks (see Figure 2.4). Drave et al. (2010) interpret

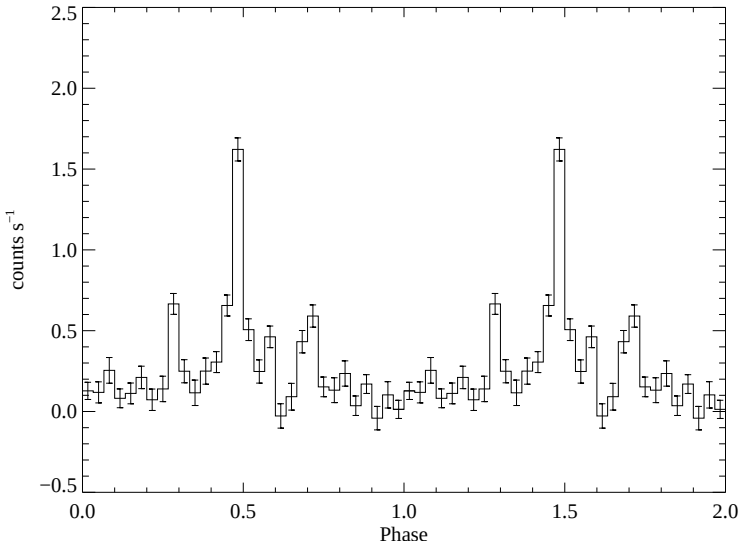

Figure 2.4: Folded lightcurve of XTE J1739-302 (IBIS/ISGRI, 18−60 keV; Drave et al. 2010).

the shape of the lightcurve using the general X-ray binary system previously modelled by Ducci et al. (2009) to show a possible orbital configuration able to explain the outburst recurrence in some SFXTs (Figure 4.20). Drave et al. (2010) explain the peak with larger luminosity at the orbital phase $\phi \approx 0.47$ as due to the periastron passage of a neutron star with an eccentric orbit, and the side-peaks at the orbital phases $\phi \approx 0.3$ and $\phi \approx 0.7$ as due to the neutron star crossing the enhanced density region inclined with respect to the orbital plane of the neutron star. If the presence of the feature at phases $\phi \approx 0.3$ and $\phi \approx 0.7$ will be confirmed with further observations, XTE J1739-302 could be the second SFXT showing an enhanced equatorial density region, as originally proposed by Sidoli et al. (2007).

The existence of preferential planes in the outflowing supergiant winds is supported by simulations suggesting that supergiants with rotational velocity similar to those measured in HMXBs (Stoyanov & Zamanov 2009), and with a dipole magnetic field ($B \gtrsim 20 - 30$ G, typical of OB supergiant) aligned to the rotation axis can produce a magnetically confined stellar wind on the equatorial plane (Ud-Doula et al. 2008).

2.1.3 Gated mechanisms

Another possibility involves the gated mechanisms, where the high dynamic ranges observed are due to transitions across the magnetic or centrifugal barrier (Grebenev & Sunyaev 2007; Bozzo, Falanga, & Stella 2008a). Grebenev & Sunyaev (2007) proposed that the steady accretion onto the

surface of the neutron star in a SFXTs is stopped because of the overcoming of a centrifugal barrier at the magnetospheric boundary of neutron star (i.e. $R_{\rm c} < R_{\rm m} < R_{\rm acc}$). Since $R_{\rm m}$ depends on the accretion rate, if $R_{\rm c}$ differs only slightly from $R_{\rm m}$, the inhibition of accretion may occur due to a small increase in the wind density, or decrease in the wind velocity (see Section 1.3.3).

Bozzo et al. (2008a) showed that a large luminosity variation (up to ~ 5 orders of magnitude) can be explained with transitions across the magnetic and centrifugal barriers if the accreting neutron star has a strong magnetic field ($\gtrsim 10^{14}$ G) and a long spin period ($P_{\rm spin} \geq 10^3$ s), and the wind of the supergiant is inhomogeneous.

To date, a direct measure of the neutron star magnetic field and a measure of a spin period larger than 10^3 s in SFXTs is still missing. Therefore, future observations might allow to discriminate between these and the other models proposed.

Chapter 3

INTEGRAL

The ESA satellite[1] *INTEGRAL (INTErnational Gamma-Ray Astrophysics Laboratory)* was launched from Baykonur (Kazakhistan) on 17^{th} October 2002 (Winkler et al. 2003). It was inserted into a geosynchronous highly eccentric orbit (72 hours) with high perigee (height of perigee of 9000 km, height of apogee of 154000 km) in order to provide long periods of uninterrupted observations with nearly constant background, and away from trapped radiation. The scientific goal of this mission is the fine spectroscopy (2.5 keV FWHM @ 1 MeV) with fine imaging and accurate positioning (angular resolution: 3 arcmin FWHM) of celestial gamma-ray sources in the energy range 3 keV−10 MeV. The fine spectroscopy permits to identify spectral features and to measure line profiles for physical studies of the source region. The fine imaging permits the location and identification of sources of gamma-ray emission with counterparts at other wavelengths, enables to distinguish point sources from extended regions and provides serendipitous science.

The *INTEGRAL* spacecraft (Jensen et al. 2003) contains all spacecraft subsystems and a payload module containing the science instruments. In particular *INTEGRAL* carries the imager IBIS (Imager on Board *INTEGRAL* Satellite, Ubertini et al. 2003), devoted to the high angular resolution imaging (15 keV − 10 MeV), the spectrometer SPI (SPectrometer on *INTEGRAL*, Vedrenne et al. 2003), devoted to the high resolution gamma-ray line spectroscopy (20 keV − 8 MeV), two X-ray monitors JEM-X (Joint European Monitor for X-ray, Lund et al. 2003) in the 3-35 keV band, and OMC (Optical Monitoring Camera, Mas-Hesse et al. 2003) in the optical (550 nm) band (see Table 3.1). All instruments are co-aligned with overlapping field of views, and they operates simultaneously. The characteristics of IBIS and JEM-X instruments, which are the more relevant instruments for this work,

[1] with contribution from Russia (PROTON launcher) and NASA (Deep Space Network ground station).

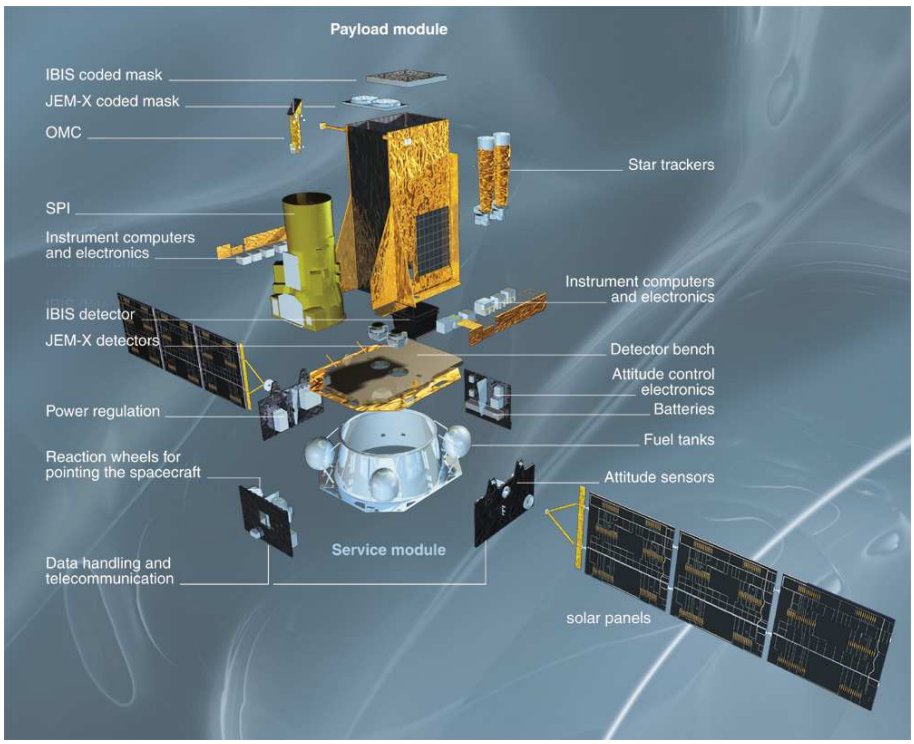

Figure 3.1: An exploded view of the *INTEGRAL* spacecraft (Image: ESA). Dimensions are ($5 \times 2.8 \times 3.2$ m). The deployed solar panels are 16 m across (Winkler et al. 2003).

are described in Sections 3.1 and 3.2. Figure 3.1 shows a schematic view of the *INTEGRAL* spacecraft with the location of the different instruments.

The strong penetration power of gamma-rays does not allow to focus high-energy photons on a given point using the standard incidence optics used by X-ray telescopes. For this reason, the high energy instruments on board *INTEGRAL* (the spectrometer SPI, the imager IBIS, and the X-ray monitors JEM-X) use the coded mask technique. The concept of coded aperture was first introduced by Dicke (1968) and Ables (1968), originally introduced to obtain an improved signal to noise ratio (SNR) for low-intensity sources (particularly X-ray sources) while maintaining high angular resolution (Fenimore & Cannon 1978). The coded mask is composed by an absorbing material with several holes, placed ahead of the detector. The shadow (called *shadowgram*) of the mask projected by the gamma-ray sources on the detector, allows to determine the images of the sky. As shown in Figure 3.2, the shadowgram is not recognizable as the object because the many holes cause the shadowgram to consist of many overlapping images. Then, the image of the object is reconstructed by decoding the detector shadowgram

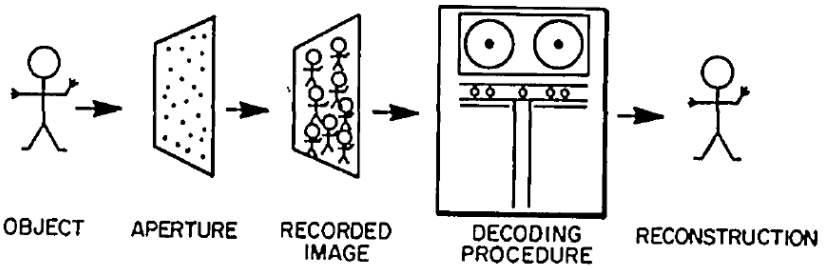

Figure 3.2: Schematic representation of the basic steps involved in coded mask technique (Fenimore & Cannon 1978).

with the mask pattern, provided that the orientation of the mask-detector system is known. The reconstruction procedure is designed to give the location and intensity of each source in the field of view. In a coded mask instrument, the angular resolution is determined by the mask pixel size C and the distance of the detector from the mask H and is given by:

$$\sigma = \arctan\left(\frac{C}{H}\right) \ .$$

The source location accuracy inside the field of view depends on the angular resolution, and it is inversely proportional to the signal to noise ratio (SNR) and the distance H:

$$d\phi = \frac{\sigma}{H \times SNR} \ .$$

If the position of a source in the field of view is known, it is possible to compute, for each detector pixel, which fraction of the sky is visible for that position, or, in other words the *Pixel Illuminated Fraction (PIF)*, knowing the detector geometry (see Figure 3.3). The comparison of the obtained PIF with the recorded shadowgram allows to extract the spectrum and the lightcurve for each source in the field of view.

3.1 Imager on Board *INTEGRAL* Satellite (IBIS)

The IBIS telescope is composed by two independent detector arrays: ISGRI (*INTEGRAL* Soft Gamma-Ray Imager, Lebrun et al. 2003), made of Cadmium-Telluride (CdTe) solid state detectors, operating in the 15−400 keV band, and PICsIT (Pixellated Imaging CaeSium Iodide Telescope, Di Cocco et al. 2003), made of Caesium-Iodide (CsI) scintillator crystals, is located below ISGRI and operates in the 180 keV − 2 MeV band. These instruments are shielded in order to minimise the background induced by high energy particles out of Van Allen belt.

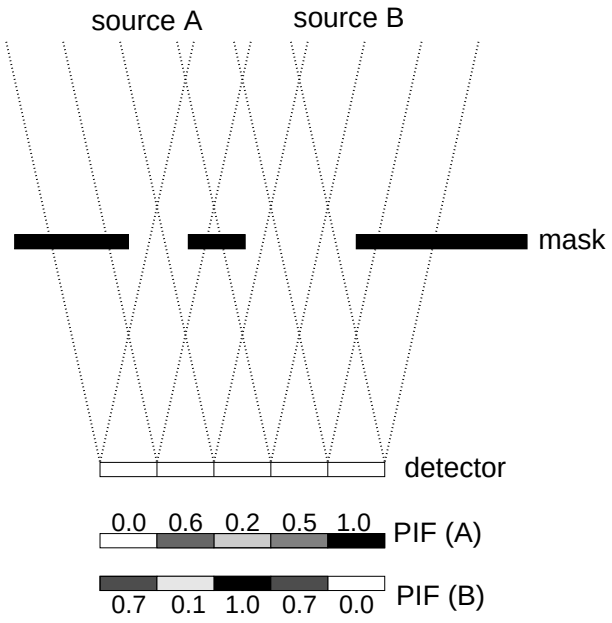

Figure 3.3: Geometric representation of the notion of *Pixel Illuminated Fraction (PIF)*.

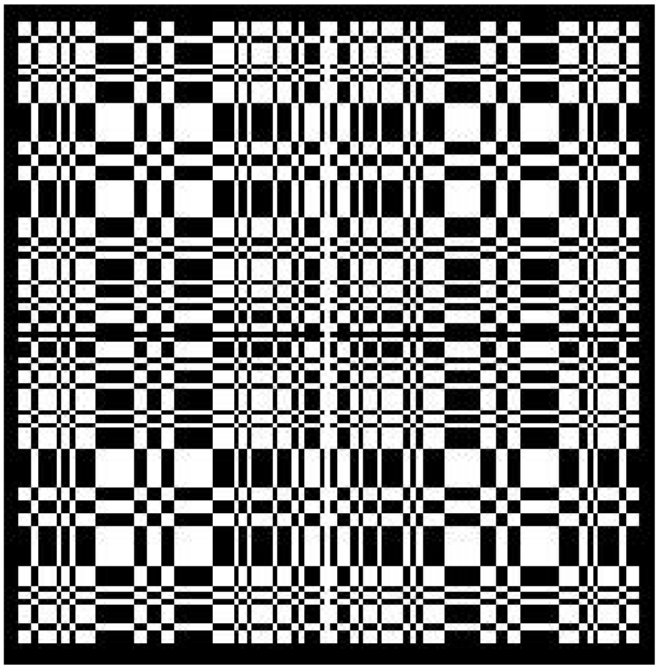

Figure 3.4: The IBIS coded mask pattern (Image: ESA).

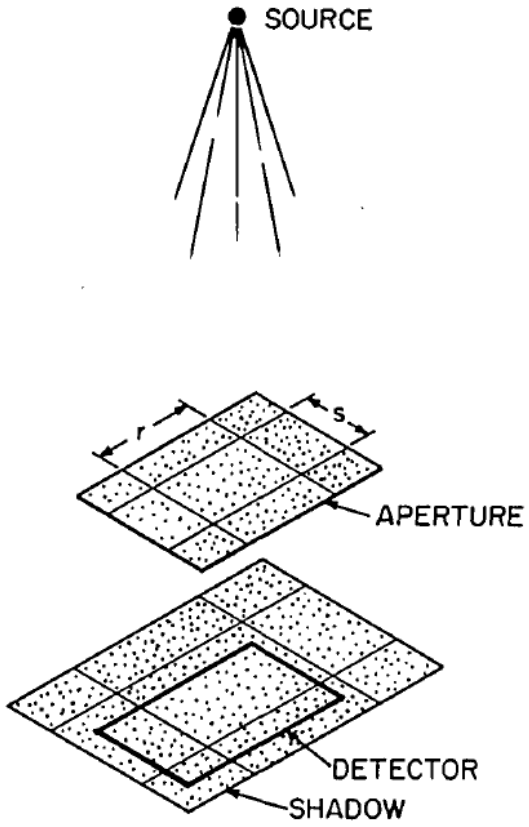

Figure 3.5: Schematic representation of the IBIS configuration. The coded aperture mask is composed of a mosaic of basic $r \times s$ patterns. An emitting source in the sky produce shadows of cyclic version of the basic aperture pattern upon the detector, which has a $r \times s$ size (Fenimore & Cannon 1978).

The detectors ISGRI and PICsIT are located at a distance of 3400 mm from a coded mask with dimensions $1064 \times 1064 \times 16$ mm^3 made up of 95×95 individuals cells of size 11.2×11.2 mm^2. The geometry of this mask is based on a cyclic replication of MURA (Modified Uniformly Redundant Array) of order 53 (see Gottesman & Fenimore 1989). 50% of the mask cells are made of Tungsten, and are opaque to photons in the operational energy range of the IBIS instrument (e.g. 70% opacity @ 1.5 MeV). The other 50% of cells are open (transparency of 60% @ 20 keV). Figure 3.4 shows the mask pattern of IBIS.

The configuration of the IBIS instrument has a mask ~ 1.8 times larger than the detector. The mask is made of cyclic repetition of a base pattern of the same size of the detector (see Figure 3.5). The most important advantage of such configuration is the large field of view with respect to the size of the detector. On the other hand, this configuration has the disadvantage that in

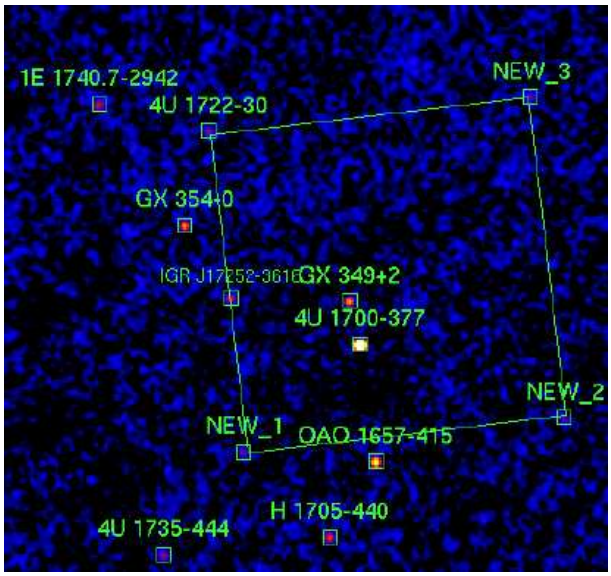

Figure 3.6: IBIS/ISGRI image. Three ghosts are visible (called "NEW_1", "NEW_2", "NEW_3") of the source 4U 1722-30 (Image of the IBIS Analysis User Manual: `http://www.isdc.unige.ch/integral/download/osa_doc`).

the reconstructed image of the sky a point source does not produce a single narrow peak, but also other spurious peaks, called ghosts, in well defined sky positions (see Figure 3.6).

The configuration coded mask-detectors of IBIS enables different way in which a source can project a shadow of the mask on the detector. If the detector is fully illuminated, the recorded shadow is a complete permutation of the mask base pattern: in this case the source is said to be in the Fully Coded Field Of View (FCFOV). If only a part of the detector is illuminated, the shadow is only a subset of the complete pattern and the source is in the Partially Coded Field Of View (PCFOV). IBIS has a FCFOV of $9° \times 9°$ and a PCFOV of $29° \times 29°$. The angular resolution is 12 arcmin, and the location accuracy is $1'$ for a 10σ detection.

3.2 Joint European Monitor for X-ray (JEM-X)

JEM-X allows the spectral, imaging and timing study of the sources detected by IBIS and SPI, and may provide independent scientific results from sources with soft spectrum (3−35 keV). The instrument consists of two co-aligned coded mask telescopes, JEM-X1 and JEM-X2, which are switched on alternatively during the mission.

The JEM-X masks are based on a Hexagonal Uniformly Redundant Ar-

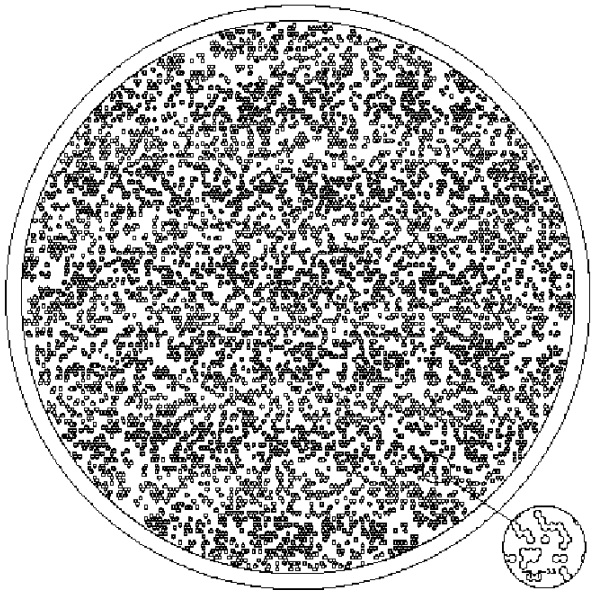

Figure 3.7: The JEM-X coded mask pattern (Image of the JEM-X Analysis User Manual: `http://www.isdc.unige.ch/integral/download/osa_doc`).

ray (HURA, Figure 3.7). The pattern is composed of 22501 elements (with dimensions of 3.3 mm) with only 25% open area. Its angular resolution ($3.35'$) is better than IBIS, which allows for a better point source location accuracy ($15''$ for a 10σ detection). The field of view has a diameter of 4.8°.

Each JEM-X detector, located at a distance of 3.4 m from the coded mask, consists of a high-pressure microstrip gas chambers, with a mixture of xenon (90%) and methane (10%).

3.3 IBIS and JEM-X data analysis

INTEGRAL observations consists of pointings (of $\sim$ 2000 s each), called Science Windows (ScWs). From one Science Window to another the pointing follow a dithering or a survey strategy as chosen in the observing program (Winkler et al. 2003).

The reduction and analysis of IBIS and JEM-X data is performed by the Off-line Science Analysis (OSA) software (Goldwurm et al. 2003), which starts from the data files obtained by the *INTEGRAL* Science Data Center (ISDC; Courvoisier et al. 2003), and performs a number of analysis steps. Using some informations provided by the user, such as the input catalog of sources, the number of images of the sky corresponding to different energy bands to create for each ScW, the spectral binning, and the time bins of the

lightcurves, OSA performs the data analysis in the following order:

- Data are prepared:
  - computation of the livetimes of the single pixels;
  - calculations of the deadtimes during which the incoming photons may be lost due to the processing of the previous events;
  - computation of the deposited energies for all events;
- Images are extracted: for each energy range, the intensity shadowgram is created and cleaned with the available background maps provided by the IBIS and JEM-X team. The shadowgrams are deconvolved and the sky images are reconstructed for each ScW, and combined to obtain mosaic of sky image of the whole observation. Then, the source search is performed in the single images and in the mosaic;
- The spectra of each source are extracted: for each source in the FOV, a model of the source contribution in each energy band (i.e. the Pixel Illuminated Function, PIF) is built, then the spectra of the sources are extracted by performing image binning and correction on small energy bands;
- Lightcurves of each source are extracted: given the PIF obtained at the spectrum level, the lightcurves of the sources from the input catalog are extracted[2].

[2]For more informations, see:
`http://isdcul3.unige.ch/Soft/download/osa/osa_doc/osa_doc-9.0/osa_um_ibis-9.2.pdf`
and: `http://isdcul3.unige.ch/Soft/download/osa/osa_doc/osa_doc-9.0/osa_um_jemx-9.2.pdf`

Parameter	SPI	IBIS
Energy range	18 keV - 8 MeV	15 keV - 10 MeV
Detector	19 Ge detectors, each (6×7) cm cooled @ 85 K	16384 CdTe detectors, each $(4 \times 4 \times 2)$ mm 4096 CsI detectors, each $(8.4 \times 8.4 \times 30)$ mm
Detector area cm^2	500	2600 (CdTe), 2890 (CsI)
Spectral resolution	3 keV @ 1.7 MeV	8 keV @ 100 keV
Continuum sensitivity (photons cm^{-2} s^{-1} keV^{-1}) ($\Delta E = E/2, 3\sigma, 10^6$ s)	5.5×10^{-6} @ 100 keV 1.2×10^{-6} @ 1 MeV	6×10^{-7} @ 100 keV 5×10^{-7} @ 1 MeV
Line sensitivity (photons cm^{-2} s^{-1}) ($3\sigma, 10^6$ s)	3.3×10^{-5} @ 100 keV 2.4×10^{-5} @ 1 MeV	1.9×10^{-5} @ 100 keV 3.8×10^{-4} @ 1 MeV
Field of view (fully coded)	16°	$9^\circ \times 9^\circ$
Angular resolution	2.5°	$12'$
Source location	$\leq 1.3^\circ$	$\leq 1'$ (for 10σ)
Parameter	**JEM-X**	**OMC**
Energy range	4 keV - 35 keV	500 nm - 600 nm
Detector	Xe/CH_4 gas detector	CCD + V-filter
Detector area cm^2	500	(2061×1056) pixels
Spectral resolution	2.0 keV @ 22 keV	-
Continuum sensitivity (photons cm^{-2} s^{-1} keV^{-1}) ($\Delta E = E/2, 3\sigma, 10^6$ s)	1.2×10^{-5} @ 6 keV 1.3×10^{-5} @ 30 keV	- -
Line sensitivity (photons cm^{-2} s^{-1}) ($3\sigma, 10^6$ s)	1.9×10^{-5} @ 6 keV 8.5×10^{-5} @ 30 keV	- -
Limiting magnitude (mag) ($3\sigma, 5000$ s)	-	17.8
Field of view (fully coded)	4.8°	$5^\circ \times 5^\circ$
Angular resolution	$3'$	$25''$
Source location	$\leq 30''$ (10σ)	$6''$ (10σ)

Table 3.1: *INTEGRAL* main characteristics (Winkler et al. 2003).

Chapter 4

Clumpy stellar winds model

4.1 Introduction

A new class of massive X-ray binaries has been recognized in the last few years, mainly thanks to observations carried out with the *INTEGRAL* satellite. They are transient X-ray sources associated to O or B supergiant stars and characterized by short outbursts. These *Supergiant Fast X−ray Transients* (SFXTs) (Sguera et al. 2005; Negueruela et al. 2006b) are remarkably different from the classical High Mass X-ray Binaries (HMXBs) with supergiant companions, that are bright persistent sources, and also differ from the Be transients for their optical companions and shorter outbursts.

The outbursts of SFXTs involve a high dynamic range, spanning 3 to 5 orders of magnitudes, from a quiescent luminosity of $\sim 10^{32}$ erg s^{-1} up to the peak luminosity of $10^{36} - 10^{37}$ erg s^{-1}. The outbursts typically last a few days and are composed of many short flares with a duration of a few hours. Besides these bright outbursts, the SFXTs can display a fainter flaring activity with luminosity $L_{\rm x} = 10^{33} - 10^{34}$ erg s^{-1} (Sidoli et al. 2008).

The winds of O and B type stars are driven by the momentum transfer of the radiation field and Lucy & Solomon (1970) showed that the dominant mechanism is the line scattering. The analytical formulation for line-driven winds has been developed by Castor et al. (1975) (CAK). In the CAK theory the mass lost by the star is smoothly accelerated by the momentum transferred from the stellar continuum radiation, and forms a stationary and homogeneous wind. However, both observational evidence and theoretical considerations indicate that the stellar winds are variable and non homogeneous. Changes in the UV line profiles, revealing wind variability, have been observed on time scales shorter than a day (Kudritzki & Puls 2000). The X-ray variability observed in 4U 1700−377, Vela X−1 and other HMXBs can be explained in terms of wind inhomogeneity (White et al. 1983; Kreykenbohm et al. 2008) and further indications for the presence of

clumps come from X−ray spectroscopy. For example, the X−ray spectrum of Vela X−1 during the eclipse phase shows recombination lines produced by a hot ionized gas and fluorescent K-shell lines produced by cool and dense gas of near-neutral ions (Sako et al. 1999). These authors proposed that the coexistence of highly ionized and near neutral ions can be explained with an inhomogeneous wind, where cool, dense clumps are embedded in a lower density, highly ionized medium.

Lucy & White (1980) suggested that the wind acceleration is subject to a strong instability since small perturbations in the velocity or density distribution grow with time producing a variable and strongly structured wind. The first time-dependent hydrodynamical simulations of unstable line-driven winds were performed by Owocki et al. (1988) and, more recently, by Runacres & Owocki (2002). These simulations show that the line-driven instability produces a highly structured wind, with reverse and forward shocks that compress the gas into clumps. Moreover, the shock heating can generate a hot inter-clump medium where colder clumps are immersed (Carlberg 1980).

Based on these considerations, we study in this work the expected variability and X−ray luminosity properties of neutron stars accreting from a clumpy wind. In the next two Sections we describe our clumpy wind model and the assumptions for the mass accretion. In Section 4.4 we study the dependence of the parameters introduced in the previous sections. In Sections 4.6, 4.7, 4.8, and 4.9 we compare the X-ray light curves predicted with our model to the observations of four high mass X-ray binaries, showing that it is possible to well reproduce the observed flaring behaviour.

4.2 Clumpy stellar wind properties

In our model, where the dynamical problem has not been treated, we assume that a fraction of the stellar wind is in form of clumps with a power law mass distribution

$$p(M_{\rm cl}) = k \left(\frac{M_{\rm cl}}{M_{\rm a}} \right)^{-\zeta} \tag{4.1}$$

where k is the normalization constant, $M_{\rm a}$ - $M_{\rm b}$ is the mass range, and ζ is the scaling parameter. Integrating the probability density we obtain the normalization constant:

$$\int_{M_{\rm a}}^{M_{\rm b}} p(M_{\rm cl}) dM_{\rm cl} = 1 \Longrightarrow k = (1-\zeta) \frac{M_{\rm a}^{-\zeta}}{M_{\rm b}^{1-\zeta} - M_{\rm a}^{1-\zeta}} \ . \tag{4.2}$$

We assume that the total mass loss rate of the supergiant is given by:

$$\dot{M}_{\rm tot} = \dot{M}_{\rm cl} + \dot{M}_{\rm wind} \tag{4.3}$$

where $\dot{M}_{\rm cl}$ is the mass loss rate component due to the clumps and $\dot{M}_{\rm wind}$ is the mass loss rate in the form of the inter-clump medium. The total number of clumps produced by the supergiant is related to the total mass loss rate by means of the following equation:

$$\dot{N}_{\rm cl} = \frac{f\dot{M}_{\rm tot}}{< M >} \quad \text{clumps s}^{-1} \tag{4.4}$$

where $f = \dot{M}_{\rm cl}/\dot{M}_{\rm tot}$ is the fraction of wind mass in the form of clumps, and

$$< M >= \int_{M_{\rm a}}^{M_{\rm b}} p(M_{\rm cl}) M_{\rm cl} dM_{\rm cl}$$

is the average mass of a clump produced by the supergiant.

Clumps are driven radially outward by absorption of UV spectral lines Castor et al. (1975). From spectroscopic observations of O stars, Lépine & Moffat (2008) suggest that clumps follow on average the same velocity law of a smooth stellar wind. We can then assume the following clump velocity profile without solving the dynamical problem:

$$v_{\rm cl}(r) = v_\infty \left(1 - 0.9983 \frac{R_{\rm OB}}{r}\right)^\beta \tag{4.5}$$

where v_∞ is the terminal wind velocity, $R_{\rm OB}$ is the radius of the supergiant, 0.9983 is a parameter which ensures that $v(R_{\rm OB}) \approx 10$ km s^{-1}, and β is a constant in the range $\sim 0.5-1.5$ (Lamers & Cassinelli 1999; Kudritzki et al. 1989).

Assuming that the clumps are confined by the ram pressure of the ambient gas, their size can be derived by the balance pressure equation. Following Lucy & White (1980) and Howk et al. (2000), the average density of a clump is:

$$\bar{\rho}_{\rm cl} = \rho_{\rm w}(r) \left(\frac{a_{\rm w}^2 + C_\rho \omega^2}{a_c^2}\right) \tag{4.6}$$

where $\rho_{\rm w}(r)$ is the density profile of the homogeneous (inter-clump) wind, $a_{\rm w}$ and a_c are the inter-clump wind and the clump thermal velocity, respectively: $a_{\rm w}^2 = \frac{kT_{\rm w}}{\mu m_H}$ and $a_c^2 = \frac{kT_c}{\mu m_H}$. k is the Boltzmann constant, $T_{\rm w}$ and T_c are the temperatures of the inter-clump wind and of the clumps, respectively, and μ is the mean atomic weight. The constant $C_\rho = 0.29$ accounts for the confining effect of the bow shock produced by the ram pressure around the clump (Lucy & White 1980). ω is the relative velocity between the wind and the clump ($\omega = v_{\rm w} - v_{\rm cl}$). Adopting $\bar{\omega} \sim 5 \times 10^7$ cm s^{-1}, $\bar{T}_c \sim 10^5$ K, $\bar{T}_{\rm w} \sim 10^7$ K and $\mu = 1.3$, we obtain[1]:

$$\left(\frac{a_{\rm w}^2 + C_\rho \omega^2}{a_{\rm c}^2}\right) \approx 200 \ . \tag{4.7}$$

[1]This value is just an estimate of a typical value of ratio of clump to ambient density, and will not adopted throughout.

Since the density radial profile $\rho_{\rm w}(r)$ of the homogeneous inter-clump wind (obtained from the continuity equation $\dot{M} = 4\pi r^2 \rho_{\rm w}(r) v(r) = \ constant$) is:

$$\rho_{\rm w}(r) = \rho_{\rm w}(r_0) \frac{r_0^2 v(r_0)}{r^2 v(r)} \tag{4.8}$$

where r_0 is a generic distance from the supergiant, from Equations (4.6), (4.7), (4.8), we obtain:

$$\bar{\rho}_{\rm cl}(r) = \bar{\rho}_{\rm cl}(r_0) \frac{r_0^2 v(r_0)}{r^2 v(r)} \tag{4.9}$$

where $\bar{\rho}_{\rm cl}(r_0) = \rho_{\rm w}(r_0) \times (a_{\rm w}^2 + C_\rho \omega^2)/a_{\rm c}^2$. Bouret et al. (2005) analyzed the far-ultraviolet spectrum of O-type supergiants and found that clumping starts deep in the wind, just above the sonic point $R_{\rm s}$, at velocity $v(R_{\rm s}) \approx 30$ km s^{-1}. In the CAK model the sonic point is defined as the point where the wind velocity is equal to the sound speed ($v(R_{\rm s}) = c_{\rm s}$):

$$R_{\rm s} = \frac{0.9983 R_{\rm OB}}{1 - (c_{\rm s}/v_\infty)^{1/\beta}} \ . \tag{4.10}$$

Adopting typical parameters for O supergiants, from Equation (4.10) we obtain that the clumping phenomenon starts close to the photosphere ($R_{\rm s} \approx R_{\rm OB}$). Assuming spherical geometry for the clumps and that the mass of each clump is conserved, it is possible to obtain the expansion law of the clumps from Equation (4.9), with $r_0 = R_{\rm s}$:

$$R_{\rm cl}(r) = R_{\rm cl}(R_{\rm s}) \left[\frac{r^2 v_{\rm cl}(r)}{R_{\rm s}^2 v(R_{\rm s})} \right]^{1/3} \ . \tag{4.11}$$

From Equation (4.11) we find that the clump size increases with the distance from the supergiant star.

For the initial clump dimensions we tried two different distributions, a power law

$$\dot{N}_{M_{cl}} \propto R_{\rm cl}^{\gamma} \quad \text{clumps s}^{-1} \tag{4.12}$$

and a truncated gaussian function:

$$\dot{N}_{M_{cl}} \propto \frac{1}{\sigma\sqrt{2\pi}} e^{-\frac{1}{2}\left(\frac{R_{\rm cl} - \bar{R}_{\rm cl}}{\sigma}\right)^2} \quad \text{clumps s}^{-1} \tag{4.13}$$

where $\sigma = (R_{\rm cl,max} - R_{\rm cl,min})/(2N_\sigma)$, and N_σ is a free parameter.

For any given mass clump we derived the minimum and maximum values for the initial radii as follows. The minimum radius is that below which the clump is optically thick for the UV resonance lines. In this case gravity dominates over the radiative force causing the clump to fall back onto the supergiant. The momentum equation of a radiatively driven clump is:

$$v_{\rm cl} \frac{dv_{\rm cl}}{dr} = -\frac{GM_{\rm OB}}{r^2} + g_{\rm e} + g_{\rm L} \tag{4.14}$$

where $M_{\rm OB}$ is the mass of the supergiant, $g_{\rm e}$ is the radiative acceleration due to the continuum opacity by electron scattering, $g_{\rm L}$ is the radiative acceleration due to line scattering. While Equation (4.14) is an approximation that ignores the pressure gradient, the solution of the momentum equation differs only slightly from the accurate solution derived by Kudritzki et al. (1989); another assumption is that the photosphere has been treated as a point source (Lamers & Cassinelli 1999). The radiative acceleration due to electron scattering is:

$$g_{\rm e}(r) = \frac{\sigma_{\rm e}(r) L_{\rm OB}}{4\pi r^2 c} \tag{4.15}$$

where $\sigma_{\rm e}$ is the opacity for electron scattering, and is given by $\sigma_{\rm e} = \sigma_{\rm Th}\frac{n_{\rm e}}{\rho_{\rm cl}}$, where $\sigma_{\rm Th}$ is the Thomson cross section, $n_{\rm e}$ is the number density of electrons, $\rho_{\rm cl}$ is the density of the clump and $L_{\rm OB}$ is the luminosity of the OB supergiant. Lamers & Cassinelli (1999) found $0.28 < \sigma_{\rm e} < 0.35\ cm^2\ g^{-1}$. Assuming a constant degree of ionization in the wind both $\sigma_{\rm e}$ and $g_{\rm e}$ are constant.

The radiative acceleration due to the line scattering is:

$$g_{\rm L} = \frac{\sigma_{\rm e}^{\rm ref} L_{\rm OB}}{4\pi c r^2} k t^{-\alpha} \left(10^{-11}\frac{n_{\rm e}}{W}\right)^{\delta} \tag{4.16}$$

where $\sigma_{\rm e}^{\rm ref} = 0.325\ {\rm cm}^2\ {\rm g}^{-1}$, k, α, δ are the force multiplier parameters, which are obtained with the calculation of the line radiative force Abbott (1982). t is the dimensionless optical depth parameter (Castor et al. 1975). According to the model of Howk et al. (2000), we assume no velocity gradient inside the clump (of size $l \approx 2R_{\rm cl}$), then we utilize the dimensionless optical depth parameter for a static atmosphere $t = \sigma_{\rm e}\int_l \rho dr$. $W(r)$ is the geometrical dilution factor (Lamers & Cassinelli 1999), given by Equation (1.25). According to the Equation (4.9), we find that the number density of electrons in each clump is given by:

$$n_{\rm e}(r) = n_0 \frac{R_{\rm s}^2 v(R_{\rm s})}{r^2 v(r)} \tag{4.17}$$

where $n_0 = n_{\rm e}(R_{\rm s})$ such that:

$$n_0 = \frac{\rho_{\rm cl}(R_{\rm s})}{\mu_{\rm e} m_{\rm H}}\ . \tag{4.18}$$

From Equation (4.14) we obtain that the minimum radius of the clump is given by:

$$g_{\rm L} + g_{\rm e} - g_{\rm g} = 0 \tag{4.19}$$

where $g_{\rm g}$ is the acceleration due to gravity. Approximating t as

$$t \approx \sigma_{\rm e}\frac{M_{\rm cl}}{V_{\rm cl}} 2R_{\rm cl} = \frac{3}{2}\sigma_{\rm e}\frac{M_{\rm cl}}{\pi R_{\rm cl}^2} \tag{4.20}$$

and assuming the force multiplier parameters calculated by Shimada et al. (1994), with $v(R_s) = 30$ km s^{-1} and $r_0 = R_s$, we finally obtain the lower-limit for the clump radius:

$$R_{\rm cl,min}(M_{\rm cl}) = \left(\frac{A \cdot B}{C}\right)^{1/(3\delta - 2\alpha)} \tag{4.21}$$

where:

$$A = \left(\frac{3\sigma_e M_{\rm cl}}{2\pi}\right)^{-\alpha} \tag{4.22}$$

$$B = \left(\frac{3M_{\rm cl}10^{-11}}{4\pi\mu_e m_H W(R_s)}\right)^{\delta} \tag{4.23}$$

$$C = (g_g - g_e)\frac{4\pi c R_s^2}{\sigma_e^{\rm ref} L_{\rm OB} k} \ . \tag{4.24}$$

We found that for the interesting range of the clump masses, the drag force (Lucy & White 1980) values are less than 3% of the forces resulting from Equations (4.15) and (4.16). Thus, in the determination of the minimum clump radius, we can neglect this contribution.

The upper-limit to the clump radius is obtained from the definition of a clump as an over-density with respect to the inter-clump smooth wind:

$$\rho_{\rm cl} \geq \frac{\dot{M}_w}{4\pi R_s^2 v_w(R_s)} \tag{4.25}$$

where $\dot{M}_w$ is the mass loss rate of the homogeneous wind component (inter-clump). From Equation (4.25) we obtain the upper-limit for the clump radius

$$R_{\rm cl,max}(M_{\rm cl}) = \left(\frac{3M_{\rm cl}R_s^2 v_w(R_s)}{\dot{M}_w}\right)^{1/3} \ . \tag{4.26}$$

The lower and the upper limits for the clump radius (Equations 4.21 and 4.26) depend on the supergiant parameter $T_{\rm eff}$, $L_{\rm OB}$, $R_{\rm OB}$, v_∞, β, $\dot{M}_w$. Thus supergiants of different spectral type have, for any given mass of the clump, different minimum and maximum values for the initial radii distribution. However, these differences are smaller than a factor 10 for OB supergiants, and the intersection of the upper-limit and lower-limit functions ranges from $M_{\rm cl} \approx 10^{20}$ g to $\approx 10^{23}$ g.

4.3 X-ray luminosity

The Bondi-Hoyle-Lyttleton accretion theory (Hoyle & Lyttleton 1939; Bondi & Hoyle 1944) is usually applied to the HMXBs where a OB supergiant loses mass in the form of a fast stellar wind, (terminal velocity, $v_\infty \approx 1000 - 2000$ km s^{-1}), that is assumed to be homogeneous and spherically symmetric.

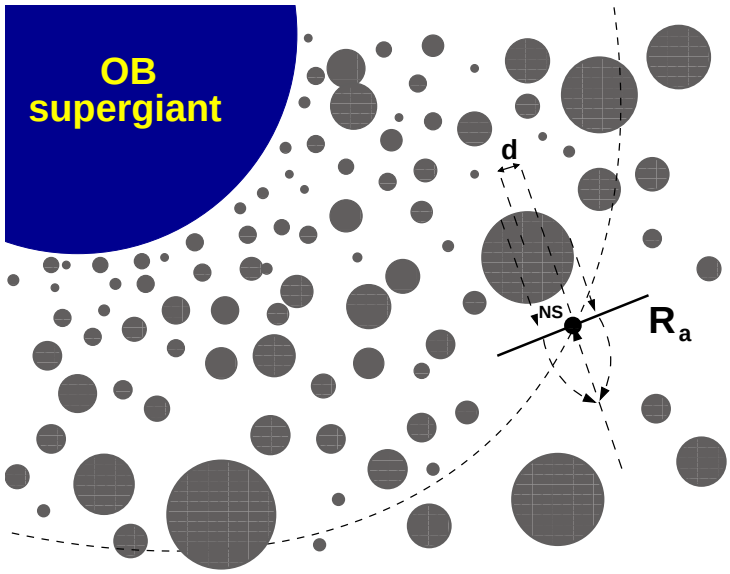

Figure 4.1: Schematic representation of our clumpy wind model. d is the distance between the centre of the clump and the centre of accreting compact object. $R_{\rm a}$ is the accretion radius.

The Bondi-Hoyle-Lyttleton accretion theory requires an important modification to properly take into account the presence of inhomogeneity in a clumpy wind. In the homogeneous case the wind particles are deflected by the gravitational field of the neutron star, and collide with the particles having the symmetric trajectory in a cylindrical region with axis along the relative wind direction. The collisions dissipate the kinetic energy perpendicular to this axis, and only the particles with a parallel kinetic energy component lower than the gravitational potential energy are accreted. The application of this accretion mechanism to an inhomogeneus wind can lead to a partial accretion of the clump: when the distance d between the neutron star and the projection of the centre of the clump on the accretion cross section is smaller than the clump radius and $d \neq 0$, only a fraction of the mass of the clump will be accreted (see Figure 4.1). In particular, if an incoming clump that crosses the accretion cross-section $\pi R_{\rm acc}^2$, is smaller than the accretion radius ($R_{\rm cl} < R_{\rm acc}$) and $d < R_{\rm cl}$, the accretion cross-section in Equation (1.17) must be replaced by

$$\Sigma = 4 \int_{d}^{R_{\rm cl}} \sqrt{R_{\rm cl}^2 - x^2} dx \tag{4.27}$$

and the mass accretion rate is $\dot{M}_{\rm acc} = \rho_{\rm cl}(r) v_{\rm rel}(r) \times \Sigma$ (see Figure 4.2,A). If $R_{\rm cl} \geq R_{\rm acc}$ we have three cases:

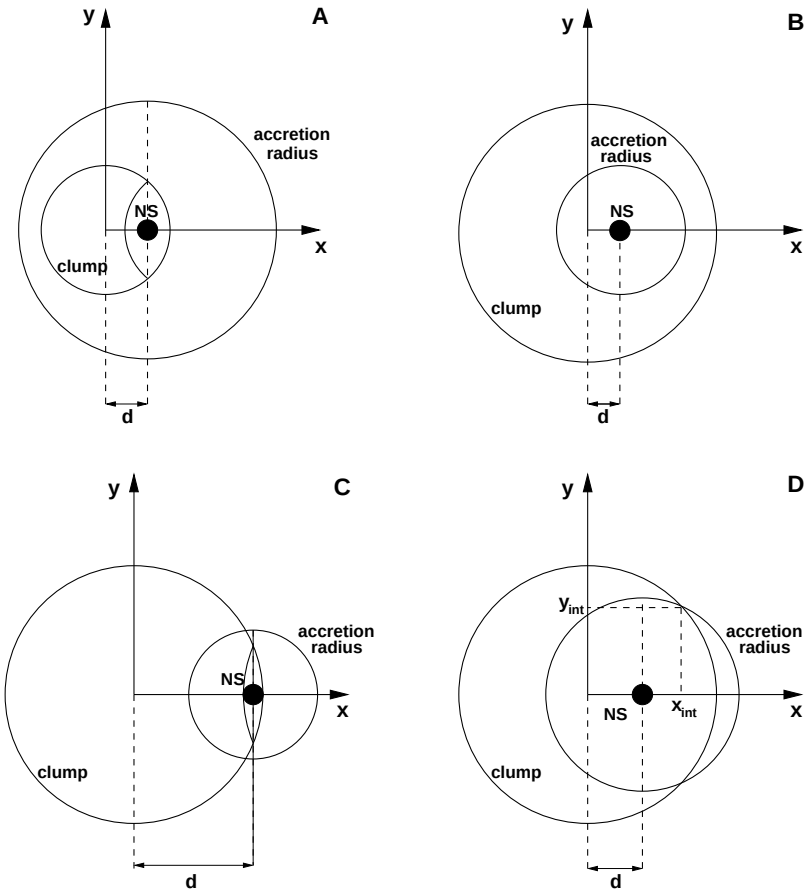

Figure 4.2: Schematic view of different possibilities for the accretion of clumps of radius $R_{\rm cl}$. A: $R_{\rm cl} \leq R_{\rm acc}$ and $d \neq 0$ (Eq. 4.27); B: $R_{\rm cl} > R_{\rm acc}$ and $R_{\rm cl} - d \geq R_{\rm acc}$ (Eq. 4.28); C: $R_{\rm cl} - d < R_{\rm acc}$ and $\sqrt{R_{\rm cl}^2 - d^2} < R_{\rm acc}$ (Eq. 4.27); D: $R_{\rm cl} - d < R_{\rm acc}$ and $\sqrt{R_{\rm cl}^2 - d^2} > R_{\rm acc}$ (Eq. 4.29).

- when $R_{\rm cl} - d \geq R_{\rm acc}$ (Figure 4.2,B), the accretion cross-section is given by:

$$\Sigma = \pi R_{\rm acc}^2 \tag{4.28}$$

- when $R_{\rm cl} - d < R_{\rm acc}$ and $\sqrt{R_{\rm cl}^2 - d^2} < R_{\rm acc}$ (Figure 4.2,C), the accretion cross-section is given by Equation (4.27).

- when $R_{\rm cl} - d < R_{\rm acc}$ and $\sqrt{R_{\rm cl}^2 - d^2} > R_{\rm acc}$ (Figure 4.2,D), the accretion cross-section is given by:

$$\begin{aligned} \Sigma &= 4\left[\int_{x_{int}}^{R_{\rm cl}} \sqrt{R_{\rm cl}^2 - x^2}dx - (x_{int} - d)y_{int} + \right. \\ &+ \left. \int_{y_{int}}^{R_{\rm acc}} \sqrt{R_{\rm acc}^2 - y^2}dy\right] \end{aligned} \tag{4.29}$$

The number density of clumps $n_{\rm cl}$ obeys the equation of continuity $\dot{N}_{\rm cl} = 4\pi r^2 n_{\rm cl}(r) v_{\rm cl}(r)$, where $\dot{N}_{\rm cl}$ is the rate of clumps emitted by the OB supergiant (see Equation 4.1). Thus:

$$n_{\rm cl}(r) = \frac{\dot{N}_{\rm cl}}{4\pi r^2 v_{\rm cl}(r)} \quad \text{clumps cm}^{-3} \tag{4.30}$$

The rate of clumps accreted by the neutron star is given by:

$$\dot{N}_{\rm accr} = n_{\rm cl}(r) v_{\rm rel}(r) \times (\pi R_{\rm acc}^2) \quad \text{clumps s}^{-1} \tag{4.31}$$

When the neutron star accretes only the inter-clump wind, the X−ray luminosity variations are due to changes in its distance from the OB companion due to orbital eccentricity. The corresponding luminosity (see Equations 1.15 and 1.17) is:

$$L_{\rm x,wind}(\phi) = \frac{GM_{\rm NS}}{R_{\rm NS}}\dot{M}_{\rm acc} = \frac{(GM_{\rm NS})^3}{R_{\rm NS}} \frac{4\pi\rho_{\rm w}(r)}{[(v_{\rm rel}^2(r) + c_s^2]^{3/2}} \tag{4.32}$$

where ϕ is the orbital phase, and $\rho_{\rm w}(r)$ is given by the Equation (4.8).

When the neutron star accretes a clump its X−ray luminosity is given by:

$$L_{\rm x,cl}(\phi) = \frac{GM_{\rm NS}}{R_{\rm NS}} \frac{M_{\rm cl}}{\frac{4}{3}\pi R_{\rm cl}^3} v_{\rm rel} \times \Sigma \tag{4.33}$$

where $R_{\rm cl}(r)$ is given by the Equation (4.11), and Σ by the Equations (4.27), (4.28), and (4.29). If two or more clumps are accreted at the same time, the X−ray luminosity at the peak of the flare produced by the accretion is given by the sum of the luminosities (Equation 4.33) produced by the accretion of each clump.

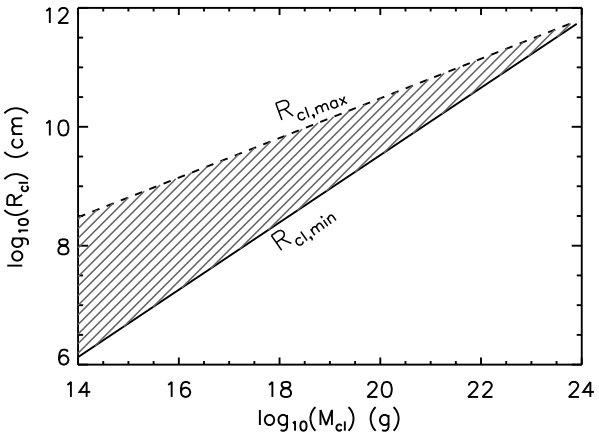

Figure 4.3: Upper (dashed line) and lower-limit (solid line) for the clump radius at $r = R_{\rm s}$. They have been obtained from Equations (4.21) and (4.26) assuming the following parameters for the supergiant: $M_{\rm OB} = 30$ M$_\odot$, $R_{\rm OB} = 23.8$ R$_\odot$, $\dot{M}_{\rm tot} = 10^{-6}$ M$_\odot$ yr^{-1}, $v_\infty = 1700$ km s^{-1}, $\beta = 1$, $v_0 = 10$ km s^{-1}, $\dot{M}_{\rm cl}/\dot{M}_{\rm wind} = 0.7$.

4.4 Application of the clumpy wind model

In this section we investigate how the X-ray luminosity and variability properties depend on the different clumpy wind parameters and orbital configurations.

As an example, we consider a binary consisting of an O8.5I star with $M_{\rm OB} = 30$ M$_\odot$, $R_{\rm OB} = 23.8$ R$_\odot$ (Vacca et al. 1996), and a neutron star with $M_{\rm NS} = 1.4$ M$_\odot$, $R_{\rm NS} = 10$ km. The parameters for the supergiant wind are the following: $\dot{M}_{\rm tot} = 10^{-6}$ M$_\odot$ yr^{-1} (Puls et al. 1996), $v_\infty = 1700$ km s^{-1}, $\beta = 1$, $v_0 = 10$ km s^{-1}, and the force multiplier parameters are $k = 0.375$, $\alpha = 0.522$, and $\delta = 0.099$ (Shimada et al. 1994). The corresponding upper and lower limits to the clump radius, derived from Equations (4.21) and (4.26), are shown in Figure 4.3.

4.4.1 The effect of the mass distribution

To study the effects of the clump masses we computed the distributions of the flares luminosity and durations for different values of ζ, f, $M_{\rm a}$ and $M_{\rm b}$, considering for simplicity a circular orbit with $P_{\rm orb} = 10$ d. We first neglected the clump radii distribution assuming that clumps which start from the sonic radius have radii given by Equation (4.21), and follow the expansion law (Equation 4.11). We found that when $M_{\rm a}$ and/or $M_{\rm b}$ increase, the number of clumps produced by the supergiant decreases (see Equation 4.4), resulting in a smaller number of X−ray flares. The average flare luminos-

ity, the average flare duration, the number of flares and the shapes of the luminosity and flare duration distributions do not change much for different values of M_a and M_b. In Figure 4.4 we show the dependence of the distributions of flare luminosities and durations on ζ and f (for $M_a = 10^{19}$ g, $M_b = 10^{22}$ g). If ζ increases, the number of clumps and their density increases (see Equations 4.4 and 4.21), implying a higher number of flares, a shift to higher luminosities and to shorter flare durations.

Figure 4.5 shows the effect of changing the fraction of wind mass in the form of clumps f for different values of ζ. When f increases, the supergiant produces more clumps (see Equations 4.4), thus the number of flares and their average luminosity increase, while their average duration remains unchanged.

4.4.2 The effect of the radii distribution

In Section 4.2 we showed that, for any given mass, the clump dimensions are constrained within the limits given by Equations (4.21) and (4.26). Here we show the effect of different assumptions on the radii distributions laws. We considered both a power law (Equation 4.12) and a truncated normal distribution (Equation 4.13), described by the parameters γ (or N_σ). When γ increases, the number of clumps with larger density decreases, thus the average luminosity of the flares decreases and their average duration increases (see Figure 4.6). We also found that when ζ increases, the flare distributions with a positive γ follow a different behaviour than those with a negative value: for $\gamma < 0$, the flare distributions behave as described above (i.e. the number of flares increases with ζ), while this does not happen for $\gamma > 0$. This is due to the fact that in this case the clumps are larger, thus there is a high probability that two or more clumps overlap thus reducing the number of flares.

For the case of a normal distribution of clump radii, we calculated the distributions of flare luminosities and durations for different values of N_σ (see Figure 4.7). When N_σ increases, the number of clumps with larger and smaller radii is reduced, resulting in a narrower flare luminosity distribution. When ζ increases, the flare distributions have the same behaviour described above for the case $\gamma > 0$.

We then tried another test, increasing the orbital period (e.g. from 10 days to 100 days), finding that the shape of the integral distributions in Figure 4.6 remains similar, except for the number of X−ray flares, which decreases.

4.4.3 The effect of the mass-loss rate

The effects of different wind mass-loss rates $\dot{M}_{tot}$ are shown in Figure 4.8. The mass-loss rate is usually derived observationally from the strength of

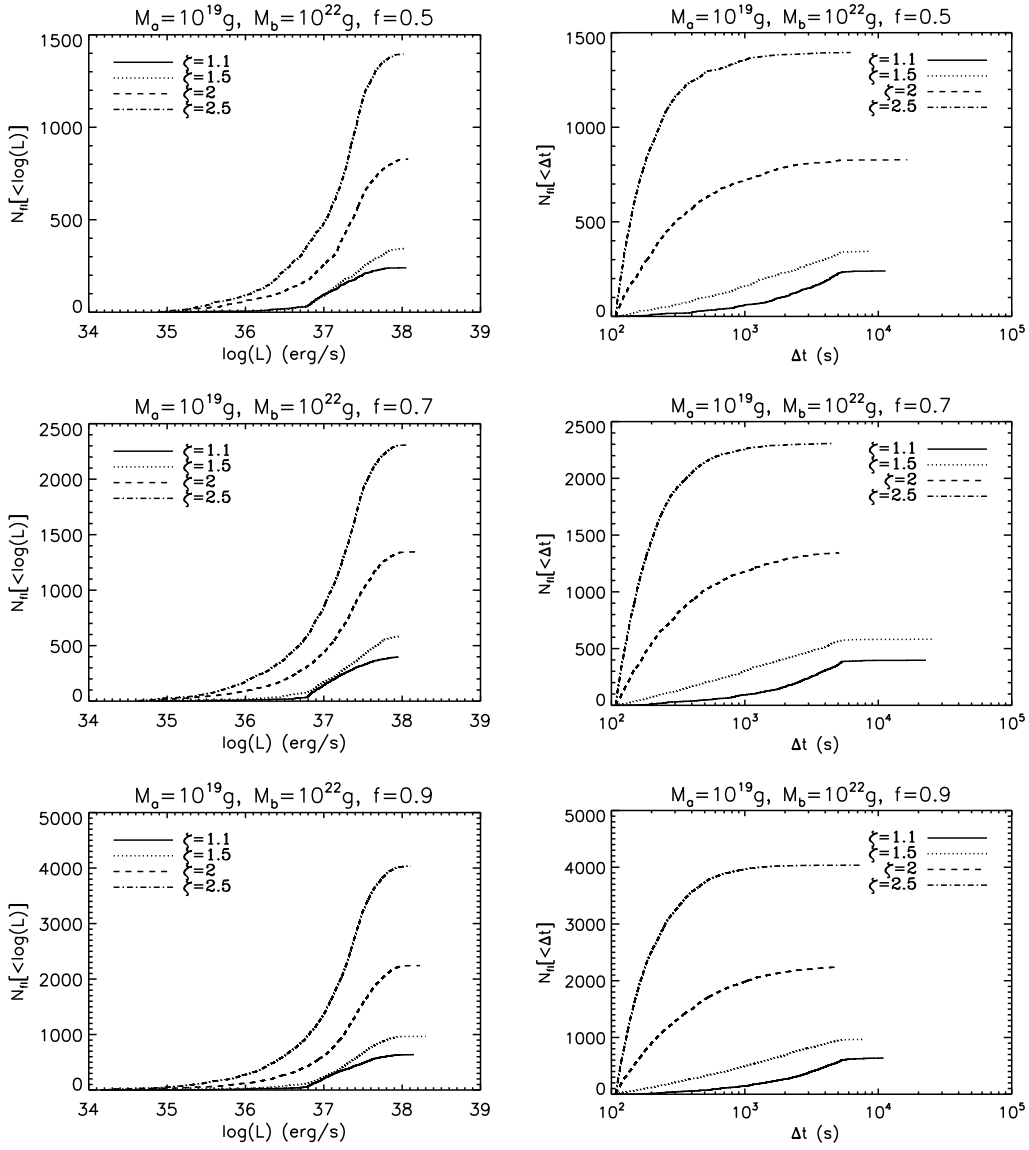

Figure 4.4: Expected integral distributions of the flare luminosities (left panels) and durations (right panels) for different values of ζ and $f = \dot{M}_{\rm cl}/\dot{M}_{\rm tot}$. The binary system parameters are: $M_{\rm OB} = 30$ M$_\odot$, $R_{\rm OB} = 23.8$ R$_\odot$, $M_{\rm NS} = 1.4$ M$_\odot$, $R_{\rm NS} = 10$ km, $P_{\rm orb} = 10$ d, $e = 0$. The parameters for the supergiant wind are: $\dot{M}_{\rm tot} = 10^{-6}$ M$_\odot$ yr^{-1}, $v_\infty = 1700$ km s^{-1}, $\beta = 1$, $v_0 = 10$ km s^{-1}, $M_{\rm a} = 10^{19}$ g and $M_{\rm b} = 10^{22}$ g and $f = 0.5$, 0.7, 0.9. The time interval for each histogram corresponds to 100 days.

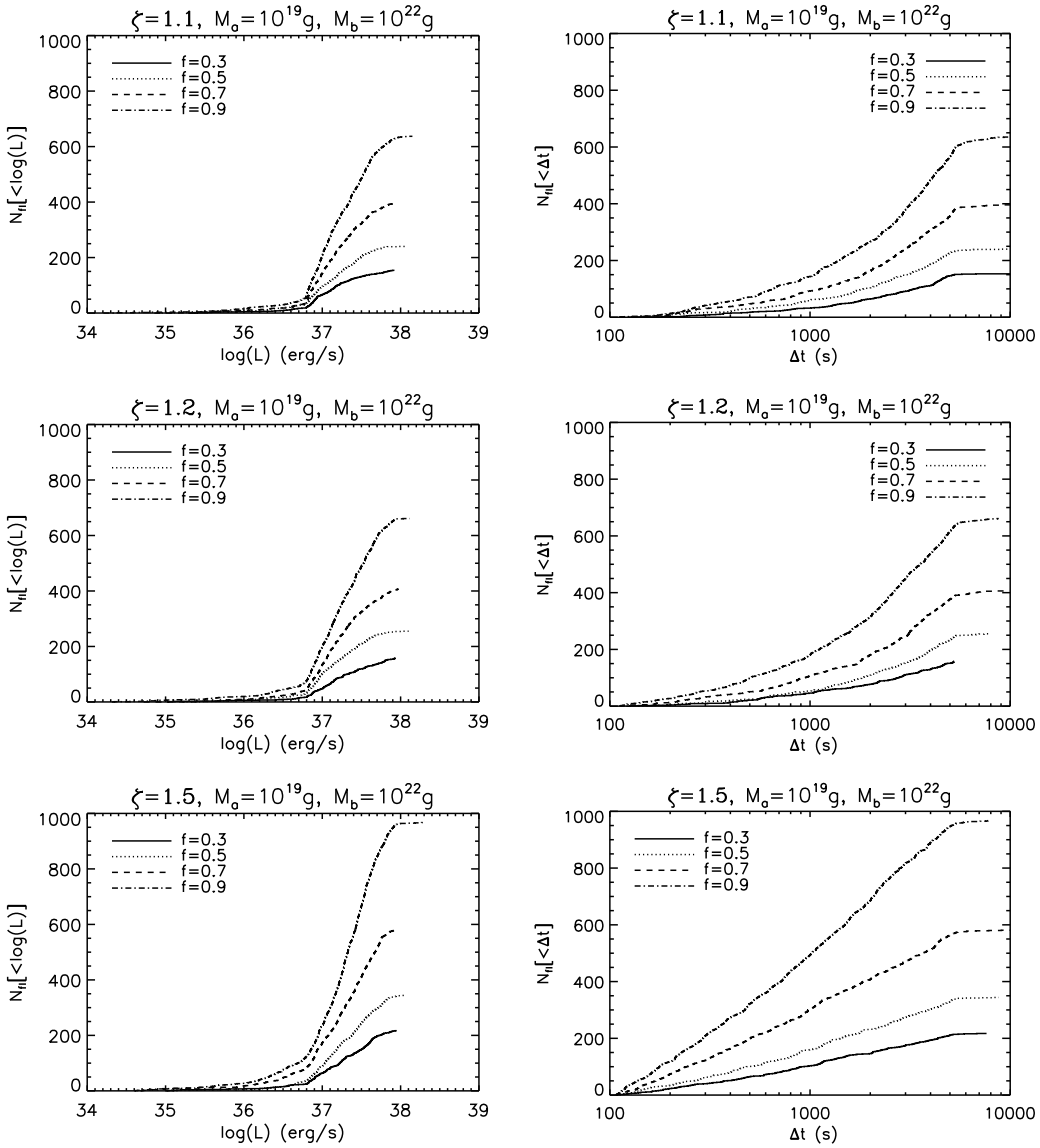

Figure 4.5: Expected integral distributions of the flare luminosities (left panels) and durations (right panels) for different values of $f = \dot{M}_{\rm cl}/\dot{M}_{\rm wind}$ and ζ. The binary system parameters are in the caption of Figure 4.4. The time interval corresponds to 100 days.

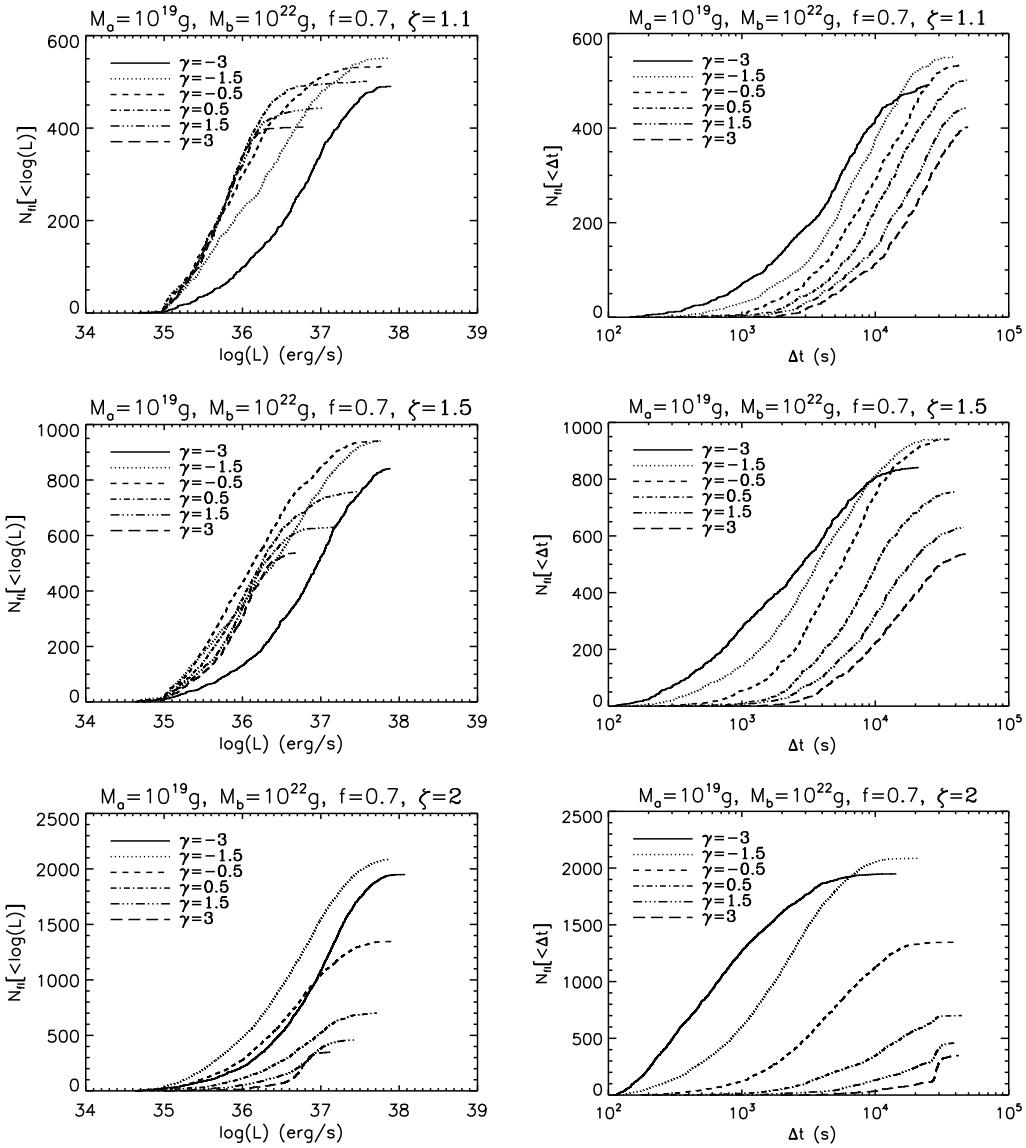

Figure 4.6: Expected integral distributions of the flare luminosities (left panels) and durations (right panels) for different values of γ and ζ of the Equations (4.12) and (4.1). The binary system parameters are in the caption of Figure 4.4. The time interval for each histogram corresponds to 100 days.

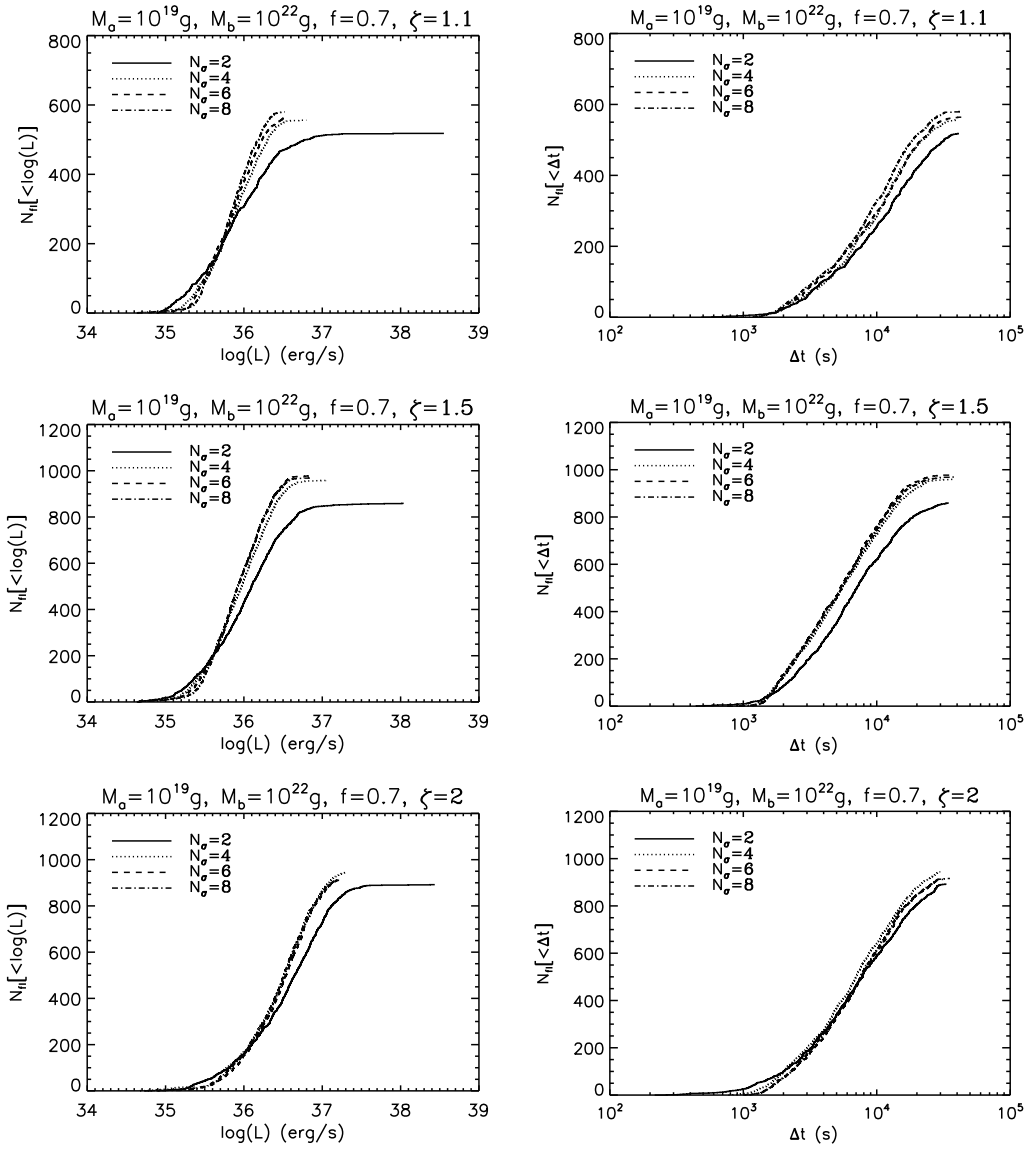

Figure 4.7: Expected integral distributions of the flare luminosities (left panels) and durations (right panels) for different values of N_σ and ζ of the Equations (4.13) and (4.1). The binary system parameters are in the caption of Figure 4.4. The time interval for each histogram corresponds to 100 days.

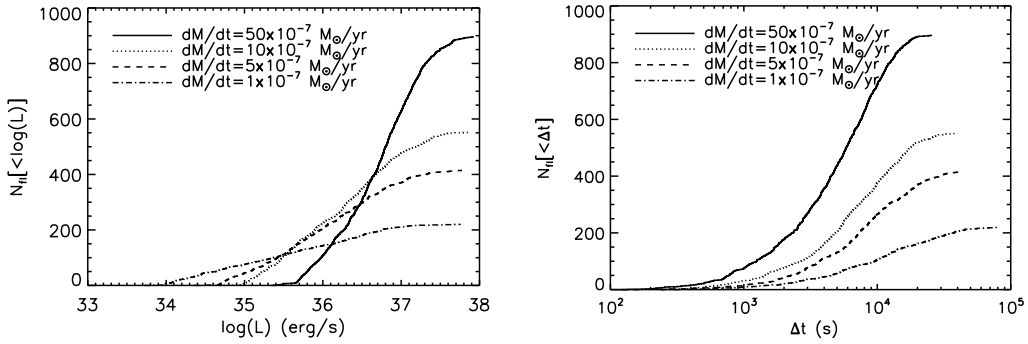

Figure 4.8: Expected integral distributions of the flare luminosities and durations for different values of the mass-loss rate and for an assumed orbital period of 10 days and a circular orbit. $\zeta = 1.1$, $\gamma = -1.5$, $f = 0.7$. The other binary system parameters are in the caption of Figure 4.4. The time interval corresponds to 100 days.

the Hα emission line, since this gives smaller uncertainties than the method based on UV P-Cygni lines (Kudritzki & Puls 2000). Since the Hα line opacity depends on ρ^2, the presence of wind inhomogeneities leads to an overestimate of the mass-loss rate. In particular, the mass-loss rates from O stars derived from smooth-wind models measurements with the Hα method need to be reduced by a factor 3 to 10 if the wind is clumpy (see Lépine & Moffat 2008 and Hamann et al. 2008). In Figure 4.8 we show that if $\dot{M}_{\rm tot}$ decreases, also the number of flares decreases due to the reduced number of clumps. Also the average luminosity of the flares is reduced because the number density of clumps decreases resulting in a smaller probability that two or more clumps overlap.

4.4.4 The effect of the orbital parameters

In Figure 4.9 we show the effect of changing the orbital period $P_{\rm orb}$ and the eccentricity e. We assumed $\zeta = 1.1$, $\gamma = -1.5$, $f = 0.7$. When the orbital period increases, the number of flares emitted by the neutron star decreases (see Equation 4.30) and the neutron star accretes clumps with a smaller density (see Equation 4.11), implying a shift to lower luminosities and higher flare durations (see Figure 4.9). When the eccentricity increases, the neutron star accretes clumps with a higher density range (in general clumps are denser when they are closer to the supergiant), thus the luminosity range of the flares increases, as shown in Figure 4.9.

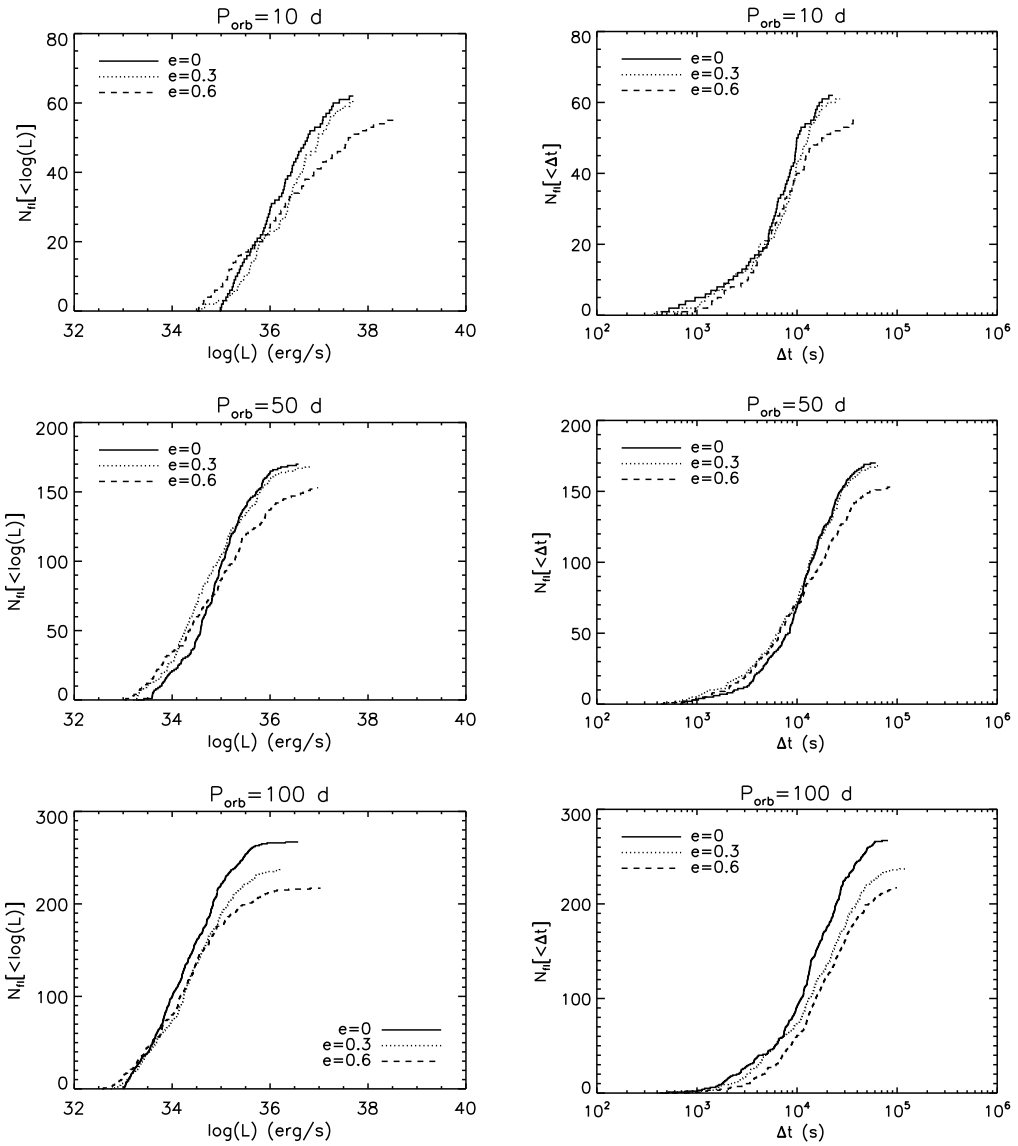

Figure 4.9: Expected integral distributions of the flare luminosities for different orbital periods and eccentrities of the binary system. $\zeta = 1.1$, $\gamma = -1.5$ and $f = 0.7$. The other binary system parameters are in the caption of Figure 4.4. The time interval for each histogram corresponds to the orbital period.

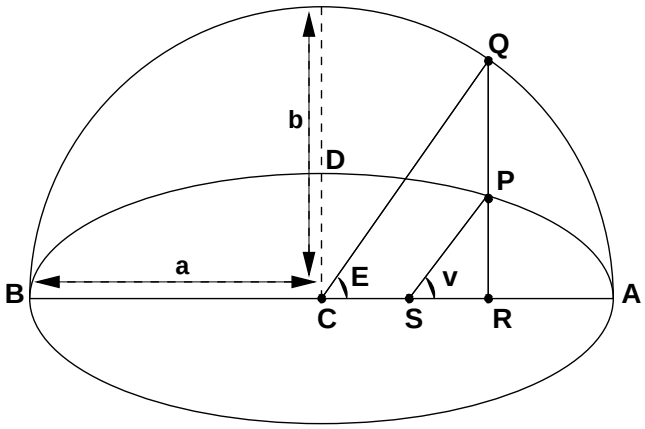

Figure 4.10: P is the position of the neutron star at time t, S is the position of the OB supergiant, A is the position of the periastron and C is the centre of the ellipse and of the auxiliary circle. RP is the perpendicular from P to AB, which intersect the auxiliary circle at Q. The angle $\widehat{QCA}$ is the eccentric anomaly (denoted by E).

4.5 Orbital X-ray variability

The accretion luminosities (Equations 4.32 and 4.33) are computed in each point of the orbit thanks to the eccentric and mean anomaly. The eccentric anomaly E of the orbit is defined as the angle between the periastron, the center of the ellipse of the orbit, and the point located by drawing a line perpendicular to the semi-major axis passing through the neutron star and intersecting the auxiliary circle of the ellipse with the major axis as diameter (see Figure 4.10). The eccentric anomaly E is only an intermediary angle, and can be expressed as a function of time thanks to the mean anomaly M, which is defined as:

$$M = \frac{2\pi}{P_{\rm orb}}(t - t_0) \tag{4.34}$$

where $P_{\rm orb}$ is the orbital period of the neutron star, t is the time and t_0 is the time of the periastron passage. The mean anomaly represents the angle described in a time interval $t - t_0$ by a radius vector rotating around the supergiant with constant angular velocity $2\pi/P_{\rm orb}$. The relation between the eccentric anomaly E and the mean anomaly M is given by the following relation:

$$M = E - e\sin(E)\ . \tag{4.35}$$

Thanks to Equation (4.35), it is possible to obtain the value of E given M (i.e. the time t) and e. However, the Equation (4.35) is trascendental and cannot be solved directly for E given an arbitrary M and e: it is possible to

obtain only an approximation of E. We solved Equation (4.35) iteratively, with the series:

$$E_1 = M + e\sin(M) \quad (4.36)$$
$$E_2 = M + e\sin(E_1) \quad (4.37)$$
$$E_3 = M + e\sin(E_2) \quad (4.38)$$
$$\dots$$
$$E_{n+1} = M + e\sin(E_n) \quad (4.39)$$

which converge to the value $E = M + e\sin(E)$ (Smart 1965).

Thus, the wind velocity, the relative velocity between the wind and the neutron star and the distance r between the supergiant and the neutron star are given by:

$$r = a(1 - e\cos(E)) \quad (4.40)$$
$$v_w = v_\infty \left(1 - \frac{0.9983 R_{OB}}{a(1 - e\cos(E))}\right)^\beta \quad (4.41)$$
$$v_r = \frac{2\pi a e \sin(E)}{P_{orb}(1 - e\cos(E))} \quad (4.42)$$
$$v_\phi = \frac{2\pi a}{P_{orb}(1 - e\cos(E))}\sqrt{1 - e^2} \quad (4.43)$$

where a is the semi-major axis and P_{orb} is the orbital period of the neutron star.

4.6 Comparison with the HMXB Vela X−1

Vela X−1 (4U 1900−40) is a bright eclipsing X-ray binary (P_{orb}= 8.964 d, $e \sim 0.09$) formed by the B0.5 Ib supergiant HD 77581 (Brucato & Kristian 1972) (M = 23 $M_\odot$, R= 30 $R_\odot$, van Kerkwijk et al. 1995) and a pulsar with spin period $\sim$ 283 s and mass 1.9 $M_\odot$. This source shows significant X−ray variability on short time-scales, with flares lasting from $\sim$ 500 s to $\sim$ 40000 s (Haberl 1994; Kreykenbohm et al. 2008).

Recently Kreykenbohm et al. (2008) analyzed *INTEGRAL* observations of Vela X−1 obtained during a phase of high flaring activity, finding two kinds of flares: brief and bright flares softer than longer flares. They also found several off-states, during which the source is not detected (at least by *INTEGRAL*). Kreykenbohm et al. (2008) proposed that the short flares are caused by the flip-flop instability, while the long ones are due to the accretion of clumps ejected by the supergiant. The off-states are explained as due to the onset of the propeller effect when the neutron star crosses the lower density inter-clump medium.

In this section we apply our wind model to Vela X-1, assuming the wind parameters derived by Searle et al. (2008) and reported in Table 4.1.

Table 4.1: Parameters of the HMXBs studied in this work. Values labeled with (*) are taken from Searle et al. (2008), values labeled with (†) are taken from Lefever et al. (2007).

	Vela X−1	4U 1700−377
Type	SGXB	SGXB
Spectral Type	B0.5 Ib	O6.5 Iaf$^+$
$M_{\rm OB}$	23 $M_\odot$	58 $M_\odot$
$R_{\rm OB}$	30 $R_\odot$	21.9 $R_\odot$
$T_{\rm eff}$	2.5×10^4 K (*)	3.5×10^4 K
$\log(L/L_\odot)$	5.58 (*)	5.82
$\dot{M}_{\rm tot}$ ($M_\odot$ yr^{-1})	$0.7 - 1.2 \times 10^{-6}$ (*)	9.5×10^{-6}
v_∞ (km s^{-1})	$\sim 1520 - 1600$ (*)	1700
β	$\sim 1 - 1.5$ (*)	1.3
$M_{\rm NS}$	1.9 $M_\odot$	2.44 $M_\odot$
$P_{\rm orb}$	8.964 d	3.412 d
e	$e \sim 0.09$	0
$P_{\rm spin}$	~ 283 s	–
distance	~ 2.0 kpc	1.9 kpc
	IGR J11215−5952	IGR J18483−0311
Type	SFXT	SFXT
Spectral Type	B0.7 Ia	B0.5Ia
$M_{\rm OB}$	23 $M_\odot$ (*)	33 $M_\odot$ (*)
$R_{\rm OB}$	35.1 $R_\odot$ (*)	33.8 $R_\odot$ (*)
$T_{\rm eff}$	2.36×10^4 K (*)	2.47×10^4 K (*)
$\log(L/L_\odot)$	5.5 (*)	5.58 (*)
$\dot{M}_{\rm tot}$ ($M_\odot$ yr^{-1})	$1 - 2.5 \times 10^{-6}$	$0.4 - 1.5 \times 10^{-6}$
v_∞ (km s^{-1})	$\sim 1000 - 1400$ (*) (†)	$\sim 1400 - 1800$ (*)
β	$\sim 1 - 1.5$	$\sim 1 - 1.5$
$M_{\rm NS}$	1.4 $M_\odot$	1.4 $M_\odot$
$P_{\rm orb}$	164.5 d	18.52 d
e	–	–
$P_{\rm spin}$	186.78 ± 0.3 s	21.05 s
distance	8 kpc	$3 - 4$ kpc

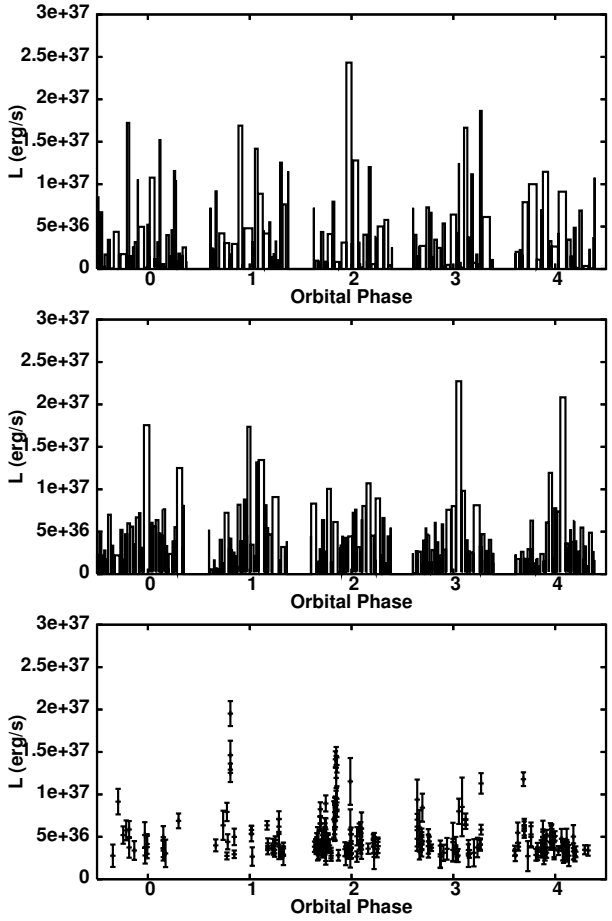

Figure 4.11: Comparison of the Vela X−1 light curve, as observed with ASM/*RXTE* (lower panel), with that calculated with our clumpy wind model for the parameters reported in Table 4.1, and $\dot{M}_{\rm tot} = 2.1 \times 10^{-7}$ M$_\odot$ yr^{-1}, $\beta = 1$, $v_\infty = 1600$ km s^{-1}, $f = \dot{M}_{\rm cl}/\dot{M}_{\rm wind} = 0.75$, $M_{\rm a} = 5 \times 10^{18}$ g, $M_{\rm b} = 5 \times 10^{21}$ g, $\zeta = 1.1$, $N_\sigma = 5$ (middle panel), and $\gamma = -1$ (upper panel), $k = 0.375$, $\alpha = 0.522$, $\delta = 0.099$. Orbital phase $\phi = 0$ corresponds to 53750 MJD. Note that Vela X−1 is not continuously observed with ASM/*RXTE*. Therefore it is possible that some flares have been missed.

In Figure 4.11 we compare the light curve measured with the ASM/*RXTE* instrument with that calculated with our clumpy wind model assuming a spherical symmetry for the outflowing wind. The ASM/*RXTE* count rate, measured in the $2-10$ keV range, has been converted to the $1-100$ keV luminosity using the average spectral parameters obtained by Orlandini et al. (1998) and the distance of 2 kpc (Sadakane et al. 1985). The observed light curve of Vela X−1 is well reproduced by our clumpy wind model for $\dot{M}_{\rm tot} = 2.1 \times 10^{-7}$ M$_\odot$ yr^{-1}, $M_{\rm a} = 5 \times 10^{18}$ g and $M_{\rm b} = 5 \times 10^{21}$ g, $\zeta = 1.1$, $f = 0.75$ and $\gamma = -1$. Acceptable light curves were also obtained with $\gamma = 1$ and $\dot{M}_{\rm tot} = 4 \times 10^{-7}$ M$_\odot$ yr^{-1}, and with a normal distribution law for the clump radii, with $N_\sigma = 5$. We point out that the average luminosity observed by ASM/*RXTE* out of the flares is $\approx 3 - 4 \times 10^{36}$ erg s^{-1}. This luminosity is obtained in our model with the accretion of numerous clumps with low density.

4.7 Comparison with the HMXB 4U 1700−377

4U 1700−377 (Jones et al. 1973) is a 3.412 day eclipsing HMXB composed of a compact object, (a neutron star or a black hole), and the O6.5 Iaf$^+$ star HD 153919, located at a distance of 1.9 kpc (Ankay et al. 2001). Despite extensive searches, no X−ray pulsations have been found in this system. Therefore the X−ray mass function cannot be determined and the system parameters ($M_{\rm OB}$, $R_{\rm OB}$, $M_{\rm x}$) cannot be derived directly. They have been estimated from the radial velocity curve of the supergiant and from the duration of the X−ray eclipse, by making assumptions about possible values of the radius of the O star and the orbital inclination. Several studies indicate that the mass of the compact object is larger than 2 M$_\odot$ (Rubin et al. 1996; Clark et al. 2002). The similarity of the X−ray spectrum to other pulsars suggest that the compact object of 4U 1700−377 is a neutron star (White et al. 1983), but the presence of a low-mass black hole cannot be excluded (Brown et al. 1996). Reynolds et al. (1999) reported the presence of a possible cyclotron feature at $\sim$ 37 keV observed with *BeppoSAX*. If confirmed, this would demonstrate that 4U 1700−377 hosts a neutron star with a magnetic field of about 2.3×10^{12} G.

The X−ray light curve of 4U 1700−377 is characterized by a strong flaring activity with variations as large as a factor of $10-100$ on time scales from minutes to hours (Haberl et al. 1989; White et al. 1983; Rubin et al. 1996). We assumed the most recent set of system parameters of 4U 1700−377, obtained by means of a detailed NLTE (Non-Local Thermal Equilibrium) line-driven wind model analysis of HD 153919 and a Monte Carlo simulation for the determination of the masses of both components (Clark et al. 2002). These authors found that the supergiant has a luminosity $\log(L/L_\odot) = 5.82 \pm 0.07$, an effective temperature $T_{\rm eff} \approx 35000$ K, radius $R_{\rm OB} \approx 21.9$ R$_\odot$,

mass $M_{\rm OB} \approx 58$ M$_\odot$, mass loss rate $\dot{M} = 9.5 \times 10^{-6}$ M$_\odot$ yr^{-1}, and a mass for the compact object $M_{\rm x} = 2.44$ M$_\odot$ (Table 4.1).

The X−ray spectrum of 4U 1700−377 is well described by an absorbed power law with high-energy cutoff (van der Meer et al. 2005). The spectrum above 20 keV was studied using different satellites (e.g. BATSE detector on board the *CGRO*, *INTEGRAL*) and can be modelled using a thermal bremsstrahlung model with $kT \sim 25$ keV (Rubin et al. 1996) or with a thermal Comptonization model (Orr et al. 2004).

The analysis of the $0.5 - 12$ keV spectrum with *XMM-Newton* during the eclipse, the egress, and a low-flux interval led van der Meer et al. (2005) to suggest that the low-flux interval is probably due to a lack of accretion such as expected in a structured and inhomogeneous wind. Moreover, van der Meer et al. (2005) proposed that the fluorescence line from near-neutral iron detected in all spectra is produced by dense clumps. They also observed recombination lines during the eclipse which indicate the presence of ionized zone around the compact object.

We analyzed the public archival *INTEGRAL* data of 4U 1700−377, using all the IBIS/ISGRI observations obtained from 2003 March 12 to 2003 April 22, and from 2004 February 2 to 2004 March 1. These data correspond to a net exposure time of ~ 5.2 days (excluding the eclipse phase). We reduced the data using OSA 7.0, and extracted the light curve in the energy range $15 - 60$ keV, finding a total of 123 flares. For each flare we extracted the spectrum in the range $22 - 100$ keV. All the spectra could be well fit by a thermal Comptonization model (COMPTT in XSPEC). Based on the spectral results, we computed the $1 - 200$ keV luminosity of each flare. All of them have a luminosity greater than 5.8×10^{36} erg s^{-1} (for lower luminosities it is difficult to evaluate the flare duration and then to distinguish the flares from the average level of the X−ray emission). For each flare we have measured two parameters: the peak luminosity and the flare duration. We then applied our clumpy wind model to the *INTEGRAL* observations of 4U 1700−377. We first compared the observed distributions of the flare luminosities and durations with those computed adopting the system parameters reported in Table 4.1. We assumed for the computed distribution a time interval equal to the exposure time of the 4U 1700−377 observations considered here. As shown in Figure 4.12 the flare properties are well reproduced with our clumpy wind model for $\dot{M}_{\rm tot} = 1.3 \times 10^{-6}$ M$_\odot$ yr^{-1}, $M_{\rm a} = 5 \times 10^{16}$ g and $M_{\rm b} = 2 \times 10^{19}$ g, $\zeta = 1.2$, $\gamma = -6.5$ and $f = 0.75$. We found that the numbers of observed (123) and calculated flares (116) are in good agreement. The light curve of 4U 1700−377 calculated with our clumpy wind model is shown in Figure 4.13.

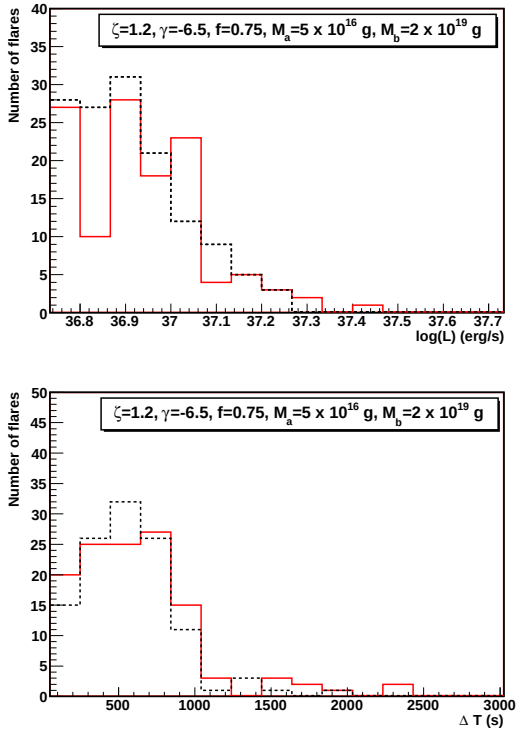

Figure 4.12: Comparison between observed (solid line) and calculated (dashed line) distributions of the flare luminosities and durations for 4U 1700−377. The binary system parameters are: $M_{\rm OB} = 58$ M$_\odot$, $R_{\rm OB} = 21.9$ R$_\odot$, $M_{\rm NS} = 2.44$ M$_\odot$, $R_{\rm NS} = 10$ km. The parameters for the supergiant wind are: $\dot{M}_{\rm tot} = 1.3 \times 10^{-6}$ M$_\odot$ yr^{-1}, $v_\infty = 1700$ km s^{-1}, $\beta = 1.3$, $v_0 = 10$ km s^{-1}, $M_{\rm a} = 5 \times 10^{16}$ g and $M_{\rm b} = 2 \times 10^{19}$ g, $\zeta = 1.2$, $\gamma = -6.5$ and $f = 0.75$.

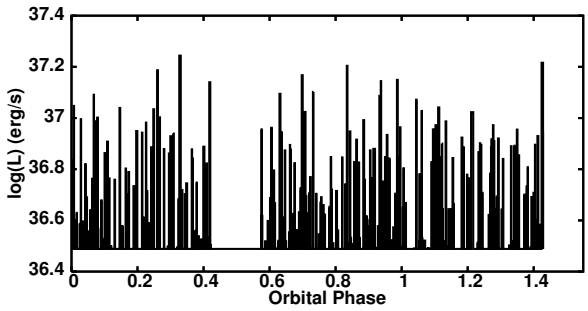

Figure 4.13: Computed light curve of 4U 1700−377. The off-state at orbital phase $0.42 \lesssim \phi \lesssim 0.58$ is due to the eclipse. The stellar parameters are reported in the caption of Figure 4.12.

4.8 Comparison with the SFXT IGR J11215−5952

The SFXT IGR J11215−5952 was discovered in April 2005 with *INTEGRAL* (Lubinski et al. 2005). It is associated with HD 306414, a B0.7 Ia star located at an estimated distance of ~ 8 kpc (Negueruela et al. 2007). *RXTE* observations showed a pulse period $P_{\rm spin} = 186.78 \pm 0.3$ s (Smith et al. 2006a; Swank et al. 2007). This is the first SFXT for which a periodicity in the outbursts recurrence time was discovered (Sidoli et al. 2006). Subsequent observations (Romano et al. 2009c) showed that the true periodicity is about 164.5 days, i.e. half of the originally proposed value. This periodicity is very likely due to the orbital period of the system.

For a distance of 8 kpc the peak fluxes of the outbursts correspond to a luminosity of $\sim 5 \times 10^{36}$ erg s^{-1} ($5 - 100$ keV, Romano et al. 2007). *Swift* monitoring of this source revealed that the outburst (lasting a few days) is composed by many flares (lasting from minutes to a few hours), and before and after the whole outburst the source is fainter than 10^{33} erg s^{-1} (Sidoli et al. 2007).

Sidoli et al. (2007) showed that accretion from a spherically symmetric homogeneous wind could not reproduce the observed light curve and therefore proposed a model based on an anisotropic wind characterized by a denser and slower equatorial component, periodically crossed by the neutron star along its orbit. However this result was based on the old determination of the orbital period (329 days). Therefore, before applying our clumpy wind model, we checked the spherically symmetric homogeneous wind with $P_{\rm orb} = 164.5$ d, different eccentricity values, and the set of stellar parameters derived by Searle et al. (2008) and Lefever et al. (2007) and reported in Table 4.1. We assumed a terminal velocity v_∞ ranging from 1000 km s^{-1} to 1400 km s^{-1}, and $\dot{M}$ ranging from 1×10^{-6} M$_\odot$ yr^{-1} to 2.5×10^{-6} M$_\odot$ yr^{-1}. In all cases we found that the duration of the X−ray outburst observed with *Swift* is shorter than that of the calculated light curves.

A better agreement with the observations could be obtained with our clumpy wind model, especially for what concerns the flaring variability during the outburst phase. However, also in this case the calculated light curve always produces an outburst longer than the observed one. This is shown in Fig. 4.14, where the green symbols correspond to the accretion of a dense clump (producing a flare), while the blue symbols indicate the lower luminosity level produced by the accretion of the inter-clump matter. We found that the probability to observe a flare, rather than the inter-clump luminosity level, is 90%.

In order to improve the agreement between the observed and the calculated light curve, we introduced an anisotropic outflow similar to that proposed by Sidoli et al. (2007). In this modified model we introduce a denser clumpy wind component in the equatorial plane, with a thickness $2h$, a terminal velocity $v_{\rm ed}$ and a mass loss rate $\dot{M}_{\rm ed}$, together with a spherically

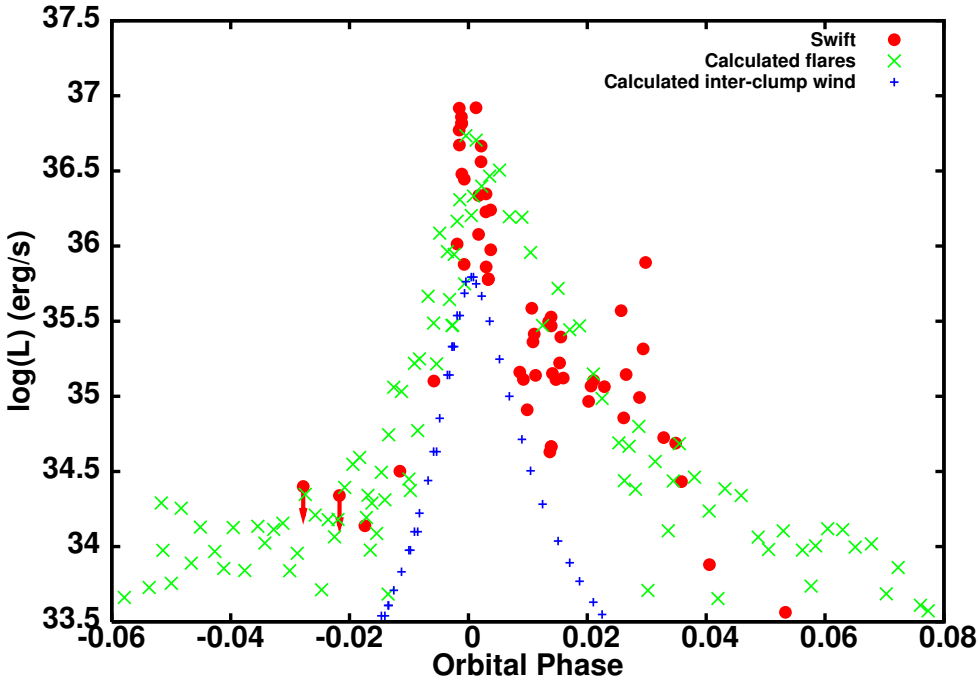

Figure 4.14: Comparison of the IGR J11215−5952 light curve of the February 2007 outburst observed with *Swift*/XRT with the calculated X−ray light curve of our clumpy wind model (presented in Section 4.2) with the stellar parameters reported in Table 4.1, and $P_{\rm orb} = 164.5$ d, $e = 0.89$, $\dot{M}_{\rm tot} = 2 \times 10^{-7}$ M$_\odot$ yr^{-1}, $\beta = 1$, $v_\infty = 1400$ km s^{-1}, $f = \dot{M}_{\rm cl}/\dot{M}_{\rm wind} = 0.75$, $M_{\rm a} = 10^{17}$ g, $M_{\rm b} = 10^{20}$ g, $\zeta = 1.1$, $\gamma = 6$, $k = 0.709$, $\alpha = 0.470$, $\delta = 0.089$.

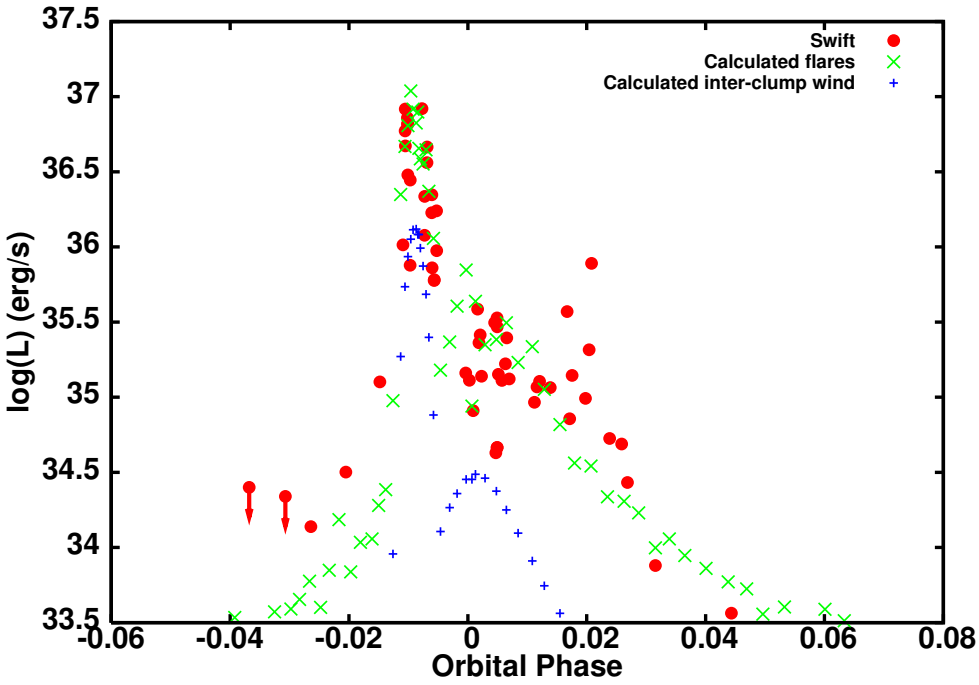

Figure 4.15: Comparison of the IGR J11215−5952 light curve of the February 2007 outburst observed with *Swift*/XRT with the calculated X−ray light curve of our clumpy wind model with equatorially enhanced wind component (presented in Section 4.2). We used the stellar parameters reported in Table 4.2.

symmetric clumpy wind component (polar wind) with terminal velocity $v_{\rm pw}$ and a mass loss rate $\dot{M}_{\rm pw}$. We linked the mass loss rate from the equatorial outflow with the mass loss rate from the polar wind, by means of the factor $f_{\rm ed}$:

$$\dot{M}_{\rm ed} = f_{\rm ed}\dot{M}_{\rm pw} \ . \tag{4.44}$$

Both wind components are clumpy and obey laws described in Section 4.2. We assume that the second wind component has a Gaussian density profile perpendicular to the equatorial plane of the supergiant. In this framework we have considered an orbital period $P_{\rm orb} = 164.5$ d and a high eccentricity in order to produce only one outburst per orbit. The comparison between the *Swift* light curve and that predicted with this model is shown in Figure 4.15. A good agreement with the data is obtained with the parameters reported in Table 4.2.

Table 4.2: Parameters for the calculated X−ray light curves of IGR J11215−5952 of our clumpy wind model with equatorially enhanced wind component (see Figure 4.15). i_0 is the angle of inclination of the orbital plane with respect the equatorial wind component; i_p is the angle between the orbital plane intersection with the equatorial wind component and the direction of the periastron.

Parameter	Value
β	1
$\dot{M}_{\rm pw}$	1×10^{-7} M$_\odot$ yr^{-1}
$v_{\infty,\ pw}$	1500 km s^{-1}
i_0	20°
i_p	70°
$h_{\rm ed}$	$2. \times 10^{11}$ cm
$f = \dot{M}_{\rm cl}/\dot{M}_{\rm wind}$	0.75
$M_{\rm a}$	5×10^{18} g
$M_{\rm b}$	10^{20} g
ζ	1.1
γ	6
$f_{\rm ed}$	100
$v_{\infty,\ ed}$	1000 km s^{-1}

4.9 Comparison with the SFXT IGR J18483−0311

IGR J18483−0311 is a SFXT discovered by the *INTEGRAL* satellite in 2003 (Chernyakova et al. 2003). This source is composed by a B0.5Ia star located at 3-4 kpc (Rahoui et al. 2008) and a pulsar, with a spin period of ~ 21 s (Sguera et al. 2007), orbiting around the companion star in ~ 18.55 d (Levine & Corbet 2006).

The broad band joint *INTEGRAL* spectrum (JEM-X + IBIS/ISGRI, 3-50 keV) of this source during the outbursts was fitted with an absorbed power law with photon index $\Gamma = 1.4 \pm 0.3$, with a cutoff at $E_{\rm c} = 22^{+7.5}_{-4.5}$ keV and high absorption ($N_{\rm H} = 9^{+5}_{-4} \times 10^{22}$ cm^{-2}; Sguera et al. 2007). IGR J18483−0311 has been detected by *XMM-Newton*, *INTEGRAL*, and *Swift* with a luminosity in the range $10^{33} - 10^{34}$ erg s^{-1} and spectral shape similar to that during the outburst activity (Romano et al. 2010; Sguera et al. 2010; Giunta et al. 2009).

We applied our clumpy wind model to the X-ray lightcurve of IGR J18483−0311, obtained by Romano et al. (2010) from the monitoring of this source performed in 2009 with *Swift*/XRT, and covering more than one orbital period.

The modulation of the overall shape of the light curve with the orbital phase emerging from the *Swift*/XRT observations (Romano et al. 2010) can be interpreted as wind accretion along a highly eccentric orbit. Thus, we applied different models for the wind accretion to gain information on the

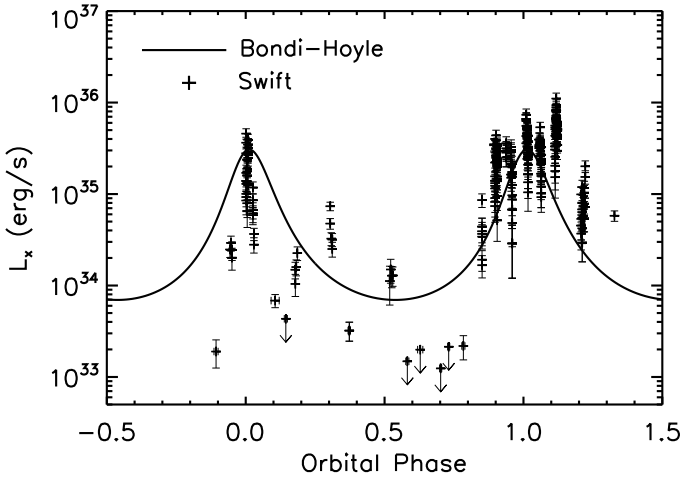

Figure 4.16: Comparison of the *Swift*/XRT light curve of IGR J18483−0311 (crosses) with the prediction of Bondi-Hoyle accretion from a spherically symmetric and homogeneous wind. We assumed a distance of 3 kpc. The model-dependent orbital phase $\phi = 0$ corresponds to 54995.83 MJD.

source parameters.

The simplest case is a Bondi-Hoyle accretion from a spherically symmetric and homogeneous wind. Assuming a supergiant mass of $M_{\rm OB} = 33$ M$_\odot$ and a radius $R_{\rm OB} = 33.8$ R$_\odot$ (Searle et al. 2008), a neutron star mass of $M_{\rm NS} = 1.4$ M$_\odot$ and a radius $R_{\rm NS} = 10^6$ cm, together with the known orbital period of $P_{\rm orb} = 18.52$ d, we tried to account for the overall shape of the X−ray light curve, leaving the orbital eccentricity e as a free parameter. We assumed the following values for the wind properties: a terminal velocity v_∞ in the range $1400 - 1800$ km s^{-1}, a mass loss rate $\dot{M}$ in the range $0.4 - 1.5 \times 10^{-6}$ M$_\odot$ yr^{-1} (see Searle et al. 2008; Lefever et al. 2007). In this framework, we obtain the best agreement with the observed light curve by assuming an eccentricity $e = 0.4$, $v_\infty = 1800$ km s^{-1}, $\dot{M} = 5 \times 10^{-7}$ M$_\odot$ yr^{-1}, $\beta = 1$. Figure 4.16 shows the comparison of the model predictions and the observed *Swift*/XRT lightcurve (by assuming a distance of 3 kpc). The model roughly reproduces the shape of the X−ray lightcurve due to the orbital modulation, with the largest deviation from the observations being in the time interval MJD 55006.5−55010.2, where we observed 4 upper limits. Note, however, that we cannot be sure that the low intensity extends for 4 days continuously, because the four *Swift* observations consist of short snapshots.

The informations about the X-ray luminosities at apastron and periastron of IGR J18483−0311 can be used within the framework of accretion from a spherically symmetric stellar wind to obtain an alternative and in-

dependent estimation of the magnetic field. In fact, the material in the background wind will be accreted onto the neutron star only if the magnetospheric radius $R_{\rm m}$ is less than the corotation radius $R_{\rm c}$ ($R_{\rm c} > R_{\rm m}$), otherwise centrifugal forces will expel the matter. We are aware that the above assumed model and propeller effect are based on various and stronlgy simplified assumptions, however this is still a reasonable approach to obtain a rough and reliable estimate for the magnetic field strength and the eccentricity. Assuming the spin period measured for IGR J18483−0311 ($P = 21.05$ s), we get a corotation radius $R_{\rm c} = 1.27 \times 10^9$ cm.

The observed quiescent X-ray luminosities could be produced only if the background wind material can reach the surface of the neutron star and impact onto it. However, the requirement of $R_{\rm c} > R_{\rm m}$ imposes important constraints.

We calculated the Bondi-Hoyle X-ray luminosity at orbital phases $\phi = 0$ and $\phi = 0.52$ assuming a supergiant mass $M_{\rm OB} = 33$ M$_\odot$ and a radius $R_{\rm OB} = 33.8$ R$_\odot$ (Searle et al. 2008), and $M_{\rm NS} = 1.4$ M$_\odot$, $R_{\rm NS} = 10$ km for the neutron star. Then we assumed the typical wind parameters for a star with same spectral type of the IGR J18483−0311 supergiant: a mass loss rate $\dot{M}$ in the range $0.4 - 3 \times 10^{-6}$ M$_\odot$ yr^{-1}, $v_\infty = 1200 - 1900$ km s^{-1}, $\beta = 0.8{-}1.6$ and we leave the magnetic field (B) and the orbital eccentricity (e) as free parameters. We calculated the expected X-ray luminosity of the neutron star at periastron and at the orbital phase $\phi \sim 0.52$, assuming that the X-ray emission is due to accretion of matter from the spherically symmetric stellar wind emitted by the supergiant companion. From Equations (1.2), (1.14), (1.15), (1.16), (1.17) we computed the X-ray luminosity $L_{\rm x}$ of a neutron star:

$$L_{\rm x,wind} = \frac{GM_{\rm NS}}{R_{\rm NS}} \dot{M}_{\rm acc} = \frac{(GM_{\rm NS})^3}{R_{\rm NS}} \frac{4\pi\rho_{\rm w}(r)}{[(v_{\rm rel}^2(r) + c_{\rm s}^2]^{3/2}} \qquad (4.45)$$

where G is the gravitational constant. Figure 4.17 shows the allowed range of parameters (e and B) which reproduce the X-ray luminosity at the periastron ($\phi \sim 0$) and apastron ($\phi \sim 0.52$) calculated according to Equation (4.45). The allowed range of parameters (e and B) are $B \lesssim 6 \times 10^{11}$ G and $0.39 \lesssim e \lesssim 0.62$. We note that the above estimated magnetic field is in very good agreement with the value inferred by Sguera et al. (2010) from the putative electron cyclotron line at ∼3.3 keV ($\sim 3 - 4{\times}10^{11}$ G).

An alternative scenario to explain the low intensity state is an X−ray eclipse of the neutron star by the supergiant companion. Assuming a circular orbit, we obtain a lower limit to the radius of the supergiant star (Rappaport & Joss 1983) of $R_{\rm OB} = 46\ R_\odot$, which is too large for a B0.5a supergiant (Searle et al. 2008). On the other hand, our modelling of the X−ray curve suggests a high eccentricity of at least $e = 0.4$. Adopting this eccentricity, we derived an expected value for the supergiant radius of $R_{\rm OB} = 39.5\ R_\odot$. The radii of B0.5Ia stars are usually smaller than this

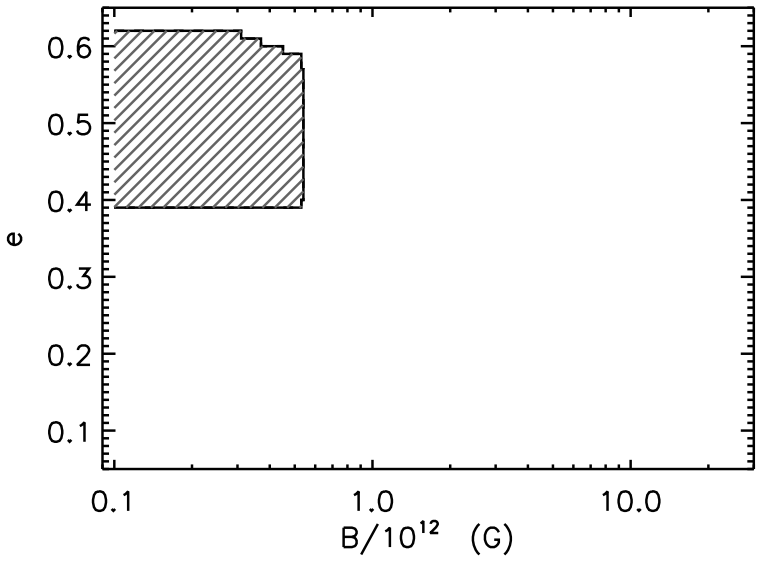

Figure 4.17: Filled region corresponds to the allowed values for the magnetic field and the orbital eccentricity of the neutron star of IGR J18483−0311.

value, but there are several exceptions with $R \approx 40\ R_\odot$ (Searle et al. 2008; Lefever et al. 2007). Therefore we cannot exclude that an eclipse is responsible for the low luminosity state, in an eccentric orbit.

Although both centrifugal inhibition and an eclipse can reconcile the observed low intensity state with the Bondi-Hoyle accretion predictions, it is also clear that the spherically symmetric and homogeneous wind only reproduces the overall shape of the X−ray light curve. It cannot, indeed, account for the very large spread around the average behaviour due to the orbital modulation and, most of all, the remakable short time scale variability. The observed short time scale variability can be naturally explained by the accretion of single clumps composing the donor wind. Thus, in order to improve the agreement between the observed and the calculated light curve, we applied our clumpy wind model.

We sought the set of wind parameters yielding the best agreement between the calculated and the observed light curve. We found that the observed lightcurve is well reproduced by this wind model by assuming the following parameter values: an eccentricity $e = 0.4$, a mass loss rate $\dot{M}_{\rm tot} = 2 \times 10^{-7}$ M$_\odot$ yr^{-1}, $v_\infty = 1800$ km s^{-1}, $\beta = 1$, a fraction of mass lost in clumps $f = 0.75$, a mass distribution power law index $\zeta = 1.1$, a power law index of the initial clump dimension distribution $\gamma = -1$, a minimum clump mass $M_{\rm a} = 10^{18}$ g and a maximum clump mass $M_{\rm b} = 5 \times 10^{21}$ g; moreover, we adopt the force multiplier parameter obtained by Shimada et al. (1994) for a B0.5Ia star ($k = 0.375$, $\alpha = 0.522$, $\delta = 0.099$). Figure 4.18 shows

the comparison of the *Swift*/XRT light curve of IGR J18483−0311 with the isotropic clumpy wind model prediction. Further acceptable solutions can be found by assuming wind parameters ζ, f, γ in the allowed ranges plotted in Figure 4.19, and $e = 0.4 \pm 0.1$, $\dot{M}_{\rm tot} = (2 \pm 1) \times 10^{-7}$ M$_\odot$ yr^{-1}, $v_\infty = 1800$ km s^{-1}, $\beta = 1$, $10^{18} \leq M_{cl} \leq 10^{21}$ g. As Figure 4.19 demonstrates, the comparison of the observed light curve with the clumpy wind model allowed us to constrain the parameters responsible for the degree of inhomogeneity of the wind. In particular, we found that a very large fraction of the mass lost from the supergiant is contained in the clumps ($0.7 \lesssim f \lesssim 0.78$), and we obtain the value of ζ (which controls the shape of the clump formation rate distribution) with an accuracy of ∼15%.

Figure 4.18 shows that the peak luminosities, the dynamic range involved by the flares, the orbital modulation, and the low luminosity state (MJD 55006.5−55010.2) observed are well reproduced by the clumpy wind model, even without invoking either a centrifugal barrier or an X−ray eclipse. Indeed, from the calculated lightcurve, we determined that the probability to observe the source at the inter-clump luminosity level in the range of phase $0.2 < \phi < 0.8$ is $\sim 25\%$: with the binomial distribution function, we obtain a probability to measure 4 low luminosity states of $\sim 5\%$. Therefore, the upper limits can be explained with the accretion of the intra-clump wind with a low density, even without invoking centrifugal inhibition or an eclipse. Finally, we note that the wind parameters we obtain applying our spherical clumpy wind model are very similar to those explaining the Vela X−1 X−ray light curve. Indeed, the two systems have very similar donor stars.

4.10 Other applications of the clumpy wind model

In the framework of the clumpy wind model developed in Section 4.2, it is possible to derive the distance of the neutron star from the supergiant companion, given the durations $\Delta t_{\rm fl}$ and luminosities $L_{\rm fl}$ of the flares observed and adopting the expansion law for the clump size (Equation 4.11).

We explain the general method adopted to obtain this distances for some SFXTs.

If the spectral type of the supergiant is known, it is possible to assume for the supergiant a wind velocity $v_{\rm w}$, a radius $R_{\rm OB}$, a mass $M_{\rm OB}$, a luminosity $\log L/L_\odot$ and an effective temperature $T_{\rm eff}$ (e.g. adopting the parameters of Vacca et al. 1996).

Then, from the duration of the flares, $\Delta t_{\rm fl}$, we obtain the radius of the clumps accreted by the neutron star:

$$R_{\rm cl} = \frac{v_{\rm w} \Delta t_{\rm fl}}{2} \ . \tag{4.46}$$

Hence, from the formula of the X-ray luminosity $L_{\rm fl} \simeq \frac{GM_{\rm NS}}{R_{\rm NS}} \dot{M}_{\rm acc}$, and

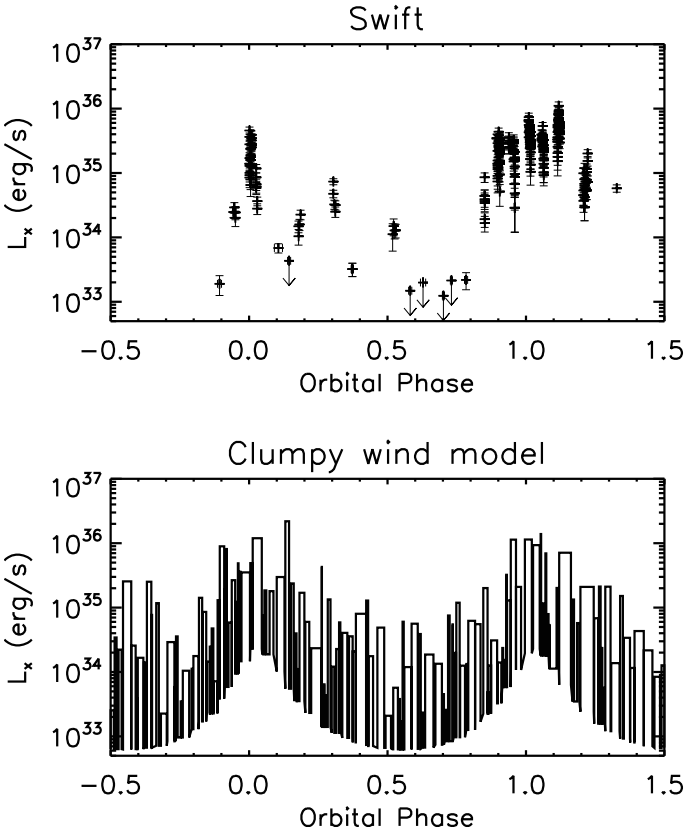

Figure 4.18: Comparison of the *Swift*/XRT light curve of IGR J18483−0311 (top) with the prediction (bottom) of our clumpy wind model. The model-dependent orbital phase $\phi = 0$ corresponds to 54995.83 MJD.

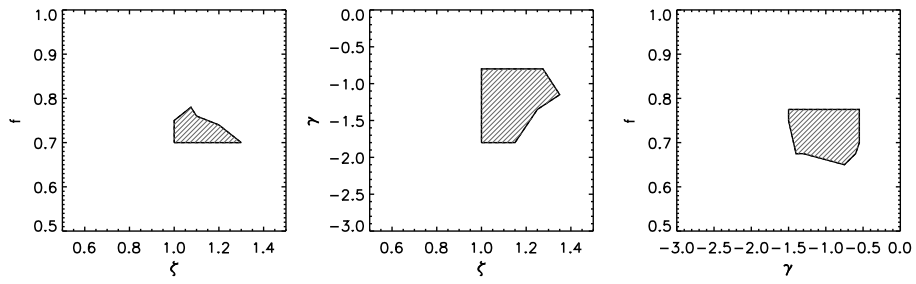

Figure 4.19: Graphs of the allowed parameters ζ, f, γ (filled region), obtained from the comparison between the observed and the calculated light curves.

Table 4.3: Distances r of the compact object from the supergiant donor derived for three SFXTs. *a*: Sidoli et al. (2010); *b*: Romano et al. (2009a); *c*: Sidoli et al. (2009).

SFXT	Observation	Satellite	$M_{\rm OB}$ ($M_\odot$)	$R_{\rm OB}$ ($R_\odot$)	r (cm)
IGR J08408-4503	Dec. 2009 [a]	*Suzaku*	30	24	10^{13}
IGR J08408-4503	Oct. 2006 [b]	*Swift*	30	24	10^{13}
XTE J1739-302	Aug 2008 [c]	*Swift*	33	23	$0.7 - 1.3 \times 10^{13}$
IGR J17544-2619	Sept 2008 [c]	*Swift*	33	23	6.8×10^{12}

the continuity equation $\dot{M}_{\rm acc} = \rho v_{\rm w} \pi R_{\rm acc}^2$, we obtain the clump density:

$$\rho = \frac{L_{\rm fl} R_{\rm NS}}{G M_{\rm NS}} \frac{1}{v_{\rm w} \pi R_{\rm acc}^2} \tag{4.47}$$

and, assuming a spherical shape for the clump, from Equations (4.46) and (4.47) we obtain the clump mass:

$$M_{\rm cl} = \frac{4}{3} \pi R_{\rm cl}^3 \rho \ .$$

Now it is possible to obtain, from the Equation (4.21), the starting radius of the clump $R_{\rm cl,i}$. Then, assuming that the sonic radius $R_{\rm s}$ equals the radius of the supergiant, and that the starting wind velocity at $R_{\rm s}$ is $v_{\rm w}(R_{\rm s}) \simeq 3 \times 10^6$ cm s^{-1} (Bouret et al. 2005), we obtain, from the expansion law of the clump (Equation 4.11) the distance of the neutron star from the companion star. In Table 4.3 are reported the distances we obtained for some SFXTs with this method.

Assuming a circular orbit, the orbital separation obtained for XTE J1739-302 (reported in Table 4.3) translate into an orbital period ranging from 20 to 50 days, consistent with the orbital period of 51.47 d found by Drave et al. (2010). The orbital separation obtained for IGR J17544-2619 is not in agreement with that derived from the orbital period of the source ($r_{4.926\,\rm d} \approx 2.8 \times 10^{12}$ cm). This discrepancy could be due to the X-ray photoionization, which in binary systems with narrow orbits (such as IGR J17544-2619) can change significantly the supergiant wind and therefore the accretion onto the compact object (see Chapter 5).

4.11 Discussion and Conclusions

We have developed a clumpy wind model (where the dynamical problem is not treated) and explored the resulting effects on an accreting compact object in order to explain the observed behavior of the SFXTs and the

SGXBs. Compared to previous attempts to explain the SFXTs outbursts in the context of clumpy winds (Walter & Zurita Heras 2007; Negueruela et al. 2008), we introduced for the first time a distribution for the masses and initial dimensions of the clumps. We described the subsequent expansion of the clumps (Equation 4.11) taking into account realistic upper and lower limits for their radius (Equations 4.21 and 4.26).

This model, together with the theory of wind accretion modified because of the presence of clumps, allow us a comparison with the observed properties of both the light curves and luminosity distributions of the flares in SGXBs and SFXTs.

From the calculated integral distributions (Section 4.4), we found that the observable characteristics of the flares, such as luminosity, duration, number of flares produced, depend mainly on the orbital period (Figure 4.9), the scaling parameter ζ of the power-law distribution for the clump formation rate (Equation 4.1), and the fraction of wind mass in the form of clumps ($f = \dot{M}_{\rm cl}/\dot{M}_{\rm tot}$), as shown in Figures 4.4 and 4.5. Thus the variability properties of the different systems do not depend only on the orbital parameters, but are also significantly affected by the properties of the clumps (in particular by the parameters ζ, γ, f, $M_{\rm a}$, $M_{\rm b}$).

We successfully applied our clumpy wind model to four different high mass X-ray binaries: Vela X−1, 4U 1700−377, IGR J18483−0311, and IGR J11215−5952. For the latter source, however, we had to introduce a denser equatorial component (still with a clumpy structure) in order to reproduce the flare duration (as originally proposed by Sidoli et al. 2007).

In Figure 4.20 we show an example of a light curve of a generic SFXT calculated in the case of anisotropic clumpy wind. We assume for the generic SFXT properties similar to IGR J11215−5952, with an orbital period of 80 d and an eccentricity $e = 0.75$. The orbital plane intersects the equatorial wind component at two phases ($\phi_1 \approx -0.12$, $\phi_2 \approx 0.12$) producing two outbursts. The third outburst is produced at the periastron passage ($\phi_3 \approx 0$). This implies that, if this explanation is correct, up to 3 outbursts per orbit are possible[2].

In Table 4.4 we have summarized the wind parameters obtained for the four sources. This table shows the typical differences in the mass-loss rate and terminal velocity expected from the CAK theory, similar values for ζ and f, and different values for γ, $M_{\rm a}$, $M_{\rm b}$. Moreover, we found that the values of $\dot{M}_{\rm tot}$ that best reproduce the observed light curves of the four HMXBs studied, are in agreement with the hypothesis that the mass-loss rate derived by the Hα emission is overestimated by a factor 2−10, in agreement with recent studies (see Section 4.4.3). We can exclude that the observed light curves of the four HMXBs studied can be reproduced with the same set of

[2]Recently, Drave et al. (2010) interpreted the shape of the lightcurve of the SFXT XTE J1739-302 using this general X-ray binary system model (see Section 2.1.2).

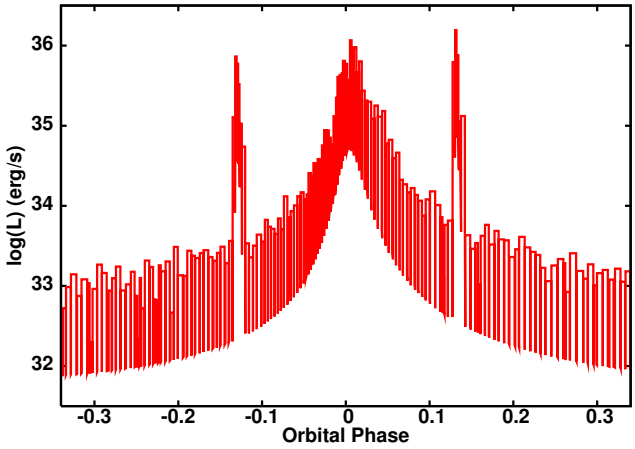

Figure 4.20: Calculated light curve of a SFXT with a neutron star accreting an anisotropic clumpy wind. The parameters of the system are: $M_{\rm NS} = 1.4$ M$_\odot$, $M_{\rm OB} = 23$ M$_\odot$, $R_{\rm OB} = 35.1$ R$_\odot$, $L_{\rm OB} = 3.16 \times 10^5$ L$_\odot$, $P_{\rm orb} = 80$ d, $e = 0.75$, $\dot{M}_{\rm tot} = 2 \times 10^{-7}$ M$_\odot$ yr^{-1}, $v_{\infty,pw} = 1500$ km s^{-1}, $\beta = 1$, $i_0 = 15°$, $i_p = 0°$, $h = 2. \times 10^{11}$ cm, $v_{\infty,ed} = 1000$ km s^{-1}, $f_{\rm ed} = 50$, $T_{\rm eff} = 20000$ K, $k = 0.709$, $\alpha = 0.470$, $\delta = 0.089$, $\zeta = 1.1$, $\gamma = 6$, $M_{\rm a} = 5 \times 10^{18}$ g, $M_{\rm b} = 10^{20}$ g.

Table 4.4: Summary of HMXBs studied in this work. We give in table their name, their type (SGXB or SFXT) their spectral type, the nature of the compact object and their wind parameters that we have assumed. For IGR J11215−5952 is reported the terminal velocity in the polar wind region.

Source	Type	Supergiant	Compact Object	$\dot{M}_{\rm tot}$ (M$_\odot$ yr^{-1})	v_∞ km s^{-1}
Vela X−1	SGXB	B0.5 Ib	NS	2.1×10^{-7}	1600
4U 1700−377	SGXB	O6.5 Iaf$^+$	NS?	1.3×10^{-6}	1700
IGR J11215−5952	SFXT	B0.7 Ia	NS	1×10^{-7}	1500
IGR J18483−0311	SFXT	B0.5Ia	NS	2×10^{-7}	1800

Source	ζ	γ	f	$M_{\rm a}$ (g)	$M_{\rm b}$ (g)
Vela X−1	1.1	−1	0.75	5×10^{18}	5×10^{21}
4U 1700−377	1.2	−6.5	0.75	5×10^{16}	2×10^{19}
IGR J11215−5952	1.1	6	0.75	5×10^{18}	10^{20}
IGR J18483−0311	1.1	−1	0.75	10^{18}	5×10^{21}

wind parameters.

In conclusion, the different values of γ, $M_{\rm a}$, $M_{\rm b}$ obtained for the four HMXBs studied reveal that, in the framework of our clumpy wind model, the properties of the clumps of these X−ray binary systems are slightly different, independently of the orbital period. This discrepancy could be due to the different spectral type of the four supergiants, which could eject structurally inhomogeneous winds with slightly different properties. We suggest as a possible cause of this behaviour that the values of γ, $M_{\rm a}$, $M_{\rm b}$ could be related to the sonic radius where the clumps start (Bouret et al. 2005), which depends on the supergiant properties (Equation 4.10).

Chapter 5

INTEGRAL results on Supergiant Fast X−ray Transients

In this Chapter we report the results from the analysis of *INTEGRAL* data of 14 SFXTs, for a total exposure time of $\sim$ 30 Ms. The results obtained here are discussed considering the structure of the clumpy supergiant winds (Ducci et al. 2009), the effect of X−ray photoionization of the outflowing wind by the compact object (in the framework of the Ho & Arons 1987 accretion model), and the possible formation of transient accretion disks, as those proposed by Taam, Brown, & Fryxell (1988) to reproduce the flares from EXO 2030+375.

5.1 Observations and Data analysis

We analysed all the public and our private *INTEGRAL* data (see Chapter 3), between 2003 and 2009, where the SFXTs IGR J16479−4514, XTE J1739−302, AX J1841.0−0536 and IGR J17544−2619 were within 15° from the center of the field of view. This resulted in 14426 Science Windows, corresponding to a total exposure time of $\sim$ 30 Ms. We considered in our analysis also the other SFXTs (and candidate SFXTs) observed in the selected ScWs (see Table 5.1). We analysed IBIS/ISGRI and JEM-X data using the Off-line Scientific Analysis package OSA 8.0 (Goldwurm et al. 2003). For the spectral analysis, which was performed with XSPEC (ver. 11.3), we added a 2% systematic error to both IBIS/ISGRI and JEM-X data sets.

For each source reported in Table 5.1, we extracted the IBIS/ISGRI lightcurve at a ScW time resolution ($\sim$ 2000 s), in the energy range 20−40 keV, and we considered only the pointings where the sources are detected with at least a 5σ significance. For each source, Table 5.1 reports the num-

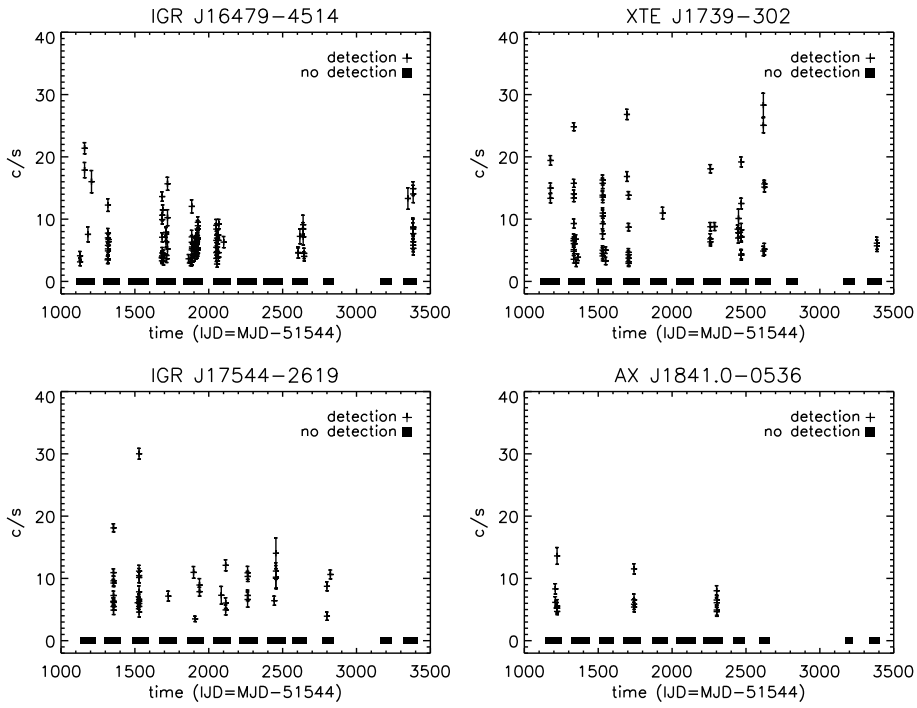

Figure 5.1: IBIS/ISGRI lightcurves of IGR J16479−4514, XTE J1739−302, IGR J17544−2619, AX J1841.0−0536 ($20-40$ keV). A binned time corresponding to the ScW duration (~ 2000 s) has been used.

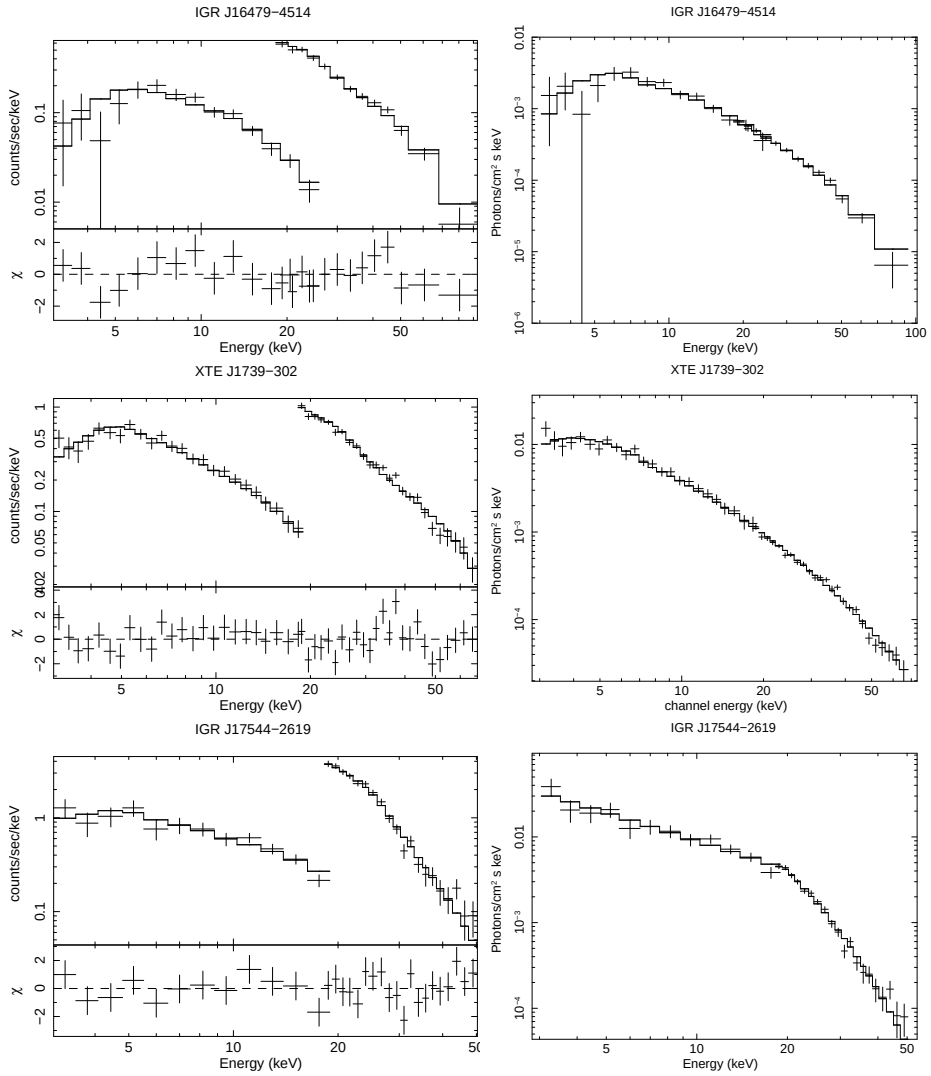

Figure 5.2: Joint JEM-X plus IBIS/ISGRI counts spectra, together with residuals in units of standard deviations (left panels) and unfolded spectra (right panels) for IGR J16479−4514, XTE J1739−302, and IGR J17544−2619 (see Table 5.4).

Table 5.1: Total exposure time $T_{\rm exp}$, duration and number of ScWs where the source is detected with a significance greater than 5.

Source	$T_{\rm exp}$ (d)	Duration (d) $S/N > 5$	# ScWs $S/N > 5$	# Outbursts
IGR J16479-4514	115.74	3.19	107	38
XTE J1739-302	260.42	2.16	65	18
IGR J17544-2619	259.92	1.33	43	14
AX J1841.0-0536	83.23	0.41	16	4
IGR J18483-0311	84.61	2.68	90	13
SAX J1818.6-1703	179.45	1.08	34	11
IGR J16465-4507	110.25	0.27	10	2
IGR J16418-4532	112.87	1.45	40	23
AX J1820.5-1434	120.95	0.09	4	2
AX J1845.0-0433	77.85	0.21	7	7
IGR J16195-4945	105.22	0.14	4	3
IGR J16207-5129	101.67	0.48	15	9
IGR J17407-2808	234.75	0.12	4	3
XTE J1743-363	232.04	0.48	20	7

ber of outbursts[1] identified. For each outburst observed, we also extracted IBIS/ISGRI lightcurves (18−60 keV) with a bin time of 50 s, and an IBIS/ISGRI spectrum in the energy range 18−100 keV. We found that the outbursts are characterized by a flaring activity. Due to its smaller field of view, we were able to extract the JEM-X spectra in only a few pointings.

5.2 Results

With IBIS/ISGRI we discovered several previously unnoticed outbursts from the following sources: XTE J1739−302, IGR J16479−4514, IGR J17544−2619, IGR J18483−0311, AX J1845.0−0433, IGR J16195−4945, IGR J16465−4507, IGR J17407−2808, IGR J16207−5129, and IGR J16418−4532. We report these outbursts in Table 5.2 and 5.3, together with the mean flux and best fit parameters of the IBIS/ISGRI spectra.

Figure 5.1 displays the 20−40 keV IBIS/ISGRI lightcurves of IGR J16479−4514, XTE J1739−302, IGR J17544−2619 and AX J1841.0−0536 collected from 2003 to 2009, where each "detection" refers to the average flux observed during each ScW, when the sources are detected with a significance $> 5\sigma$.

[1]We defined *outburst* as an X−ray emission detected by IBIS/ISGRI with significance $> 5\sigma$, and separated by adjacent outbursts by at least ∼1 day of inactivity (source below the IBIS/ISGRI threshold of detectability). An outburst can be composed by one or a series of flares with a typical duration of $\sim 10^2 - 10^4$ s each.

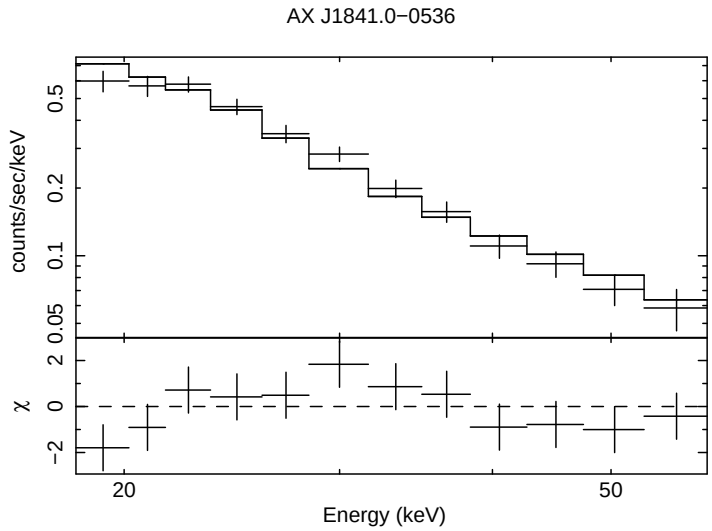

Figure 5.3: Average IBIS/ISGRI counts spectra of AX J1841.0−0536 (see Table 5.4), and residuals (lowest panels) in units of standard deviations.

Solid boxes represent the observations where the sources are not detected ($< 5\sigma$). For most of the time each source is not significantly detected.

No evidence of spectral variability has been found between different outbursts of these four SFXTs. To achieve the best statistics, we extracted an average JEM-X+IBIS/ISGRI outburst spectrum for each source (Figures 5.2 and 5.3). We did not extract an average JEM-X spectrum for AX J1841.0−0536 because we detected the source only in one pointing, with a low flux. The models which best fit the average spectra are reported in Table 5.4.

5.2.1 Clumpy wind in IGR J16479−4514

The results of our analysis of all available *INTEGRAL* observations of SFXTs can be compared with quantitative expectations from our new clumpy wind model (Ducci et al. 2009). A meaningful comparison can be performed only in SFXTs where a large number of flares has been observed. For this reason we will concentrate only on IGR J16479−4514. In order to apply the model, we have to establish the stellar parameters of the system and to confirm the eclipse duration.

In Figure 5.4 we show the IBIS/ISGRI ScWs where IGR J16479−4514 has been detected in outburst, folded on the orbital period of the system assuming a zero time $t_0 = 54546.742$ MJD (Bozzo et al. 2008b). This histogram is consistent with the presence of an eclipse with duration $\Delta t \approx 0.6$ d (Jain, Paul, & Dutta 2009).

Table 5.2: Summary of the new flares discovered of 7 confirmed SFXTs (IBIS/ISGRI data). We fitted the spectra with a powerlaw or a bremsstrahlung model.

Date (UTC)	Mean Flux (erg cm^{-2} s^{-1})	kT (keV)/Γ	χ^2_ν (d.o.f.)
XTE J1739−302:			
2009 Apr. 8, 16:49−18:46	4×10^{-10}	$\Gamma = 2.8^{+0.5}_{-0.5}$	0.99 (10)
IGR J16479-4514:			
2003 Feb. 2 19:07−22:30	2.5×10^{-10}	$\Gamma = 2.6^{+0.5}_{-0.5}$	0.76 (9)
2004 Aug. 9, 02:26−04:24	3.0×10^{-10}	$kT = 41^{+45}_{-17}$	0.52 (13)
2004 Aug. 20, 07:27−12:58	2.6×10^{-10}	$\Gamma = 2.1^{+0.5}_{-0.5}$	0.73 (10)
2004 Sep. 10, 01:14−02:12	2.5×10^{-10}	$kT = 19^{+19}_{-8}$	0.4 (12)
2009 Mar. 1, 16:56−17:54	10^{-9}	$\Gamma = 2.7^{+0.7}_{-0.6}$	1.2 (9)
2009 Apr. 6, 6:16−13:09	7.2×10^{-10}	$kT = 34^{+7}_{-5}$	1.45 (12)
IGR J17544-2619:			
2004 Feb. 27, 14:18−14:45	4.2×10^{-10}	$\Gamma = 3.1^{+0.9}_{-0.8}$	1.27 (8)
2006 Sep. 20, 09:58−13:47	6.9×10^{-10}	$kT = 18^{+29}_{-8}$	1.38 (7)
IGR J18483-0311:			
2004 Nov. 3, 00:05−00:31	3.3×10^{-10}	$kT = 22^{+48}_{-11}$	1.01 (11)
2005 Oct. 16, 07:34−08:30	1.7×10^{-10}	$kT = 21^{+39}_{-10}$	1.19 (11)
2005 Oct. 19, 20:48−20, 18:40	3.1×10^{-10}	$\Gamma = 2.8^{+0.3}_{-0.3}$	1.42 (10)
2006 Apr. 25, 14:04−14:33	5.0×10^{-10}	$kT = 40^{+21}_{-21}$	1.54 (11)
AX J1845.0-0433:			
2006 Sep. 3, 17:52−18:28	4.6×10^{-10}	$\Gamma = 2.4^{+0.5}_{-0.5}$	0.83 (11)
IGR J16195-4945:			
2004 Aug. 20, 04:40−06:27	2.6×10^{-10}	$\Gamma = 2.0^{+0.6}_{-0.6}$	0.73 (10)
2005 Feb. 18, 13:25−14:22	2.6×10^{-10}	$\Gamma = 2.0^{+1.1}_{-0.9}$	0.61 (8)
IGR J16465-4507:			
2004 Aug. 9, 22:12−10, 02:53	2.3×10^{-10}	$\Gamma = 2.5^{+0.5}_{-0.5}$	0.86 (10)

Table 5.3: Summary of the new flares discovered of 3 candidate SFXTs (IBIS/ISGRI data). We fitted the spectra with a powerlaw or a bremsstrahlung model.

Date (UTC)	Mean Flux (erg cm^{-2} s^{-1})	kT (keV)/Γ	χ^2_ν (d.o.f.)
IGR J17407-2808:			
2003 Sep. 21, 04:27−04:29	2.6×10^{-9}	$kT = 44^{+35}_{-16}$	1.38 (10)
2006 Sep. 20, 12:18−13:47	4.9×10^{-10}	$\Gamma = 1.9^{+0.3}_{-0.3}$	0.55 (14)
IGR J16207-5129:			
2004 Jan. 21, 09:23−09:56	5.8×10^{-10}	$kT = 38.^{+81}_{-17}$	1.37 (10)
2005 Feb. 07, 06:48−07:45	2.0×10^{-10}	$kT = 30^{+94}_{-16}$	0.69 (11)
2005 Feb. 11, 03:04−04:01	2.2×10^{-10}	$\Gamma = 2.0^{+0.9}_{-0.8}$	0.78 (10)
2005 Feb. 13, 10:59−11:56	2.2×10^{-10}	$\Gamma = 1.8^{+0.8}_{-0.8}$	1.06 (10)
2005 Feb. 18, 22:41−19, 01:41	3.2×10^{-10}	$\Gamma = 2.2^{+0.3}_{-0.3}$	1.06 (11)
IGR J16418-4532:			
2003 Feb. 3, 12:37−13:13	4.6×10^{-10}	$\Gamma = 1.8^{+1.2}_{-1.1}$	1.07 (5)
2003 Mar. 4, 21:39−22:07	2.1×10^{-10}	$kT = 15^{+16}_{-6}$	1.12 (14)
2004 Feb. 18, 03:42−04:16	3.0×10^{-10}	$\Gamma = 3.2^{+1.2}_{-1.0}$	1.75 (14)
2004 Mar. 20, 21:27−21, 11:24	2.5×10^{-10}	$\Gamma = 3.0^{+0.7}_{-0.6}$	0.96 (14)
2004 Aug. 9, 13:57−14:56	1.9×10^{-10}	$\Gamma = 2.7^{+0.9}_{-0.7}$	0.70 (14)
2004 Aug. 24, 13:32−14:56	2.0×10^{-10}	$kT = 20^{+12}_{-7}$	1.00 (14)
2005 Feb. 13, 02:17−15:02	1.6×10^{-10}	$kT = 15^{+6}_{-4}$	1.34 (14)
2005 Feb. 22, 04:54−06:14	1.5×10^{-10}	$kT = 22^{+23}_{-10}$	1.13 (14)
2005 Feb. 24, 05:20−07:10	1.3×10^{-10}	$\Gamma = 2.8^{+1.1}_{-0.9}$	0.87 (14)
2005 Feb. 27, 05:41−Mar. 1, 12:09	1.9×10^{-10}	$kT = 21^{+7}_{-5}$	1.02 (14)
2005 Mar. 8, 04:35−05:35	3.2×10^{-10}	$kT = 14^{+8}_{-3}$	1.16 (14)
2005 Mar. 18, 14:09−14:42	1.3×10^{-10}	$\Gamma = 4.2^{+5.8}_{-1.4}$	0.62 (7)
2005 Aug. 26, 18:08−27, 08:56	2.5×10^{-10}	$kT = 28^{+15}_{-9}$	1.16 (14)
2005 Oct. 2, 00:32−01:15	3.6×10^{-10}	$\Gamma = 2.6^{+1.6}_{-1.4}$	0.76 (8)
2006 Aug. 13, 23:48−14, 21:01	2.9×10^{-10}	$kT = 20^{+6}_{-4}$	1.65 (14)
2007 Feb. 19, 03:58−04:39	3.9×10^{-10}	$\Gamma = 2.3^{+0.9}_{-0.8}$	0.74 (8)
2007 Mar. 15, 04:43−05:27	5.4×10^{-10}	$kT = 15^{+12}_{-5}$	1.48 (8)
2007 Mar. 30, 02:19−03:01	3.0×10^{-10}	$\Gamma = 2.0^{+1.9}_{-1.6}$	0.87 (5)
2009 Apr. 7, 10:15−10:43	4.8×10^{-10}	$\Gamma = 2.8^{+0.9}_{-0.8}$	0.92 (10)
2009 Apr. 7, 21:13−21:41	4.1×10^{-10}	$\Gamma = 2.28^{+0.99}_{-0.91}$	1.22 (9)

Table 5.4: Best fit parameters of the average spectra of IGR J16479−4514, XTE J1739−302, and IGR J17544−2619 observed with JEM-X and IBIS/ISGRI (see Figure 5.2), and best fit parameters of the average spectrum of AX J1841.0−0536 observed with IBIS/ISGRI (see Figure 5.3). Γ is the power-law photon index, $E_{\rm c}$ is the cutoff energy, $E_{\rm F}$ is the e-folding energy.

	IGR J16479-4514 (JEM-X & IBIS/ISGRI)	XTE J1739-302 (JEM-X & IBIS/ISGRI)
Fit model	cutoff-powerlaw	cutoff-powerlaw
$N_{\rm H}$ (10^{22} cm^{-2})	23^{+17}_{-13}	$8.6^{+4.1}_{-3.6}$
Γ	$1.2^{+0.4}_{-0.4}$	$1.6^{+0.2}_{-0.2}$
$E_{\rm c}$, $E_{\rm F}$ (keV)	$E_{\rm c} = 25.1^{+12}_{-6}$	$E_{\rm c} = 26.5^{+6.5}_{-4.7}$
χ^2_ν (d.o.f.)	0.90 (23)	1.12 (45)
	IGR J17544-2619 (JEM-X & IBIS/ISGRI)	AX J1841.0-0536 (IBIS/ISGRI)
Fit model	powerlaw with high-energy cutoff	powerlaw
$N_{\rm H}$ (10^{22} cm^{-2})	$0.2^{+8}_{-0.15}$	–
Γ	$1.1^{+0.3}_{-0.1}$	$2.50^{+0.16}_{-0.15}$
$E_{\rm c}$ (keV)	$19.7^{+1.5}_{-1.2}$	–
$E_{\rm F}$ (keV)	$8.1^{+1.0}_{-0.7}$	–
χ^2_ν (d.o.f.)	1.03 (27)	1.20 (10)

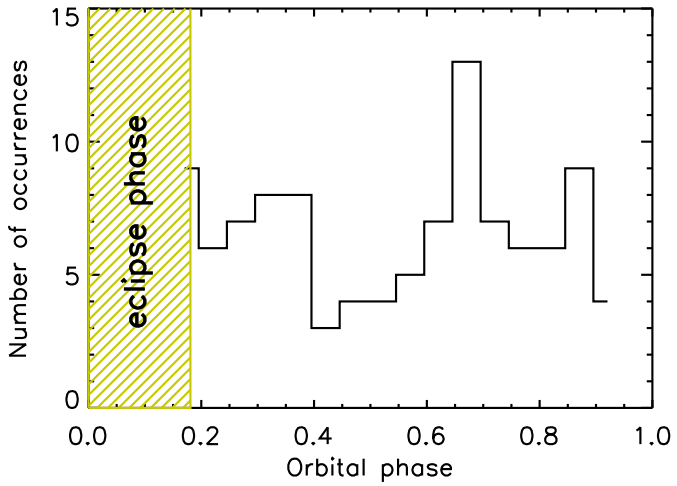

Figure 5.4: Folding on a period of 3.3194 d of the ScWs where IGR J16479−4514 is detected with significance $> 5\sigma$. The start time of the eclipse is t_0 = 54546.742 MJD, and the duration is 0.6 d.

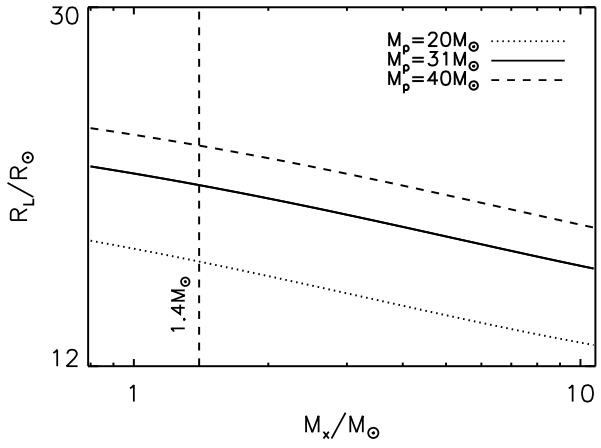

Figure 5.5: $R_{\rm L}$ for different values of $q = M_{\rm p}/M_{\rm x}$ (see Equation 5.1).

The Roche Lobe radius $R_{\rm L}$ of IGR J16479−4514, adopting the approximated formula obtained by Eggleton (1983), is the following:

$$R_{\rm L} = a\frac{0.49q^{2/3}}{0.6q^{2/3} + \ln(1 + q^{1/3})} \quad 0 < q < \infty \tag{5.1}$$

where a is the orbital separation, $q = M_{\rm p}/M_{\rm x}$ is the mass ratio[2], with a circular orbit assumed. Figure 5.5 reports the results obtained for $R_{\rm L}$. Roche Lobe overflow (RLO) is not expected in this system because RLO would imply a much higher mass transfer to the compact object and thus a much higher X−ray luminosity. Assuming that the compact object is a neutron star with $M_{\rm x} = 1.4$ M$_\odot$, we make the hypothesis that the primary star has mass $M_{\rm p} = 31$ M$_\odot$ and radius $R_{\rm p} = 19$ R$_\odot$. This set of parameters is in agreement with the expected values for a O8.5I star (e.g. Martins, Schaerer, & Hillier 2005; Vacca, Garmany, & Shull 1996), and excludes the Roche Lobe overflow. However, we point out that other parameters for $M_{\rm x}$, $M_{\rm p}$, and $R_{\rm p}$ are allowed.

We applied our clumpy wind model in its spherical configuration (Chapter 4) to the IBIS/ISGRI observations of IGR J16479−4514, for which we have a significant number of flares ($N_{\rm fl} = 80$). Our model assumes that a fraction f of the mass lost by the supergiant wind is in form of clumps ($f = \dot{M}_{\rm cl}/\dot{M}_{\rm tot}$). The clumps are assumed to follow a power-law mass distribution $p(M_{\rm cl}) \propto M_{\rm cl}^{-\zeta}$ in the mass range $M_{\rm a} - M_{\rm b}$, a power-law radius distribution $\dot{N} \propto R_{\rm cl}^{\gamma}$, and a β-velocity law. We compared the observed and calculated number of flares, their luminosity distribution, the X−ray

[2] $M_{\rm p}$ is the mass of the primary star (i.e. the supergiant star), and $M_{\rm x}$ is the mass of the compact object.

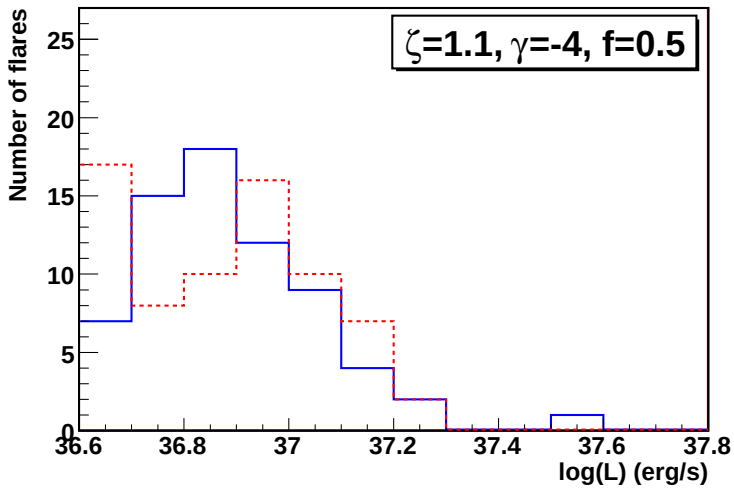

Figure 5.6: Comparison between observed (solid line) and calculated (dashed line) distributions of the flare luminosities of IGR J16479−4514.

luminosity outside flares and the average time duration of flares. For each of the 80 flares found, we derived the peak luminosity in the energy range $1-100$ keV by means of the spectral parameters found by fitting simultaneously the IBIS/ISGRI and JEM-X data (see Table 5.4). The luminosity $(1-100$ keV) outside flares is $L_{\rm out-flares} \lesssim 10^{35}$ erg s^{-1} (Sguera et al. 2008).

To avoid the selection effect given by the fact that the 5σ detection threshold varies with the position of the source in the field of view, we have considered only those flares with luminosities greater than $L_{\rm lim} \approx 4 \times 10^{36}$ erg s^{-1}, where we have calculated $L_{\rm lim}$ from the average 5σ detection threshold count−rate at an offset angle from the pointing position of $\theta = 15°$.

Figure 5.6 shows the comparison between the observed and calculated distributions of flare luminosities which results in the best agreement. The wind parameters obtained are reported in Table 5.5, with $\dot{M} = 10^{-7}$ M$_\odot$ yr^{-1}, $v_\infty = 1800$ km s^{-1}, $\beta = 1$, $M_{\rm a} = 5 \times 10^{19}$ g, $M_{\rm b} = 5 \times 10^{21}$ g, $\zeta = 1.1$, $f = 0.5$, $\gamma = -4$, and, since $T_{\rm eff} = 34000$ K, the multiplier parameters adopted from Shimada et al. (1994) are: $k = 0.375$, $\alpha = 0.522$, $\delta = 0.099$. With this set of wind parameters we are able also to reproduce the observed X−ray luminosity outside bright flares and the average flare duration.

5.3 Discussion

The wind parameters obtained for IGR J16479−4514 in Section 5.2.1 are in agreement with those of the sources previously studied (see Ducci et al.

2009; Romano et al. 2010), with the exception of f ($f = 0.75$ for the other persistent HMXBs and SFXTs). Moreover, the mass loss rate found for IGR J16479−4514 ($\dot{M} = 10^{-7}$ M$_\odot$ yr^{-1}) is lower if compared to the typical mass loss rate from a O8.5I star, which is of the order of $\dot{M} \approx 4 \times 10^{-6}$ M$_\odot$ yr^{-1} (see Table 5.5). This difference could be due to the fact that the mass loss rates derived from homogeneous-wind model measurements with the Hα method are overestimated by a factor 2-10 if the wind is clumpy (see e.g. Lépine & Moffat 2008; Hamann, Feldmeier, & Oskinova 2008). Another possibility is that the X−ray flaring behaviour in IGR J16479−4514 is not totally due to the accretion of clumps, but other mechanisms could be at work, like, e.g. the centrifugal inhibition of accretion, the formation of transient accretion disks, or the Rayleigh−Taylor instability. The role of these mechanisms in SFXTs will be treated in this section.

5.3.1 X−ray photoionization

Direct accretion

Here we discuss the effects of X−ray photoionization on the mass transfer onto a neutron star in a close binary system, modifying the analytic model by Ho & Arons (1987) and applying it to SFXTs.

In HMXBs, the wind reaching the compact object is overionized by the X−ray photons produced by the compact object (Hatchett & McCray 1977). This high ionization alters the dynamics of the line-driven stellar wind of the primary: the wind becomes highly ionized and does not interact anymore with the UV photons emitted by the primary, which drive the wind. Hence, the wind velocity and density around the neutron star is different from what expected neglecting the X−ray photoionization. The accretion onto the compact object is modified accordingly since it depends onto the wind velocity.

For a source with a X−ray luminosity $L_{\rm x}$, the ionization state ξ of the wind at a radius R_ξ is defined by:

$$\xi \equiv \frac{L_{\rm x}}{n(r_\xi) R_\xi^2} \tag{5.2}$$

where $n(r_\xi)$ is the particle number density at a distance $r_\xi = D - R_\xi$ from the supergiant (see Figure 5.7). The parameter ξ defined in Equation (5.2) determines the thermal and ionic state of the gas, assuming optically thin gas in thermal balance (see Tarter, Tucker, & Salpeter 1969).

Several attempts have been made to include the effects of X−ray ionization in the accretion of HMXBs (e.g. Ho & Arons 1987; MacGregor & Vitello 1982; Blondin et al. 1990; Stevens & Kallman 1990; Stevens 1991). Here we adopt the analytic model developed by Ho & Arons (1987). They assumed a spherically symmetric wind, ionized by the X−rays from the compact object. They assumed that the radiation line force is turned off at

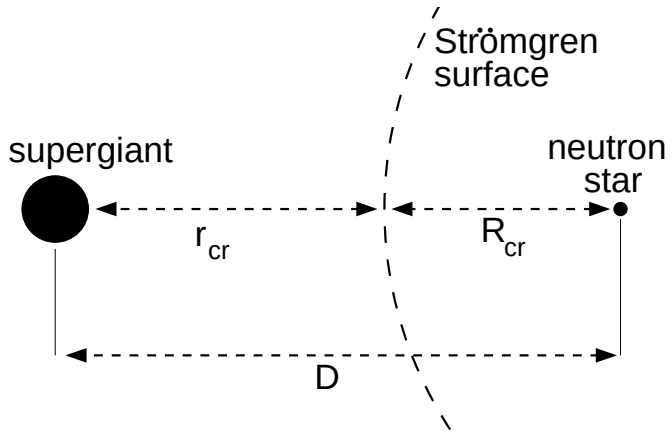

Figure 5.7: Schematic representation of a Strömgren surface produced by a neutron star orbiting around a supergiant. The labels indicates the distance of this surface which respect the two stars, accordingly to Ho & Arons (1987).

$\xi_{\rm cr} = 10^4$ erg cm s^{-1}. Thus, the wind follows the standard β-velocity law (with $\beta = 0.5$) up to a distance $R_{\rm cr}$ from the compact object such that $L_{\rm x}/[n(R_{\rm cr})R_{\rm cr}^2] = \xi_{\rm cr}$, i.e. where the wind is sufficiently ionized to become transparent to the UV photons. Inside this sphere with the neutron star in the centre, the radiation force (Kudritzki & Puls 2000) is turned off and the wind velocity is assumed constant. The wind velocity will be lower in the vicinity of the compact object (with respect to the non-ionized case), leading to an enhancement of the mass accretion rate. With these assumptions, Ho & Arons (1987) developed a model to describe the accretion of the wind, taking into account the feedback effect of the X−rays which ionize the wind, and consequently controls the mass transfer onto the compact object (see Section 1.3.5).

We propose the following important changes to this model:

1. a generic β-velocity law, with β not fixed;

2. we consider the orbital velocity of the neutron star in the calculations, which cannot be neglected in close binary systems such as IGR J16479−4514 ($P_{\rm orb} = 3.32$ d, Jain et al. 2009);

3. we modify the equations developed by Ho & Arons (1987) to take into account the possibility that the mass loss rate towards the neutron star is reduced because of the high ionization state of the wind, which reduces the radiative acceleration given by the absorption and re-emission of UV photons (emitted by the supergiant) in the resonance lines of ions forming the wind. Assuming for the wind particles a velocity distribution centered on $v_{\rm w}(r_\xi)$ (Equation 5.3), a part of

them may decelerate enough not to be able to reach the neutron star;

4. a force cutoff value $\xi_{\rm cr} = 3 \times 10^2$ erg cm s^{-1} (Stevens 1991).

We assumed the standard wind velocity law obtained from the radiation line-driven mechanism of Castor, Abbott, & Klein (1975):

$$v_{\rm w}(r_\xi) = v_\infty \left(1 - \frac{r_{\rm p}}{r_\xi}\right)^\beta \tag{5.3}$$

where r_ξ is the distance from the primary (see Figure 5.7), and v_∞ is the terminal velocity.

In wind-fed systems, the mass accretion rate is defined as the flux of matter passing through a circular area with radius $R_{\rm acc}$, and is written as:

$$\dot{M}_{\rm accr} = \left[\frac{\dot{M}}{4\pi D^2 v_{\rm w}} v_{\rm rel}\right] \pi R_{\rm acc}^2 \tag{5.4}$$

where $\dot{M}$ is the wind mass loss rate from the supergiant, the factor contained in square brackets is the stellar wind flux at a distance D from the primary, $v_{\rm rel}$ is the relative velocity between the wind and the neutron star, and $R_{\rm acc}$ is the accretion radius. where $M_{\rm x} = 1.4$ M$_\odot$ is the mass of the neutron star and $c_{\rm s}$ is the sound velocity. Hence, the accretion luminosity, given by Equations (5.3, 5.4, 1.15) is:

$$L_{\rm x} = \frac{GM_{\rm x}}{R_{\rm x}} \dot{M}_{\rm accr} = \frac{(GM_{\rm x})^3}{R_{\rm x}} \frac{\dot{M}}{D^2 v_{\rm w}(r_\xi)} \frac{1}{(v_{\rm rel}^2 + c_{\rm s}^2)^{3/2}} \ . \tag{5.5}$$

The radius $r_{\rm lim}$ where the sum of the radiation force $g_{\rm e}$, due to scattering of continuum photons by free electrons, and the gravitational forces of the primary and neutron star acting on a parcel of the wind is zero (see Figure 5.8) can be derived as follows:

$$\frac{GM_{\rm p}}{r_{\rm lim}^2}(1 - \Gamma_{\rm e}) = \frac{GM_{\rm x}}{(D - r_{\rm lim})^2} \tag{5.6}$$

where $\Gamma_{\rm e}$, defined as

$$\Gamma_{\rm e} = \frac{\sigma_{\rm e} L_{\rm p}}{4\pi c G M_{\rm p}} \ , \tag{5.7}$$

is obtained from the formula of the force due to electron scattering:

$$g_{\rm e} = \frac{\sigma_{\rm e} L_p}{4\pi c r^2} = \frac{GM_{\rm p}}{r^2}\Gamma_{\rm e} \ , \tag{5.8}$$

where $\sigma_{\rm e}$ is the opacity for electron scattering, assumed to be equal to $\sim$ 0.3 cm^2 g^{-1} and constant, as suggested by Lamers & Cassinelli (1999).

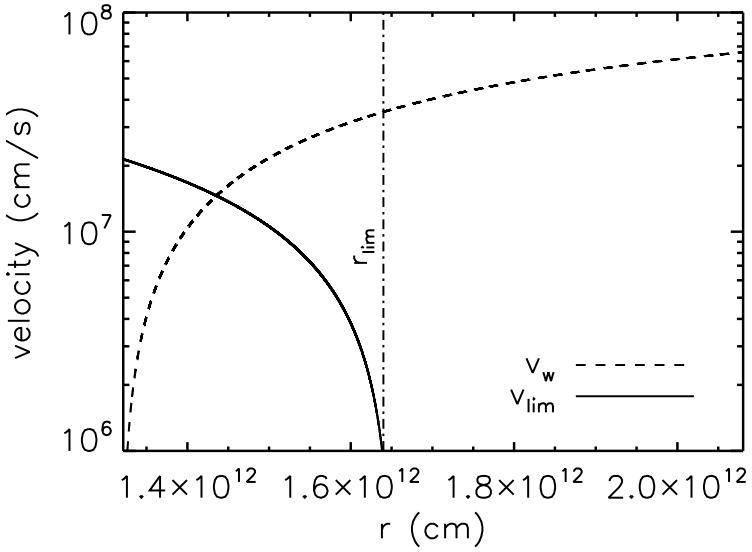

Figure 5.8: Schematic representation of the wind velocity, described by Equation (5.3), and the limit-velocity (Equation 5.11). We assumed $v_\infty = 1800$ km s^{-1}, $\beta = 1$, $R_\mathrm{p} = 19$ R$_\odot$ and $M_\mathrm{p} = 31$ M$_\odot$, $M_\mathrm{x} = 1.4$ M$_\odot$.

When the radiation force is turned off, a parcel of gas is only subject to the gravitational force of the two stars and to the force due to electron scattering. Assuming that this parcel of gas reaches the distance r_lim with null velocity, the initial velocity can be obtained from the momentum equation:

$$v\frac{dv}{dr} = -\frac{GM_\mathrm{p}}{r^2}(1-\Gamma_\mathrm{e}) + \frac{GM_\mathrm{x}}{(D-r)^2} \ . \tag{5.9}$$

For a particle starting at a distance r, with velocity v, the solution obtained from Equation (5.9) is:

$$\int_0^v v dv = -\int_{r_\mathrm{lim}}^r \frac{GM_\mathrm{p}}{r'^2}(1-\Gamma_\mathrm{e})dr' + \int_{r_\mathrm{lim}}^r \frac{GM_\mathrm{x}}{(D-r')^2}dr'. \tag{5.10}$$

Thus:

$$\begin{aligned} v_\mathrm{lim}(r) &= \left[-2GM_\mathrm{p}(1-\Gamma_\mathrm{e})\left(\frac{1}{r_\mathrm{lim}} - \frac{1}{r}\right)\right. \\ &- \left. 2GM_\mathrm{x}\left(\frac{1}{D-r_\mathrm{lim}} - \frac{1}{D-r}\right)\right]^{1/2} \ . \end{aligned} \tag{5.11}$$

The wind particles have a temperature of $\approx 10^5$ K (Lamers & Cassinelli 1999). Assuming for the particles velocity, at a distance r from the primary, a gaussian distribution centered on $v_\infty(1-R_\mathrm{p}/r)^\beta$ with $\sigma_\mathrm{v} \sim 10^7$ cm s^{-1}, it

is possible to calculate the density probability to have particles with $v \gtrsim v_{\rm lim}$ at $r = r_{\rm cr}$:

$$S \equiv \frac{1}{\sqrt{2\pi}\sigma_{\rm v}} \int_{v_{\rm lim}}^{+\infty} {\rm e}^{-\frac{(v-v_{\rm w})^2}{2\sigma_{\rm v}^2}} dv \tag{5.12}$$

where $v_{\rm w}$ is given by Equation (5.3).

We now propose a new version of the *self-consistent steady state equation* developed by Ho & Arons (1987), improved with the considerations described above. The accretion luminosity $L_{\rm a}$ from Equations (5.3), (5.5), and (5.12) is then:

$$L_{\rm a}(r_\xi) = \frac{(GM_{\rm x})^3}{R_{\rm x}} \frac{\dot{M}S(r_\xi)}{D^2 v_\infty (1 - R_{\rm p}/r_\xi)^\beta} \frac{1}{(v_{\rm rel}^2 + c_{\rm s}^2)^{3/2}} \tag{5.13}$$

which we call, following the nomenclature of Ho & Arons (1987), the *accretion equation*. Then we obtain the *feedback equation* from Equations (5.2), (5.3), (5.4), (1.15), (5.12):

$$L_{\rm b}(r_\xi) = \xi_{\rm cr} \frac{\dot{M}S(r_\xi)(D - r_\xi)^2}{4\pi r_\xi^2 \mu m_{\rm p} v_\infty (1 - R_{\rm p}/r_\xi)^\beta} \tag{5.14}$$

where μ is the mean atomic weight. The steady state solution is given by: $L_{\rm a}(r_\xi) = L_{\rm b}(r_\xi)$, thus, by equating Equations (5.13) and (5.14), it is possible to obtain the X−ray luminosity $L_{\rm x}$ and the corresponding Strömgren radius $r_{\rm cr}$.

We assume for the force cutoff value $\xi_{\rm cr} = 3 \times 10^2$ erg cm s^{-1}, which is two orders of magnitude smaller than the value considered by Ho & Arons (1987), but in agreement with the calculations of Stevens (1991), who found that for this value the wind material is already basically completely ionized.

We calculate the X−ray luminosity and $r_{\rm cr}$ of IGR J16479−4514 from the steady state solution obtained from Equations (5.13) and (5.14), assuming the parameters reported in Table 5.5. We obtain an expected luminosity of $L_{\rm x} \approx 10^{37}$ erg s^{-1}, reached by the neutron star when $r_{\rm cr} = 1.33 \times 10^{12}$ cm. This luminosity level is in agreement with the peak flare luminosities observed. However, IGR J16479−4514 has an out-of-flare luminosity of the order of $10^{34} - 10^{35}$ erg s^{-1} (Sidoli et al. 2008). This luminosity level can be obtained possibly invoking the presence of the centrifugal inhibition of accretion.

For IGR J17544−2619 we assumed the system parameters suggested by Clark et al. (2009), with eccentricity $e = 0.4$. We found that the X−ray photoionization acts to increase the difference in luminosity when the neutron star is at periastron ($L_{\rm x} \approx 10^{37}$ erg s^{-1}) and apastron ($L_{\rm x} \approx 10^{35}$ erg s^{-1}, see Table 5.6). In fact, at periastron the wind is highly ionized by the X−ray source ($r_{\rm cr} \simeq 0.9 \times 10^{12}$ cm), leading to a low wind velocity in the vicinity of the neutron star ($v_{\rm rel} \simeq 230$ km s^{-1}) and accordingly to a higher

Table 5.5: System Parameters for IGR J16479−4514 and IGR J17544−2619.

Parameters	Sources	
	IGR J16479−4514	IGR J17544−2619
Spectral type	O8.5I [a]	O9I [a]
$P_{\rm orb}$ (d)	3.3194 ± 0.0010[b]	4.926 ± 0.001[g]
$M_{\rm p}$ ($M_\odot$)	31 [c]	$25 - 28$ [g]
$R_{\rm p}$ ($R_\odot$)	19 [c]	< 23 if $e = 0$ [g]
		~ 12.7 if $e \sim 0.4$ [g]
$L_{\rm p}$ ($L_\odot$)	$\approx 5 \times 10^5$ [d]	$\approx 4.6 \times 10^5$ [d]
$\dot{M}$ ($M_\odot$ yr^{-1})	$\sim 4 \times 10^{-6}$ [e]	$\sim 2.4 \times 10^{-6}$ [e]
$M_{\rm x}$ ($M_\odot$)	1.4 [f]	1.4 [f]
v_∞ (km s^{-1})	1800	1800
β	1	1

[a] Rahoui et al. (2008)

[b] Jain et al. (2009)

[c] obtained assuming no Roche-Lobe overflow (see section 5.2.1)

[d] Vacca et al. (1996); Martins et al. (2005)

[e] Calculated with the Vink formula (Vink, de Koter, & Lamers 2000)

[f] Assumed

[g] Clark et al. (2009)

Table 5.6: Results for IGR J17544−2619.

	Periastron	Apastron
$\dot{M}$ ($M_\odot$ yr^{-1})	2.4×10^{-6}	2.4×10^{-6}
$r_{\rm cr}$ (cm)	$\sim 0.9 \times 10^{12}$	$\sim 3.3 \times 10^{12}$
$L_{\rm x}$ (erg s^{-1})	$\gtrsim 10^{37}$	$\sim 2 \times 10^{35}$
$v_{\rm rel}$ (km s^{-1})	~ 230	~ 1400
$R_{\rm m}$ (cm)	10^{10}	4.5×10^{10}

X-ray luminosity (since $L_{\rm x} \propto v_{\rm rel}^{-3}$). At apastron the ionization is lower ($r_{\rm cr} \simeq 3.3 \times 10^{12}$ cm), therefore its effect on the wind velocity is small ($v_{\rm rel} \simeq 1400$ km s^{-1}).

Centrifugal inhibition of accretion

In this section we apply for the first time the centrifugal inhibition (c.i.) of accretion to the modified model of Ho & Arons (1987) described in Section 5.3.1.

The magnetospheric radius $R_{\rm m}$ is defined as the radius where the magnetic field pressure $B^2(R_{\rm m})/8\pi$ equals the ram pressure of the accreting plasma $\rho(R_{\rm m})v^2(R_{\rm m})$. We use the definition obtained by Davidson & Ostriker (1973):

$$R_{\rm m}(r_\xi) = \left[\frac{B_0^2 R_{\rm x}^6}{4\dot{M}_{\rm accr}(GM_{\rm x})^{1/2}}\right]^{2/7} \tag{5.15}$$

where B_0 is the surface magnetic field. When $R_{\rm m} \gtrsim R_{\rm co}$ (where $R_{\rm co}$ is the corotation radius), the accretion flow is halted at the magnetospheric boundary, which behaves like a closed barrier (Illarionov & Sunyaev 1975). The expected X−ray luminosity in this regime is:

$$L_{\rm m} = \frac{GM}{R_{\rm m}}\dot{M}_{\rm accr} \ . \tag{5.16}$$

The position of the magnetospheric radius depends also on the effect of the X−ray ionization on the accreting matter. Here we obtain the formula which gives the steady position of the magnetospheric radius and the related position of the Strömgren radius for which the accretion luminosity is equal to the feedback luminosity. The accretion Equation (5.13) can be written as follows:

$$L_{\rm a,c.i.}(r_\xi) = \frac{(GM_{\rm x})^3}{R_{\rm m}} \frac{\dot{M}S(r_\xi)}{D^2 v_\infty (1 - R_{\rm p}/r_\xi)^\beta} \frac{1}{(v_{\rm rel}^2 + c_{\rm s}^2)^{3/2}}. \tag{5.17}$$

We obtain $R_{\rm m}$ as a function of $r_{\rm cr}$ by equating $L_{\rm b}$ of the feedback Equation

Table 5.7: Model results for IGR J16479−4514. We calculate the magnetospheric radius $R_{\rm m}$ with Equation (5.15), assuming a magnetic field of $B_0 = 10^{12}$ Gauss. For IGR J16479−4514, the corotation radius is equal to the magnetospheric radius when $\dot{M} = 4 \times 10^{-6}$ M$_\odot$ yr^{-1} for a spin period of the neutron star of ~ 1 s.

	Direct accretion ($R_{\rm m} < R_{\rm co}$):	Centrifugal inhibition of accretion ($R_{\rm m} > R_{\rm co}$):
$\dot{M}$ (M$_\odot$ yr^{-1})	$\gtrsim 4 \times 10^{-6}$	4×10^{-6}
$r_{\rm cr}$ (cm)	$\sim 1.33 \times 10^{12}$	$\sim 2 \times 10^{12}$
$L_{\rm x}$ (erg s^{-1})	$\gtrsim 10^{37}$	$\gtrsim 8 \times 10^{34}$
$v_{\rm rel}$ (km s^{-1})	~ 460	~ 760
$R_{\rm m}$ (cm)	1.6×10^{8}	1.7×10^{8}

(5.14) to the $L_{\rm a,c.i.}$ of the accretion Equation (5.17):

$$R_{\rm m,c.i.}(r_\xi) = \frac{(GM_{\rm x})^3 4\pi\mu m_{\rm p}}{(v_{\rm rel}^2 + c_{\rm s}^2)^{3/2}\xi_{\rm cr}(D - r_\xi)^2} \ . \tag{5.18}$$

Hence, if the centrifugal inhibition of accretion is at work in an X−ray binary system where the X−ray ionization cannot be neglected, the steady values for $R_{\rm m}$ and $r_{\rm cr}$ can be derived by equating Equations (5.15) and (5.18):

$$R_{\rm m}(r_\xi) = R_{\rm m,c.i.}(r_\xi) \ . \tag{5.19}$$

In Table 5.7 we report the steady state solutions obtained for IGR J16479−4514 (assuming the system parameters reported in Table 5.5) in the case of direct accretion and in the case of centrifugal inhibition of accretion. Assuming a transition from direct accretion to the centrifugal inhibition of accretion for a mass-loss rate of $\dot{M} = 4 \times 10^{-6}$ M$_\odot$ yr^{-1}, we obtain steady state solutions in agreement with observations for a magnetic field of $B_0 \approx 10^{12}$ Gauss and a spin period of ≈ 1 s. When the neutron star enters the state of centrifugal inhibition of accretion, the X−ray luminosity is reduced, thus also the photoionization is lower; this leads to a shift of the magnetospheric radius to a higher value. The opposite transition (from centrifugal inhibition to direct accretion) needs $\dot{M}$ greater than 4×10^{-6} M$_\odot$ yr^{-1} (e.g. the accretion of a dense clump). This behaviour allows longer durations for the low-luminosity state. When $R_{\rm m} \approx R_{\rm co}$, the oblate spheroid shape of the magnetospheric boundary (see Jetzer, Strassle, & Straumann 1998) results in the intermediate luminosity state observed ($\sim 10^{35}$ erg s^{-1}) because simultaneously $R_{\rm m} < R_{\rm co}$ in the magnetic polar region and $R_{\rm m} > R_{\rm co}$ in the magnetic equatorial region (Campana et al. 2001; Perna, Bozzo, & Stella 2006).

5.3.2 Formation of an accretion disk

In the previous section we discussed the effect of X−ray photoionization in a close X−ray binary system like IGR J16479−4514, where a compact object

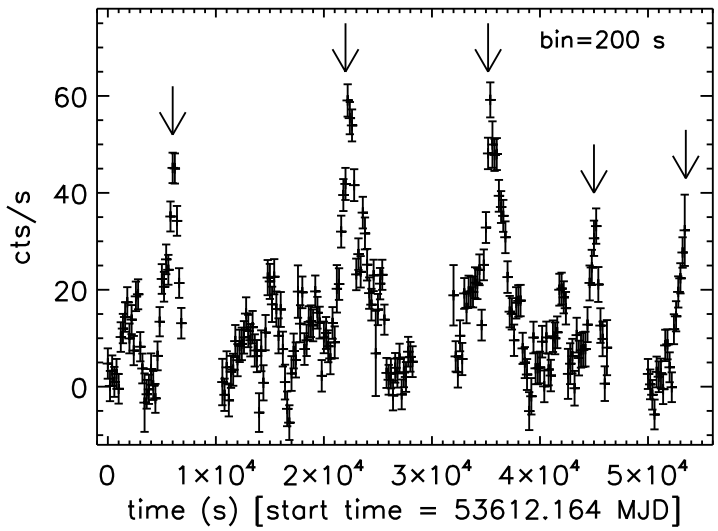

Figure 5.9: Lightcurve of the observation of XTE J1739−302, in the energy range $18 - 60$ keV (IBIS/ISGRI). Arrows indicates the peaks of luminosity.

accretes matter from a wind with a low relative velocity $v_{\rm rel} \approx 460$ km s^{-1}. In Section 5.3.1 we have excluded for this system the possibility of the formation of an accretion disk due to Roche Lobe overflow. However, it is also possible that an accretion disk forms from the capture of angular momentum from a slow wind (see Illarionov & Sunyaev 1975; Shapiro & Lightman 1976; Wang 1981). The existence of a disk in IGR J16479−4514 requires that the relative velocity between the neutron star and the wind is lower than $\simeq 500$ km s^{-1} (see equation [31] in Wang 1981), therefore the presence of a disk in IGR J16479−4514 cannot be ruled out. The formation of a transient disk from the mass and angular momentum capture from an asymmetric stellar wind can lead to a flaring activity, as proposed by Taam et al. (1988) to explain the recurrent flares observed in EXO 2030+375 (Parmar et al. 1989). Recently, the formation of transient disks has been proposed by Kreykenbohm et al. (2008) to explain part of the flaring behaviour of the persistent HMXB Vela X−1. In the model of Taam et al. (1988), the density and velocity inhomogeneities in the wind lead to an instability in the accretion flow. Because of this instability, the interaction of the accretion flow with the shock fronts of the accretion wake leads to the formation and dissipation of transient accretion disks (see e.g. Edgar 2004 and references therein for a recent review). In their model, Taam et al. (1988) gave an approximative formula for the time scale for the duration of flares:

$$\tau \sim \frac{6GM_{\rm x}}{v_{\rm rel}^3} \ . \tag{5.20}$$

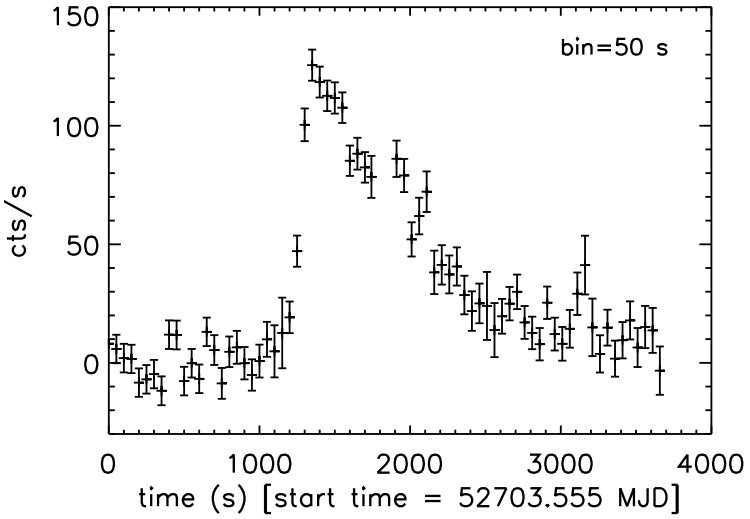

Figure 5.10: Lightcurve of an observation of IGR J16479−4514, in the energy range $18 - 60$ keV (IBIS/ISGRI).

Assuming relative velocities reported in Table 5.7 (in the case of direct accretion), we found for IGR J16479−4514 a time scale for the duration of flares of $\sim 10^3 - 10^4$ s, in agreement with the observed flare durations. The flares produced by the formation of transient accretion disks can be distinguished from those produced by the simple clump accretion by measuring the time derivative of the pulse period, which, in the first case, is expected to change sign for each flare (see Taam et al. 1988).

The SFXT XTE J1739−302 has shown a quasi-periodic flaring behaviour on 53612.164 MJD (see Figure 5.9), which could be ascribed to the mechanism of formation and dissipation of transient accretion disks described above. Adopting Equation (5.20), we obtain, from the measure of the flares durations ($\tau \sim 5000$ s), a relative velocity of $v_{\rm rel} \approx 600$ km s^{-1}. This value is in agreement with the $v_{\rm rel}$ expected from an X−ray binary system with a small orbital period ($\approx 3 - 7$ d), or with a higher orbital period and large eccentricity, where the effect of X−ray photoionization reduces significantly the wind velocity. This supports the hypothesis of Smith et al. (2006b) that the fast outbursts of XTE J1739−302 could be due to an instability of an accretion disk.

5.3.3 Intermittent accretion flow onto a neutron star

The shape of the flare of IGR J16479−4514 we observed with *INTEGRAL* and reported in Figure 5.10, consists of a fast rise and exponential decay, which could be explained with the magnetospheric instability mechanism

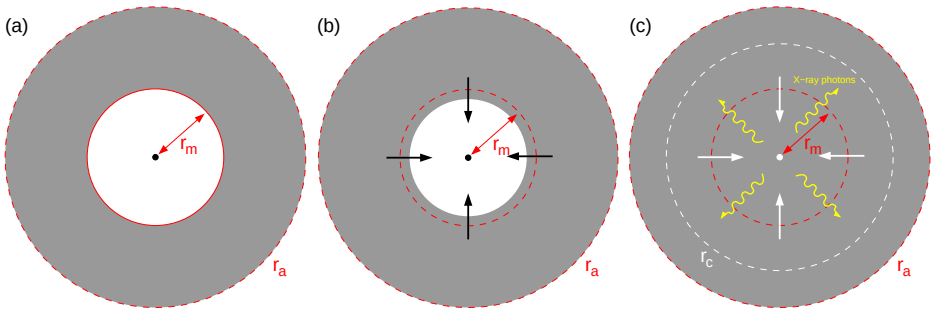

Figure 5.11: In the framework of the model of Lamb et al. (1977), the matter from the donor star falls toward a strongly magnetized neutron star. *(a):* the material is shock-heated when it reaches the magnetospheric radius. If its temperature is greater than a critic value, the magnetosphere behaves like a close gate, and an atmosphere is set-up outside. *(b):* when the gas at the base of the atmosphere has cooled sufficiently because of bremsstrahlung processes, the gate opens, and the plasma begins to fall. *(c):* the accretion of the atmosphere leads to a strong emission of X-ray photons, which cools the matter inside a radius r_c by means of Compton processes and extends the duration of the flare.

proposed by Lamb et al. (1977) to explain type II X−ray bursts. All equations in this section are taken from these authors. In the framework of a spherically symmetric accretion flow onto a neutron star, and under particular conditions of X−ray luminosity and temperature of the accreting matter, the magnetospheric surface behaves as a gate which controls the flow towards the stellar surface (see Figure 5.11). When the gate is closed, a magnetospheric cavity is formed, and a reservoir of matter is accumulated on the top of the neutron star magnetosphere, leading to low X−ray luminosities. When this matter has cooled sufficiently (because of electron−ion bremsstrahlung, which is the dominant cooling mechanism when the gate is closed), the plasma enters the magnetosphere via Rayleigh−Taylor instability, and the accretion onto the neutron star leads to a flaring behaviour. Lamb et al. (1977) found a critical luminosity

$$L_{\rm crit} = 2 \times 10^{36} |1 - T_{\rm r}/T_{\rm c}|^{7/8} \mu_{30}^{1/4} \left(\frac{M}{M_\odot} \right)^{1/2} R_6^{-1/8} {\rm erg\ s^{-1}} \qquad (5.21)$$

where $T_{\rm r}$ is the temperature of radiation, $T_{\rm c} \approx 10^9$ K, μ_{30} is the stellar magnetic moment in units of 10^{30} Gauss cm^3, M is the mass of the neutron star and R_6 is the radius of the neutron star in units of 10^6 cm. If the flare luminosity is greater than the critical luminosity (Equation 5.21), the Compton cooling dominates the bremsstrahlung cooling at $R_{\rm m}$, thus the magnetosphere gate is open for longer time and the flare is prolonged (Lamb et al. 1977).

The flare reported in Figure 5.10 has a peak luminosity of $\approx 3\times10^{37}$ erg s^{-1}, which is greater than the critical luminosity $L_{\rm crit} \approx 2.4 \times 10^{36}$ erg s^{-1} (if $T_{\rm r} < 10^9$ K).

Assuming $T_{\rm r} \approx 10^8$ K, we found that, because of Compton processes, beyond the radius $r_{\rm c} \approx 2.2 \times 10^{10}$ cm at which the free-fall temperature equals the temperature of radiation, the X−rays emitted by the neutron star heat the plasma[3] (see formula [31] in Lamb et al. 1977).

If the heating time scale is less than the flow time scale[4], the flow is choked at $R_{\rm m}$, and we expect for the flare a time duration given by:

$$\Delta t_{\rm max} \approx 125 \left(\frac{T_{\rm r}}{10^8 K}\right)^{-3/2} \left(\frac{M}{M_\odot}\right) \ {\rm s} \qquad (5.23)$$

which results into $\Delta t_{\rm max} \approx 175$ s assuming $T_{\rm r} = 10^8$ K and $M = 1.4 M_\odot$. This duration is not in agreement with that observed in Figure 5.10. However, if we assume $T_{\rm r} \approx 2 \times 10^7$ K, the heating time scale is less than the flow timescale at distances $\gg r_{\rm c}$. The condition (5.22) is no longer valid ($L_{\rm x} \lesssim L_{\rm choke} \approx 4 \times 10^{37}$ erg s^{-1}), thus the flow is choked at a radius $r'_{\rm c} > r_{\rm c}$. In this case the expected burst duration is given by:

$$\Delta t'_{\rm max} \approx 210 L_{37}^{-3} \left(\frac{T_{\rm r}}{10^8 K}\right)^{-3} \left(\frac{M}{M_\odot}\right)^{4} \ {\rm s} \approx 4900 \ {\rm s} \qquad (5.24)$$

(assuming $T_{\rm r} = 2 \times 10^7$ K, $M = 1.4 M_\odot$ and $L_{\rm x} = 3 \times 10^{37}$ erg s^{-1}). The assumption $T_{\rm r} = 2\times10^7$ K is in agreement with the temperature of radiation observed in some SFXTs (see e.g. Sidoli et al. 2007). In the framework described by Lamb et al. (1977), the exponential decay in this kind of flares is described by the law $L(t) \propto t^{1-2\alpha/3}$, with $\alpha \gtrsim 3/2$. From the fit of the exponential decay of the flare observed by *INTEGRAL* (Figure 5.10) we found $\alpha \approx 1.55$, thus in agreement with the value predicted by Lamb et al. (1977).

We point out that if $L_{\rm x} > L_{\rm crit}$, $T_{\rm r} < T_{\rm c}$ at $R_{\rm m}$, and if the accretion radius is lower than $r_{\rm c}$, the X−ray source is persistent with high luminosity (see Elsner & Lamb 1977). In fact, if $R_{\rm a} < r_{\rm c}$, Compton processes cool the matter up to a distance $r_{\rm c}$ but heat matter outside $r_{\rm c}$. If $R_{\rm a} < r_{\rm c}$, the matter

[3]The material accreting onto a neutron star is decelerated by the magnetic field, hence it is shock-heated to a temperature $T_{\rm s} \approx 3/16 T_{\rm ff}(R_{\rm m})$, where $T_{\rm ff}(r) \propto 1/r$ is the proton free-fall temperature. Since the temperature of radiation is roughly constant for every r, below a radius $r_{\rm c}$ the gas is cooled by Compton interaction ($T_{\rm r} < T_{\rm gas}$); outside $r_{\rm c}$ we have $T_{\rm r} > T_{\rm gas}$, thus the gas is heated by Compton processes.

[4]The condition for which the heating time scale is less than the flow time scale is expressed by:

$$L_{\rm x} \gg L_{\rm choke} = 1.2 \times 10^{37} \left(\frac{T_{\rm r}}{10^8 K}\right)^{-1/2} \left(\frac{M}{M_\odot}\right) \ {\rm erg \ s^{-1}} \ . \qquad (5.22)$$

This condition is respected if $T_{\rm r} = 10^8$ K, $M = 1.4 M_\odot$, $L_{\rm x} = 3 \times 10^{37}$ erg s^{-1}.

Table 5.8: Total exposure time $T_{\rm exp}$, number of outbursts, and outburst rates of the sample of sources considered.

Source	$T_{\rm exp}$ (d)	Number of outbursts	Rate ($\rm d^{-1}$)
Confirmed			
IGR J16465-4507	110.25	2	0.018
IGR J16479-4514	115.74	38	0.33
XTE J1739-302	260.42	18	0.069
IGR J17544-2619	259.92	14	0.054
SAX J1818.6-1703	179.45	11	0.061
AX J1841.0-0536	83.23	4	0.048
IGR J18483-0311	84.61	13	0.15
Candidates			
IGR J16195-4945	105.22	3	0.029
IGR J16207-5129	101.67	9	0.089
IGR J16418-4532	112.87	23	0.204
IGR J17407-2808	234.75	3	0.013
XTE J1743-363	232.04	7	0.030
AX J1820.5-1434	120.95	2	0.017
AX J1845.0-0433	77.85	7	0.090

is supplied at a sufficient rate and at a radius interior to $r_{\rm c}$: in this case the burst could last indefinitely.

In our case $R_{\rm a} \approx 1.8 \times 10^{11}$ cm and $r_{\rm c} \approx 2.2 \times 10^{10}$ cm (if $T_{\rm r} = 10^8$ K) or $r_{\rm c} \approx 1.1 \times 10^{11}$ cm (if $T_{\rm r} = 2 \times 10^7$ K). Thus, what makes IGR J16479−4514 (and probably other SFXTs) intermittent with respect to the other persistent HMXBs could be the X−ray photoionization which reduces the wind velocity, increasing the accretion radius with respect to $r_{\rm c}$.

5.4 The expected number of SFXTs in the Galaxy

The *INTEGRAL* data analysis of 14 SFXTs we have performed (Section 5.1; Ducci et al. 2010), enable us to place constraints on the total population number of SFXTs in our Galaxy. With *INTEGRAL* we detected 14 SFXTs within the Galactic longitudes $-35 \lesssim l \lesssim 41.7$. Using the distances inferred from the optical counterparts (when available), we found that the average luminosity of the outbursts is $\bar{L}_{\rm x} = 5 \times 10^{36}$ erg $\rm s^{-1}$ $(18 - 40$ keV). The minimum flux that a SFXT must have in order to be detected by IBIS/ISGRI $(18 - 40$ keV) with a significance $> 5\sigma$ is $F_{\rm min} \simeq 2 \times 10^{-10}$ erg $\rm cm^{-2}$ $\rm s^{-1}$. Thus, only SFXTs within $R_{\rm loc} \simeq 14$ kpc from the Sun can be detected by IBIS/ISGRI. As shown in Figure 5.12, we have observed a small region of

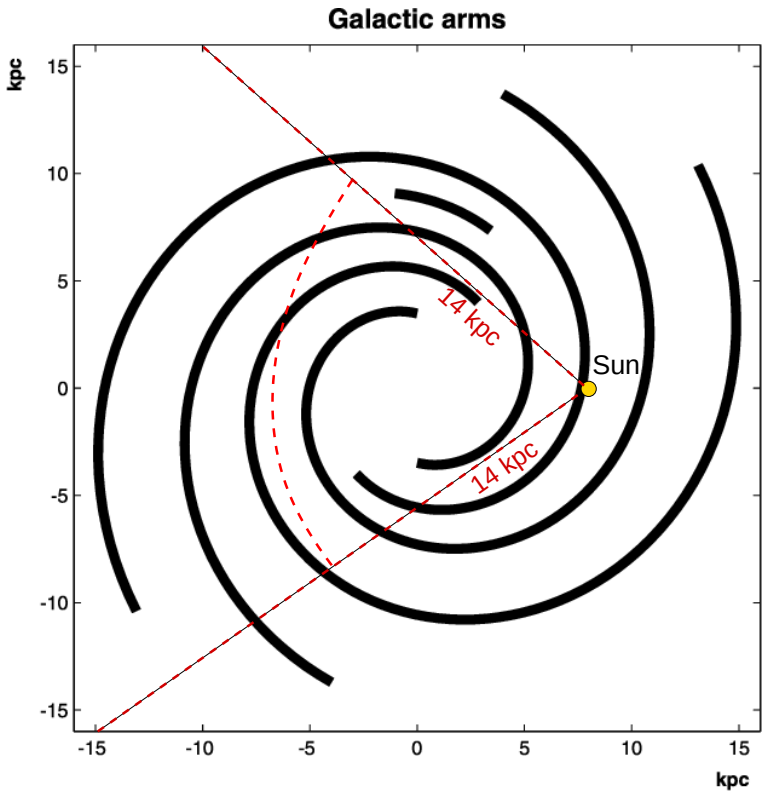

Figure 5.12: Schematic representation for the Galactic plane, viewed from above the north Galactic pole. The black lines are the model from Wainscoat et al. (1992), with the Sun located at 8.5 kpc from the center. Red lines define the region of the Galaxy we have observed with *INTEGRAL*, where the angle is ($\sim 76.7°$) and $R_{\rm loc} = 14$ kpc is the maximum distance for a SFXT in order to be observed with IBIS/ISGRI.

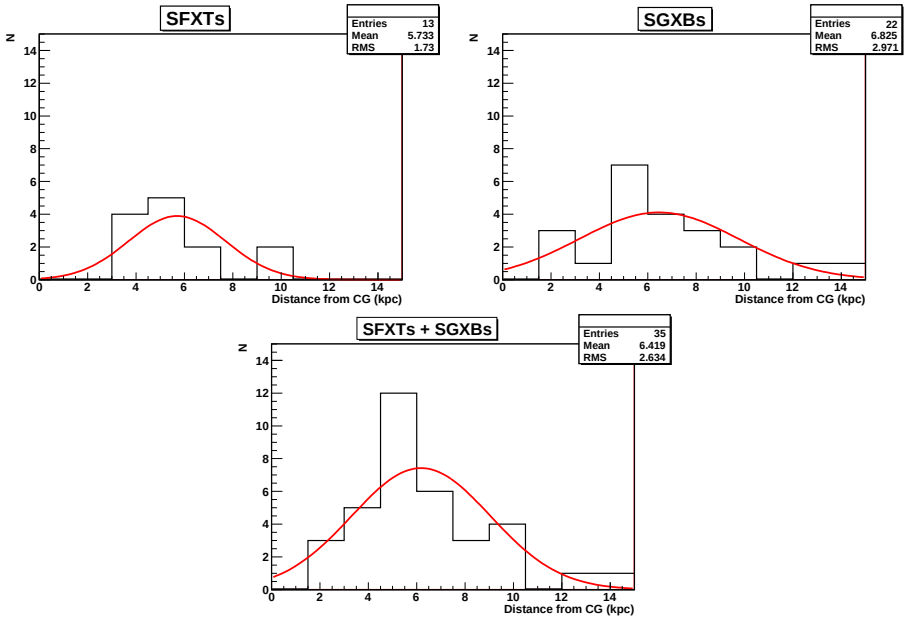

Figure 5.13: Distributions of galactocentric distances of SFXTs (top, left panel), SGXBs (top, right panel), SFXTs + SGXBs (bottom panel), fitted with a gaussian distribution (red line) using the binned likelihood test, because of the low statistics.

the Galactic plane, defined by the angle $\theta \sim 76.7^{\circ}$ and the radius $R_{\rm loc}$.

In order to estimate the number of SFXTs in the Galaxy, we need to know the fraction of the SFXTs population in the region of the Galaxy that we surveyed with *INTEGRAL*. In Figure 5.13 we report the distributions of galactocentric distances of SFXTs, SGXBs, and SFXTs+SGXBs. We obtained the position and distance of each source in our sample from the SIMBAD server, the Liu et al. (2006) catalogue, and the *INTEGRAL* sources listed in `http://irfu.cea.fr/Sap/IGR-Sources/`. We fitted each distribution with a gaussian, adopting a binned likelihood test because of the low statistics. With a Kolmogorov-Smirnov test we found that the SFXTs and SGXBs distributions are statistically compatible with a probability of $\sim 23\%$. This result can be explained with the hypothesis that SFXTs and SGXBs follow the distribution of young OB massive star-forming complexes (Russeil 2003). Thus we consider for our purpose the galactocentric distribution of SFXTs+SGXBs. We report in Figure 5.14 a 3D representation of the shape of this distribution. This Figure shows that HMXBs with supergiant are underabundant in the central few kpc and peaks at the spiral arms, so we have calculated the fraction f of SFXTs in the area covered by our observations (Figure 5.12) adopting a Monte Carlo integration method,

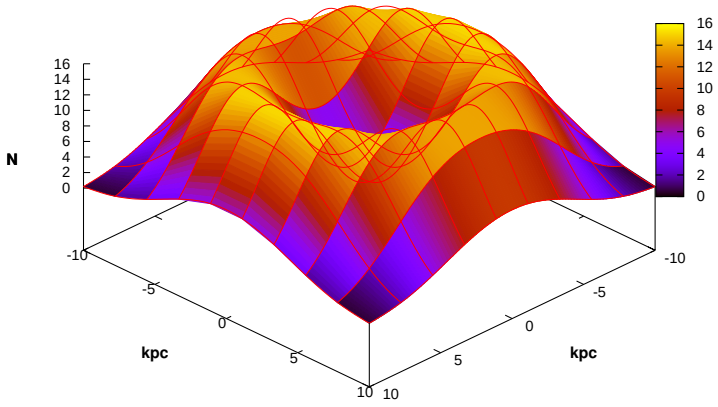

Figure 5.14: Schematic representation of the SFXTs distributions in our Galaxy.

and f resulted to be:

$$f = \frac{n_{\rm loc}}{n} = 0.4513 \ .$$

This means that we have observed a region containing about 45% of the total population of SFXTs in our Galaxy.

Given f, we can calculate the expected number of SFXTs in our Galaxy, and we obtained this value with a method similar to that used by Muno et al. (2008) to estimate the number of Galactic magnetars.

We assumed that, for a monitoring period $T_{\rm m}$, a new Galactic X-ray source is identified as candidate SFXT if it produces one or multiple bright flares ($\bar{L}_{\rm x} = 5 \times 10^{36}$ erg s^{-1}) with duration of a few hours.

We considered the recurrence timescale r of the outbursts of the 14 SFXTs, which is given by:

$$r = \frac{N_{\rm out}}{T_{\rm m}} \ ,$$

where $N_{\rm out}$ is the number of outbursts emitted by the source in a monitoring time $T_{\rm m}$ (see Table 5.8).

We have to calculate the probability that a number of outbursts occurrs in a fixed period of time, if these outbursts occur with a known average rate r indipendently of the time since the last event. This probability is expressed by the Poisson distribution. Given the outburst rate r of the considered source, the expected number of occurrences during the monitoring time $T_{\rm m}$ is:

$$\mu = rT_{\rm m} \ .$$

Then, the probability that there are ν occurrences is:

$$p_\mu(\nu) = \frac{\mu^\nu e^{-\mu}}{\nu!} \tag{5.25}$$

From Equation (5.25) we have that the chance that any given source is not detected ($\nu = 0$) is:

$$p_\mu(0) = e^{-\mu} = e^{-rT_\mathrm{m}} \ .$$

Thus, the chance that any given source is detected is $1 - p_\mu(0)$:

$$prob = 1 - e^{-rT_\mathrm{m}} \ . \tag{5.26}$$

We assumed a population of n_loc SFXTs in the region of the Galaxy observed with *INTEGRAL*, and m is the number of SFXTs observed during our *INTEGRAL* observations. Thus, given a population of n_loc sources, the probability to detect m sources within a monitoring time T_m is given by the binomial distribution:

$$prob(m|n_\mathrm{loc}, rT_\mathrm{m}) = (1 - e^{-rT_\mathrm{m}})^m (e^{-rT_\mathrm{m}})^{(n_\mathrm{loc}-m)} \frac{n_\mathrm{loc}!}{m!(n_\mathrm{loc} - m)!} \ . \tag{5.27}$$

The probability that n_loc SFXTs of a total population n would lie in the fraction of the Galaxy we have surveyed is:

$$prob(n_\mathrm{loc}|n, f) = f^{n_\mathrm{loc}} (1 - f)^{(n-n_\mathrm{loc})} \frac{n!}{n_\mathrm{loc}!(n - n_\mathrm{loc})!} \tag{5.28}$$

where we used the fraction f previously obtained. Then, the probability that m SFXTs are found is the joint probability that n_loc of n SFXTs lie in the observed region of the Galaxy and that m out of n_loc are detected during a monitoring time T_m:

$$\begin{aligned} prob(m|rT_\mathrm{m}, f, n) = & \sum_{n_\mathrm{loc}=m}^{\mathrm{n}} (1 - e^{-rT_\mathrm{m}})^m (e^{-rT_\mathrm{m}})^{(n_\mathrm{loc}-m)} \frac{n_\mathrm{loc}!}{m!(n_\mathrm{loc} - m)!} \times \\ & \times \quad f^{n_\mathrm{loc}} (1 - f)^{(n-n_\mathrm{loc})} \frac{n!}{n_\mathrm{loc}!(n - n_\mathrm{loc})!} \ . \end{aligned} \tag{5.29}$$

Bayesian inference allows us to calculate the expected population of sources from which a set of data has been extracted. We are interested in n, thus we invert Equation (5.29) using the Bayes' theorem[5] given the number of SFXTs m found in a fraction f of the Galaxy. The probability $prob(n|m, rT_\mathrm{m}, f)$ is given by:

$$prob(n|m, rT_\mathrm{m}, f) = \frac{prob(m|rT_\mathrm{m}, f, n)}{\sum_{n=m}^{\infty} prob(m|rT_\mathrm{m}, f, n)} \ . \tag{5.30}$$

[5] see e.g. the review of Bayesian methods in astrophysics of Trotta (2008).

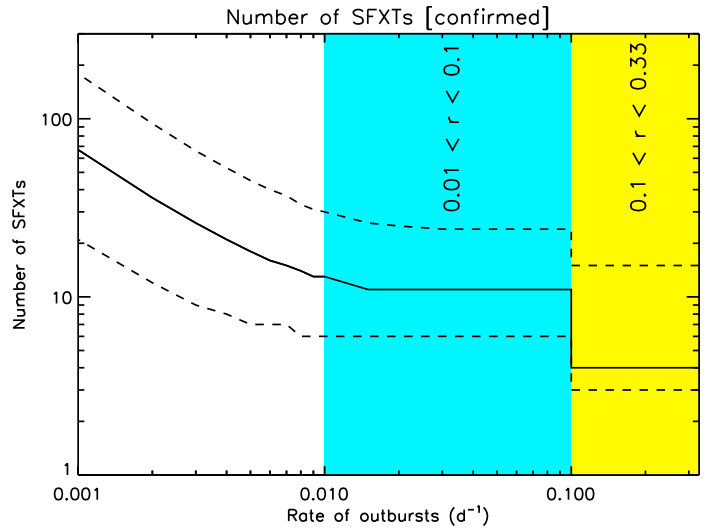

Figure 5.15: Estimated number of SFXTs in our Galaxy, as a function of the outburst rate r. We based our calculation of n on the confirmed SFXTs. The solid line shows the most likely number, the dashed lines show the 99% confidence limit on that number.

We used Equation (5.30) to obtain the number of SFXTs in the region of the Galaxy observed with *INTEGRAL*. We calculate this number starting from two different sets of sources:

a) SFXTs confirmed;

b) SFXTs confirmed + candidates.

a) From Table 5.8 we have that the outburst rate is strongly variable from source to source, ranging from $r = 0.018$ of IGR J16465-4507 to $r = 0.33$ of IGR J16479-4514. In order to apply the Equation (5.30) to SFXTs with homogeneous properties (i.e. similar r), we divided the sample of confirmed SFXTs in two sub-sets:

1. SFXTs with $r \geq 0.1$ d^{-1} $\Rightarrow m_1 = 2$;
2. SFXTs with $r \leq 0.1$ d^{-1} $\Rightarrow m_2 = 5$;

For each sub-set we assume that the monitoring period is given by:

$$T_{\rm m} = \frac{\sum_{\rm i=1}^{\rm m} T_{\rm exp}}{m} \ ,$$

therefore, $T_{\rm m_1} = 100.175$ d and $T_{\rm m_2} = 178.654$ d.

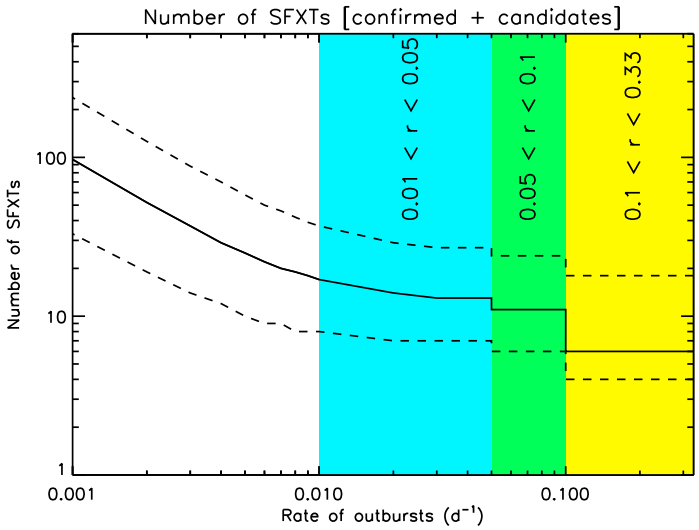

Figure 5.16: Estimated number of SFXTs in our Galaxy, as a function of the outburst rate r. We based our calculation of n on the confirmed and candidates SFXTs. The solid line shows the most likely number, the dashed lines show the 99% confidence limit on that number.

In Figure 5.15 we plot for a range of r the most likely value for the number n of SFXTs (solid line), and the 99% confidence limit for n (dashed lines).

If the total population of SFXTs has outbursts rates $r \geq 0.01$, from Figure 5.15 we have that there could be 17^{+28}_{-8} SFXTs.

b) Similarly to Figure 5.15, Figure 5.16 refers to the expected SFXTs in the Galaxy taking into account confirmed and candidates SFXTs. In this case we divide our sample of sources in three sub-sets:

1. $r \geq 0.1$ d^{-1} $\Rightarrow m_1 = 3$ and $T_{\rm m_1} = 104.407$ d;
2. $0.05 \leq r < 0.1$ d^{-1} $\Rightarrow m_2 = 5$ and $T_{\rm m_2} = 175.862$ d;
3. $0.01 \leq r < 0.05$ d^{-1} $\Rightarrow m_3 = 6$ and $T_{\rm m_3} = 147.74$ d.

In this case, for a rate $r \geq 0.01$, we derive a number of 34^{+45}_{-16} SFXTs.

We have previously pointed out that the outburst rate in SFXTs is strongly variable from source to source. Thus, it is possible that there are other SFXTs still undiscovered with an outburst rate of $r \simeq 0.006$ (similar to the outburst rate of IGR J11215-5952, for which we expect an outburst every $P_{\rm orb} \approx 165$ d) or less. In this case, the expected number of SFXTs can be very large: for example, for $r \geq 0.001$ there could be up to 114^{+166}_{-71} SFXTs.

Assuming that SFXTs have an average X-ray luminosity in the 2-10 keV energy band of $\bar{L}_{\rm x} \approx 10^{33} - 10^{34}$ erg s^{-1} (Sidoli et al. 2008; Romano et al. 2010), from the estimated number of SFXTs we found that the total X-ray luminosity of SFXTs in the Galaxy is $L_{\rm tot}^{\rm SFXTs} \approx 4 \times 10^{34} - 4 \times 10^{36}$ erg s^{-1} (2-10 keV). We point out that, because of the X-ray variability of SFXTs, an outburst can increase the total luminosity of the Galactic population of SFXTs by an order of magnitude. $L_{\rm tot}^{\rm SFXTs}$ can be neglected with respect to the total X-ray luminosity of HMXBs in normal galaxies such as the Milky Way or M 31, which is of the order of $2 - 3 \times 10^{38}$ erg s^{-1} (2-10 keV; Grimm et al. 2002; Makishima et al. 1989).

5.5 Conclusions

Up to now three accretion mechanisms have been proposed to explain the X−ray flares of SFXTs.

Here we propose other mechanisms to explain the observed X−ray behaviour of IGR J16479−4514, IGR J17544−2619 and XTE J1739−302: the effect of X−ray photoionization onto accretion (both in direct accretion and centrifugal inhibition of accretion) in the framework of the Ho & Arons (1987) model; the accretion disk instability of Taam et al. (1988), and the intermittent accretion flow of Lamb et al. (1977).

We have shown that the X−ray photoionization reduces the mass loss rate and the wind velocity along the trajectory compact object−OB supergiant in comparison with the undisturbed case (section 5.3.1). Their simultaneous reduction leads to X−ray luminosities in agreement with those observed during the flaring activity; moreover, a lower $v_{\rm w}$ allows the formation of transient accretion disks from the capture of angular momentum, able to reproduce some kind of quasi−periodic recurrent flares observed in SFXTs.

We found in our analysis of *INTEGRAL* data that some flares show a peculiar shape, characterized by a sharp rise and an exponential decay (Figure 5.10). We found that this shape is well explained assuming the model of Lamb et al. (1977), based on the Rayleigh-Taylor instability, although this model was proposed to try to explain type II bursts.

Therefore, we conclude that in SFXTs with large orbital periods ($P_{\rm orb} \gtrsim$ 15 d; e.g.: IGR J18483−0311, SAX J1818.6−1703, IGR J11215-5952) the effects of X−ray photoionization onto accretion mechanism can be neglected. In SFXTs with smaller orbital periods ($P_{\rm orb} \lesssim 15$ d; e.g.: IGR J16479−4514, IGR J17544−2619) we suggest that part of the X−ray variability observed is due to the X−ray photoionization and consequently to the accretion disk instability. We are still not able to establish which mechanism dominates in SFXTs with smaller orbital periods. Moreover, we point out that different accretion mechanisms could be at work in a single SFXT, in the case of

orbits with high eccentricities.

Chapter 6

Study of IGR J16418-4532

6.1 Introduction

In Chapter 5 we reported the discovery of several new outbursts from the candidate SFXT IGR J16418-4532. These new observations allowed us to gain more information about this source, which is still poorly known.

IGR J16418-4532 is an HMXB discovered in 2003 February by the *INTEGRAL* satellite (Tomsick et al. 2004). This source is composed of a neutron star, with a spin period of 1246 ± 100 s (Walter et al. 2006), and an OB star (Chaty et al. 2008). Corbet et al. (2006) found the orbital period using the *Swift*/BAT and *RXTE*/ASM data and obtained the values 3.753 ± 0.004 d and 3.7389 ± 0.0004 d, respectively. Corbet et al. (2006) explained the discrepance between the two values with an underestimation of the error bars because of the presence of non-periodic modulation in the light curves and because the modulation is probably not-sinusoidal. Levine et al. (2010) obtained for this source an orbital period of $P_{\rm orb} = 3.73886 \pm 0.0014$ d using a larger set of *RXTE*/ASM data (50133−55224 MJD).

Rahoui et al. (2008) determined a spectral type O8.5 fitting the Spectral Energy Distribution (SED), but still uncertainties in the main sequence, giant or supergiant remained (see Table 6.1).

The *XMM-Newton* spectrum showed that this source is highly absorbed, with a column density of $\sim 10^{23}$ cm^{-2} (Walter et al. 2006). Sguera et al. (2006) proposed a fast X-ray transient nature, from the observation of a fast outburst (duration of ~ 1 hr) detected by IBIS/ISGRI on 2004 February 26.

Here we report the spectral and timing analysis of IGR J16418-4532 using *INTEGRAL* and *Swift*/BAT observations.

Table 6.1: Distances of IGR J16418-4532 derived by Rahoui et al. (2008) assuming different spectral classes.

Spectral Type	Distance (kpc)		
O8.5	V	III	I
	4.9	8.3	13

6.2 Observations and results

6.2.1 *Swift*/BAT results

We have used data from the Burst Alert Telescope (BAT; Barthelmy et al. 2005), aboard the *Swift* observatory (Gehrels et al. 2004), which was launched in 2004. BAT is a coded mask telescope with a wide field of view ($120^\circ \times 90^\circ$ partially coded field of view) operating in the $15 - 200$ keV energy band. Moreover, *Swift* carries the X-Ray Telescope (XRT; Burrows et al. 2005) operating in the $0.2 - 10$ keV energy band, and the UltraViolet/Optical Telescope (UVOT; Roming et al. 2005) operating in the $170 - 600$ nm.

We searched for the orbital period using the 15-50 keV *Swift*/BAT lightcurve of IGR J16418-4532 provided by the *Swift*/BAT team (Krimm et al. 2006)[1]. The data analysed here span the time between 53413 and 55432 MJD. We excluded bad quality points (quality 1 and 2), which are points with extremely large errors (more than four times the average statistical error) and large ($> 10\sigma$) negative fluctuations due to systematic errors. We corrected the lightcurve for the Solar System barycentre using the EARTH2SUN tool of the HEASARC software package FTOOLS ver. 6.4.1. Adopting the Lomb-Scargle method (Lomb 1976; Scargle 1982; Figure 6.1, left panel), we found a periodicity at ~ 3.7383 d at above 99.9% significance (the false alarm probability is 1.6×10^{-9}). Using an epoch-folding method, our search resulted in a χ^2 peak at $P_{\rm orb} = 3.7381 \pm 0.0002$ days. Figure 6.1 (right panel) shows the χ^2 peak fitted with a gaussian corresponding to the period found. This period is in agreement with that determined by Levine et al. (2010) using *RXTE*/ASM data.

Figure 6.2 shows the *Swift*/BAT lightcurve folded on the orbital period. The folded lightcurve shows a significant orbital modulation, probably due to an eclipse at the orbital phase ~ 0, or due to an orbital modulation produced by an eccentric orbit, eventually with the onset of the centrifugal inhibition of accretion at apastron, where the wind is less dense and has a larger velocity than at periastron because of the continuity Equation (1.14) and the β-velocity law (Equation 1.28).

[1] We downloaded the lightcurve from:
`http://heasarc.nasa.gov/docs/swift/results/transients/`.

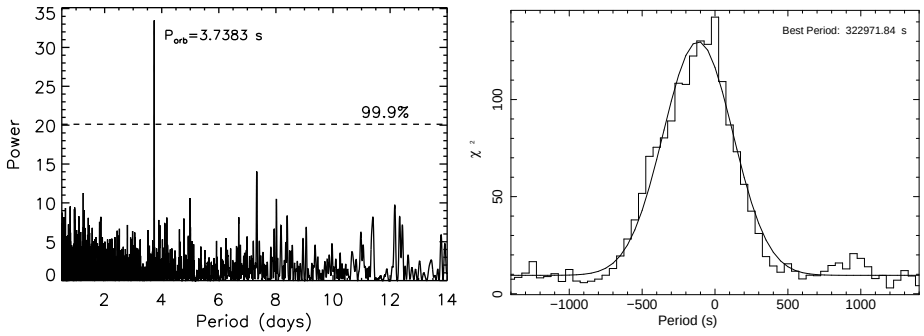

Figure 6.1: *Left panel:* Lomb-Scargle periodogram for the 15-50 keV *Swift*/BAT lightcurve of IGR J16418-4532. The peak in the periodogram corresponds to $P_{\rm orb} = 3.7383$ d. *Right panel:* distribution of χ^2 versus trial period using the 15-50 keV *Swift*/BAT data. The distribution peaks at $P_{\rm orb} = 3.7381 \pm 0.0002$ d.

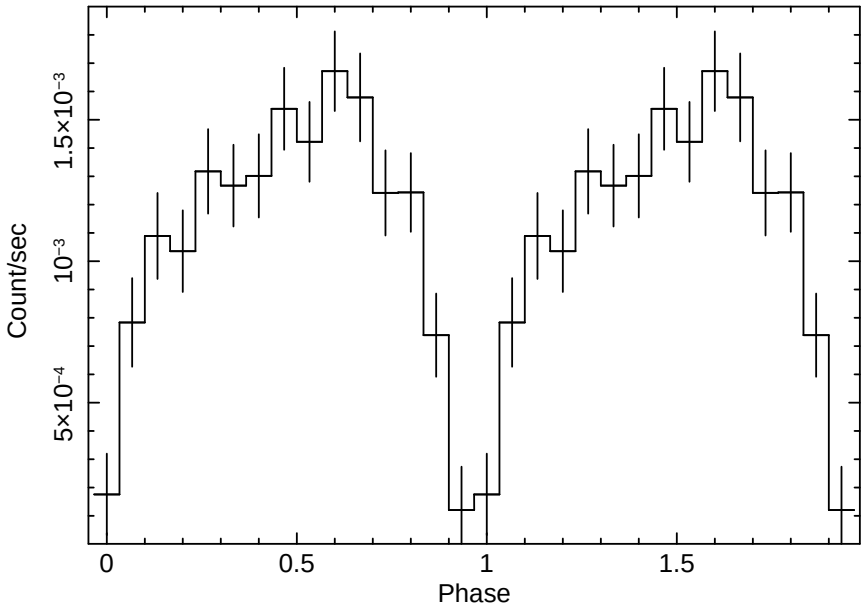

Figure 6.2: *Swift*/BAT lightcurve (15-50 keV) of IGR J16418-4532 folded with a period $P_{\rm orb} = 3.7381 \pm 0.0002$ d (2σ) and at $t_0 = 51544$ MJD.

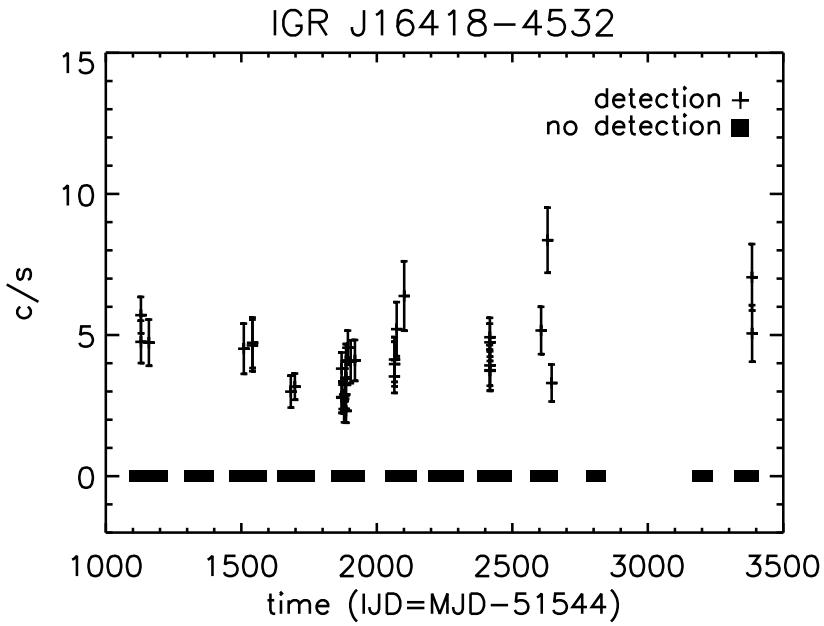

Figure 6.3: IBIS/ISGRI lightcurves of IGR J16418−4532 ($20-40$ keV). A binned time corresponding to the ScW duration (~ 2000 s) has been used.

6.2.2 INTEGRAL results

We analyzed all the public and our private IBIS/ISGRI and JEM-X data (between 2003 and 2009) in the 18−60 keV energy band where the source was in the IBIS/ISGRI field of view. We use the Off-line Scientific Analysis package OSA 8.0 (Goldwurm et al. 2003). This resulted in 3790 ScWs, corresponding to a total exposure time of 112.87 d.

We extracted the IBIS/ISGRI lightcurve at ScW resolution, and we considered only the pointings with significance $> 5\sigma$ (see Figure 6.3).

For these pointings we extracted the IBIS/ISGRI and, where available, JEM-X spectra. We performed the spectral analysis with XSPEC 11.3, and we added a 2% systematic error to both IBIS/ISGRI and JEM-X data sets.

We adopted two simple models to fit the spectra: a bremsstrahlung and a power law. The best fit spectral parameters are reported in Table 5.3 for the newly discovered outbursts.

No evidence of a spectral variability has been found. Thus, we extracted an average JEM-X+IBIS/ISGRI outburst spectrum summing together all the data (Figure 6.4). The best fit to the average spectrum is an absorbed power law with a high-energy cutoff with the following parameters: a photon index $\Gamma = 1.87^{+0.16}_{-0.16}$, a cutoff energy $E_{\rm c} = 36.2^{+2.7}_{-3.1}$ keV, an e-folding energy $E_{\rm F} = 5.8^{+3.8}_{-3.0}$ keV modified by photoelectric absorption at lower energies

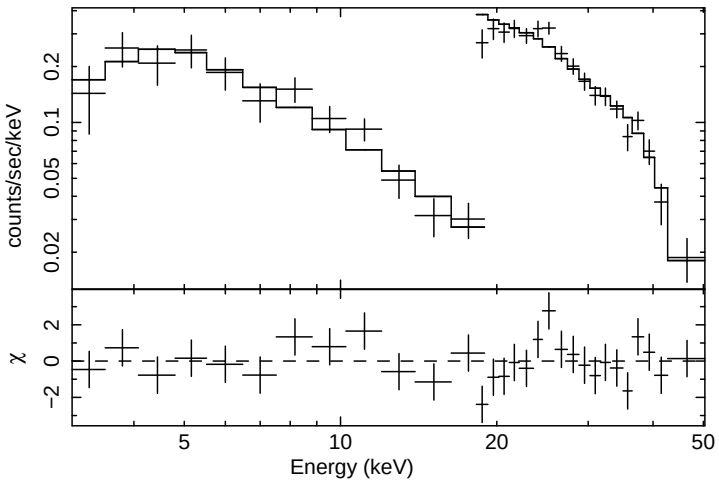

Figure 6.4: Joint JEM-X plus IBIS/ISGRI counts spectra, together with residuals in units of standard deviations for IGR J16418−4532.

($N_{\rm H}$) of $6.6^{+6.1}_{-4.8}$ 10^{22} cm^{-2} ($\chi^2_\nu = 1.29$, d.o.f.=25).

We searched for the IGR J16418-4532 spin period by using the Lomb-Scargle periodogram (Lomb 1976; Scargle 1982) within the period range 100−2000 s. We found a periodicity at 1213.5 s in the IBIS/ISGRI data (15−40 keV) of the *INTEGRAL* revolution 468 (see Figure 6.5 and Table 6.2), with a false alarm probability of 0.001275. This spin period is in agreement (within the measurement uncertainties) with the earlier measurement of Walter et al. (2006) obtained with *XMM-Newton*. Since the probability to have a spurious detection of a previously known period is less than the probability to have spurious detection in a blind search (Wen et al. 2006), the probability of chance detection in our case is $0.001275/N_{\rm f} = 1.38436 \times 10^{-6}$, where $N_{\rm f} = 921$ is the number of independent period searched, that we have calculated with the formula:

$$N_{\rm f} = -6.362 + 1.193N_0 + 0.00098N_0^2$$

of Horne & Baliunas (1986), where $N_0 = 539$ is the number of points in the data set. We evaluated the uncertainty on the spin period $\sigma_{\rm P}$ following the Horne & Baliunas (1986) formula:

$$\sigma_{\rm P} = \frac{3\pi\sigma_{\rm N}}{2\sqrt{N}\Delta T A}\frac{2\pi}{\omega^2} \tag{6.1}$$

where ΔT is the total length of the data set, N is the number of data points, and $\sigma^2_{\rm N}$ is the variance of the noise after subtracting the sinusoidal signal:

$$y(t) = A\sin(\omega t - \phi) + B\ . \tag{6.2}$$

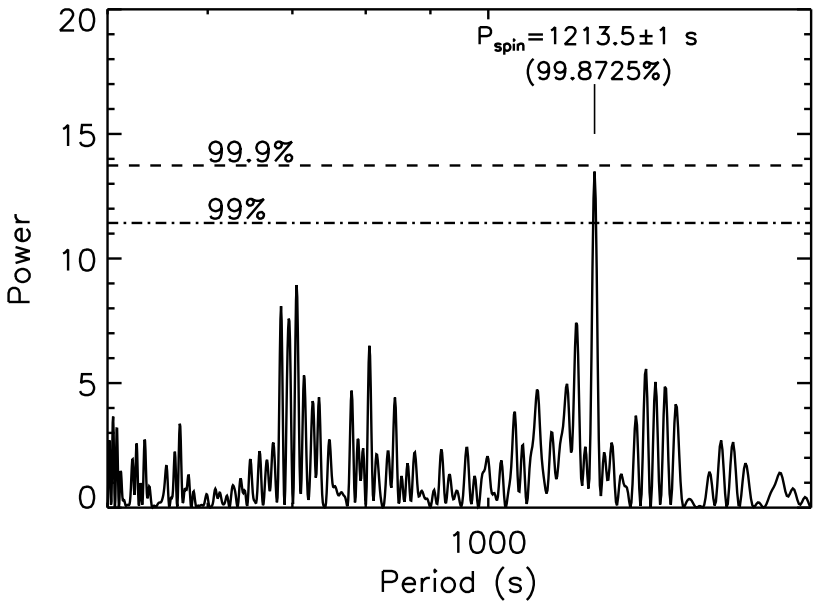

Figure 6.5: Lomb-Scargle periodogram for the $15-40$ keV IBIS/ISGRI lightcurve of IGR J16418-4532 (bin-time $\Delta t = 50$ s).

Table 6.2: *INTEGRAL* observations used to search the spin period with the Lomb-Scargle method (Figure 6.5).

ScW	Start Time (MJD)	End Time (MJD)
046800270010	53960.883	53960.918
046800300010	53960.992	53961.026
046800360010	53961.209	53961.243
046800370010	53961.245	53961.279
046800380010	53961.281	53961.316
046800490010	53961.697	53961.732
046800510010	53961.769	53961.804
046800520010	53961.805	53961.840
046800530010	53961.842	53961.876

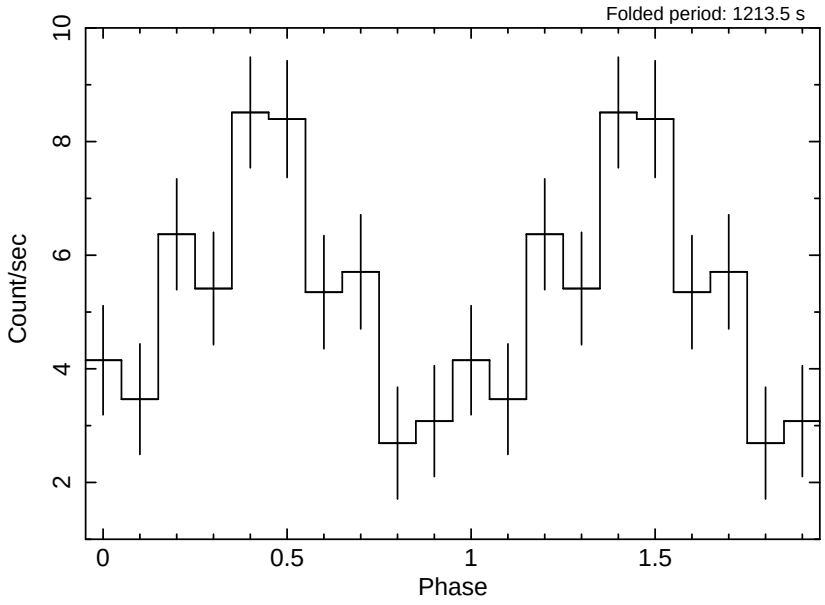

Figure 6.6: IBIS/ISGRI lightcurve ($15-40$ keV) of IGR J16418-4532 folded with a period of 1213.5 s.

From Equation (6.1) we obtained a period uncertainty of ≈ 1 s. We searched for spin period of this source also adopting epoch-folding techniques: with this method we found a spin period of $P_{\rm spin} = 1213.7 \pm 1$ s, in agreement with the spin period found with the Lomb-Scargle periodogram. Figure 6.6 shows the lightcurve of IGR J16418-4532 folded with a period of 1213.5 s.

6.3 Discussion

In order to estimate the time duration of the state with low flux at the orbital phase $\phi \sim 0$ (Figure 6.2), we re-extracted a IBIS/ISGRI lightcurve of IGR J16418-4532, where each point corresponds to the shortest time-interval where the source is detected above 5σ. We extracted the fluxes of this lightcurve from mosaics of contiguous ScWs. Figure 6.7 shows the most relevant lightcurves obtained for the aim described above. In Figure 6.7 IGR J16418-4532 displays a low level of X-ray luminosity at phase $\phi \approx 0$, with a duration $\Delta t \approx 0.505$ d (yellow region) corresponding to the low-luminosity level observed at the same phase in the folded lightcurve (Figure 6.2).

We investigated the possibility that the low flux at $\phi = 0$ is an eclipse. Assuming a circular orbit, we calculated the radius of the supergiant as a function of the inclination of the orbital angular momentum vector with respect to the line of sight to the Earth i, and for different values of the

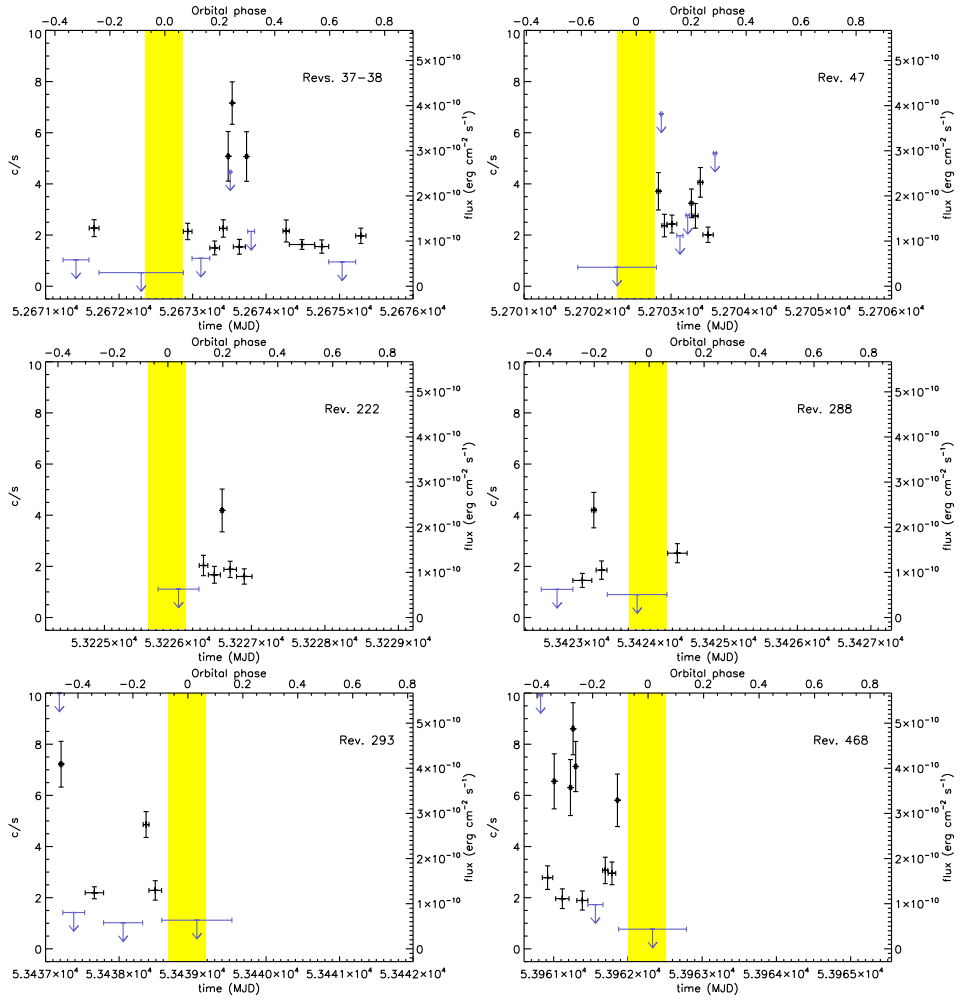

Figure 6.7: IBIS/ISGRI lightcurves of IGR J16418-4532 ($15-40$ keV). The time duration of the state with low flux at phase ~ 0 is indicated with a yellow stripe and results to be $\Delta t = 0.505$ d.

mass of the primary star; then we compared these results with the typical radii of O8.5 I, III, V stars.

The radius of the companion is related to the inclination i by:

$$R_{\mathrm{O8.5}} = a\sqrt{\cos^2 i + \sin^2 i \sin^2 \theta_{\mathrm{e}}} \tag{6.3}$$

(Rappaport & Joss 1983), where a is the semimajor axis (Kepler's third law):

$$a = \left[\frac{G(M_{\mathrm{O8.5}} + M_{\mathrm{NS}})P_{\mathrm{orb}}^2}{4\pi^2}\right]^{1/3} \tag{6.4}$$

and:

$$\theta_{\mathrm{e}} = \frac{2\pi t_{\mathrm{e}}}{P} \tag{6.5}$$

is the eclipse semiangle, where $t_{\mathrm{e}} = \Delta t/2$ is the half duration of the eclipse.

For the donor star we adopted masses and radii obtained by Martins et al. (2005) from a calibration of stellar parameters based on results of detailed spectroscopic analysis of individual O stars:

- O8.5V: $M_{\mathrm{O8.5}} = 18.8$ M$_\odot$; $R_{\mathrm{O8.5}} = 7.9$ R$_\odot$;
- O8.5III: $M_{\mathrm{O8.5}} = 23.68$ M$_\odot$; $R_{\mathrm{O8.5}} = 13.6$ R$_\odot$;
- O8.5I: $M_{\mathrm{O8.5}} = 31.54$ M$_\odot$; $R_{\mathrm{O8.5}} = 21.4$ R$_\odot$,

Then we assumed a neutron star mass $M_{\mathrm{NS}} = 1.4$ M$_\odot$ with radius $R_{\mathrm{NS}} = 10^6$ cm. From Equations (6.3), (6.4), and (6.5), we obtained the solutions reported in Figure 6.8 (solid lines). In Figure 6.8 we also compared the radii obtained for the companion star with the expected values (dashed lines). From this comparison we can exclude the hypothesis that the companion is a main sequence star. In the giant and supergiant cases, orbital inclinations $i_{\mathrm{O8.5III}} = 1.35$ and $i_{\mathrm{O8.5V}} = 0.97$ allows to explain the observed eclipse duration assuming the expected radius of the donor star.

Furthermore, it is possible to establish the nature of the donor star from a comparison between the observed and the expected X-ray luminosity of the neutron star. In fact, the accretion onto a neutron star from the wind of a supergiant or a main sequence/giant star produces different X-ray luminosities. The wind of a O8.5I star has mass loss rate of the order of $\dot{M} \approx 2 \times 10^{-6}$ M$_\odot$ yr^{-1} and the wind follows the β-velocity law (Equation 1.28) with a terminal velocity $v_\infty = 1800$ km s^{-1} and $\beta = 1$ (Vink et al. 2000). The wind of O8.5 V/III are usually composed by an equatorial component (circumstellar disk) denser and slower than the polar wind (see Section 1.3.4). The equatorial component is characterized by a density given by the Equation (1.33) with $\rho_0 = 10^{-11}$ g cm^{-3} and $n \approx 3.3$, and a radial velocity law given by the Equation (1.34) with $v_0 = 10 - 30$ km s^{-1}

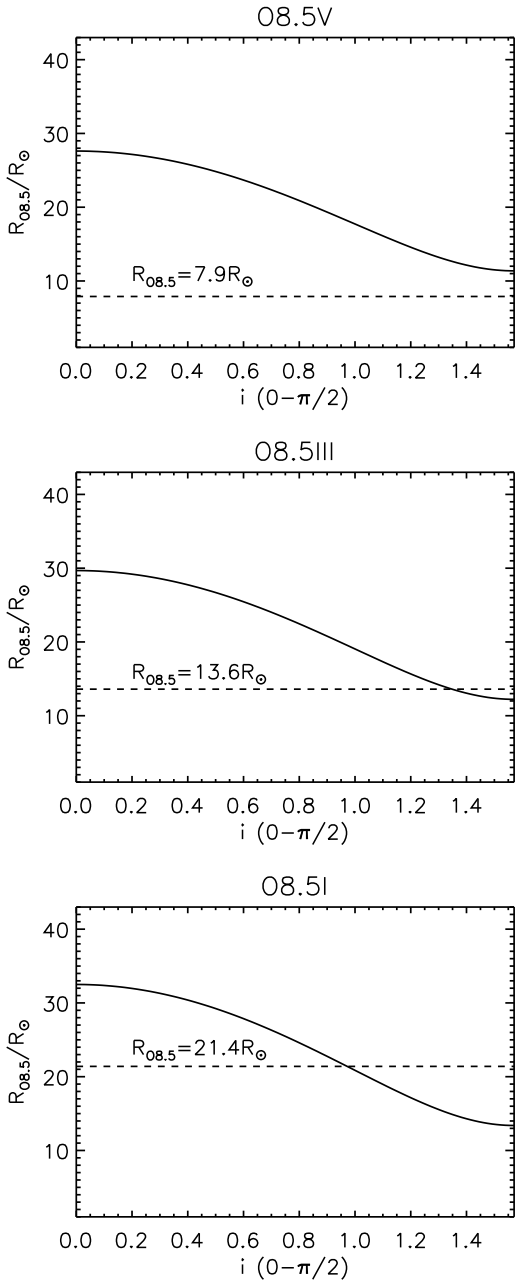

Figure 6.8: Radius of the donor star as a function of the binary inclination angle i, calculated for different values of the mass of the donor star. The solid lines are given by Equation (6.3), dashed lines are the radii of O8.5 V-III-I stars given by Martins et al. (2005).

and a rotational velocity given by the Equation (1.35) with $\alpha = 0.5$ (Keplerian disk) and $v_{\rm rot,*} \approx 150 - 300$ km s^{-1} (Waters et al. 1989). The polar wind is characterized by a terminal velocity $v_\infty = 600 - 2000$ km s^{-1} and $\dot{M} \approx 10^{-8} - 10^{-10}$ M$_\odot$ yr^{-1} (Waters et al. 1989). If the main sequence/giant star does not show the presence of a circumstellar disk (see e.g. Reig 2007), the wind is spherically symmetric with terminal velocity $v_\infty = 600 - 2000$ km s^{-1} and a mass loss rate $\dot{M} \approx 10^{-8} - 10^{-10}$ M$_\odot$ yr^{-1}.

Assuming that the donor star is a supergiant, for a circular orbit of the neutron star and considered the relative wind velocity of the neutron star with respect to the wind velocity, from Equations (1.16), (1.18), (1.28) we obtained a luminosity of $L_{\rm x} \approx 10^{36}$ erg s^{-1} (corresponding to a flux $F_{\rm x} \approx 1.5 \times 10^{-10}$ erg cm^{-2} s^{-1}, $d = 13$ kpc).

If the neutron star orbits around a main sequence/giant star, and accretes matter from the circumstellar disk, the expected luminosity is $L_{\rm x} \approx 10^{38}$ erg s^{-1} ($F_{\rm x} \approx 1 - 3 \times 10^{-8}$ erg cm^{-2} s^{-1}, $d = 4.9 - 8.3$ kpc).

If the equatorial component is not present, the neutron star accretes only from the polar wind; in this case the expected luminosity ranges from $\approx 3{\times}10^{33}$ erg s^{-1} to $\approx 2{\times}10^{35}$ erg s^{-1} ($10^{-12} \lesssim F_{\rm x} \lesssim 5{\times}10^{-11}$ erg cm^{-2} s^{-1}, $d = 4.9 - 8.3$ kpc).

Therefore, from a comparison between the observed and the expected fluxes we can exclude the presence of a circumstellar disk. The good agreement between observed and calculated fluxes favours the presence of a supergiant in IGR J16418-4532. However, the accretion from the polar wind of a main sequence/giant star with extreme properties (i.e. $v_\infty > 600$ km s^{-1} and $\dot{M} < 10^{-8}$ M$_\odot$ yr^{-1}) cannot be excluded.

We also investigated the possibility that the low-luminosity level at phase $\phi \sim 0$ in Figure 6.2 is due to an orbital modulation produced by an eccentric orbit, eventually with the onset of the centrifugal inhibition of accretion at apastron. If the orbit is eccentric, the onset of the centrifugal inhibition of accretion may occurr at apastron, where the wind is less dense and has a larger velocity than at periastron because of the continuity Equation (1.14) and the β-velocity law (Equation 1.28). This lead to a much stronger X-ray variability of the source related to the orbital motion than expected in the case of direct wind accretion. We calculated the X-ray lightcurves for the three cases O8.5 V−III−I within the Bondi-Hoyle accretion theory. Then, we compared these lightcurves with the lightcurve of IGR J16418-4532 obtained by folding the IBIS/ISGRI lightcurve with the orbital period 3.7381 d. The lightcurve obtained (Figure 6.9) does not show evidence of modulation (excluding the phase around $\phi \approx 0$), thus the orbit is likely to have a low eccentricity. The observed and calculated lightcurves are in agreement (i.e. similar X-ray luminosities along the orbit, and similar time duration of the region with low flux) only when we assumed an X-ray binary system composed by a supergiant (with $\dot{M} = 2 \times 10^{-6}$ M$_\odot$ yr^{-1}, $v_\infty = 1800$ km s^{-1}, $\beta = 1$, see Vink et al. 2000), an eccentricity in the range

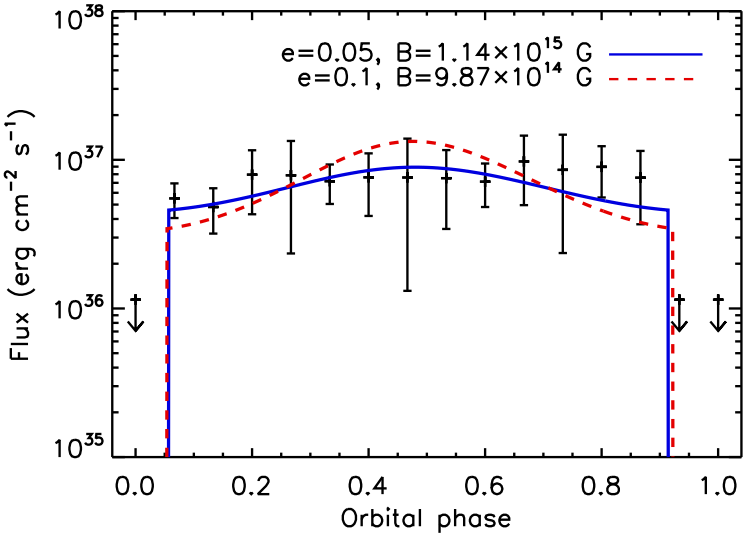

Figure 6.9: Comparison between the IBIS/ISGRI lightcurve of IGR J16418-4532 folded with the period 3.7381 d and the calculated lightcurves (assuming the presence of a supergiant in the binary system), for which we have considered the effect of the centrifugal inhibition of accretion. We derived the $1-100$ keV luminosities of the folded lightcurve by means of the spectral parameters found by fitting simultaneously the IBIS/ISGRI and JEM-X data (see Section 6.2.2). We found a good agreement (i.e. similar X-ray luminosities and similar time duration of the region with low-level luminosity) assuming that the primary star is a supergiant with $\dot{M} = 2\times10^{-6}$ M$_\odot$ yr^{-1}, $v_\infty = 1800$ km s^{-1}, $\beta = 1$, $9.87\times10^{14} \lesssim B \lesssim 1.14\times10^{15}$ G, and eccentricity $0.05 \lesssim e \lesssim 0.1$.

$0.05 \lesssim e \lesssim 0.1$ and a magnetic field for the neutron star of $B \approx 10^{15}$ G (see Figure 6.9). In the other cases (direct accretion along the whole orbit, binary system composed by a main sequence/giant star) we cannot reproduce the observed lightcurve.

6.4 Conclusions

We obtained a refined estimate of the orbital period of IGR J16418-4532 using the *Swift*/BAT lightcurve and we confirmed the presence of a region with low flux, probably due to an eclipse or due to the onset of the centrifugal inhibition of accretion.

Then we found a spin period of $P_{\rm spin} = 1213.5 \pm 1$ s in the IBIS/ISGRI lightcurve ($15-40$ keV) during the *INTEGRAL* revolution 468, with a probability of chance detection of 1.38436×10^{-6}. This measurement improves the previous estimate for the spin period found by Walter et al. (2006).

Assuming that the time interval with low luminosity at $\phi \approx 0$ in Figure 6.2 is due to an eclipse, we found that it is possible to exclude the presence of a O8.5 V star in IGR J16418-4532. Then, we investigated the hypothesis that the region with low luminosity at $\phi \approx 0$ is due to the onset of the centrifugal inhibition of accretion at apastron (assuming an eccentric orbit). In this case we found that the observed lightcurve can be explained assuming a O8.5 supergiant, a low eccentricity $e \lesssim 0.1$ and a neutron star magnetic field of the order of $B \approx 10^{15}$ G. A clear observational evidence for the presence of neutron stars with such high magnetic fields is still missing. However, several authors investigated the possibility that wind-fed HMXBs can host a magnetar with long spin period ($\gtrsim 10^3$ s; see e.g. Zhang et al. 2004a), and at present, a few known wind-fed HMXBs have been proposed to host a magnetar (see e.g. Finger et al. 2010).

Conclusions

During my PhD I studied the new class of Supergiant Fast X-ray Transients (SFXTs), mainly with *INTEGRAL* observations, and I explored the accretion mechanisms involved in these sources.

In this thesis I described the new clumpy wind model for OB supergiants, with both spherical and non-spherical geometry, that I developed to investigate the resulting effects of the accretion of an inhomogeneous wind onto a neutron star in HMXBs, and in particular in SFXTs. I introduced a distribution for the masses and initial dimensions of the clumps and I found that the clump size increases with the distance from the supergiant star. Then, for each mass of the clump, I derived the upper-limit and the lower-limit for the clump radius. From the calculated integral distributions (Section 4.4) I found that the observable characteristics of the flares, such as luminosity, durations, number of flares produced, do not depend only on the orbital parameters, but can be significantly affected by the properties of the clumps, in particular the scaling parameter ζ of the power-law distribution for the clump mass, and the fraction f of wind mass in the form of clumps. I successfully applied the clumpy wind model to four different HMXBs: Vela X-1, 4U 1700-377, IGR J11215-5952, and IGR J18483-0311. For IGR J11215-5952 I introduced a denser equatorial component, still with a clumpy structure, in order to reproduce the flare duration (according to the geometry suggested by Sidoli et al. 2007). I found that the X-ray luminosity and variability properties of these sources can be reproduced assuming similar mass distributions ($\zeta \approx 1.1 - 1.2$) and fraction of mass lost in clumps ($f = 0.75$). Moreover, I found that the values of the total mass loss rate $\dot{M}_{\rm tot}$ that best reproduce the observed lightcurves of the four sources studied are in agreement with the hypothesis that the mass loss rates derived by the Hα are overestimated by a factor 3-10. The different values of γ, $M_{\rm a}$, $M_{\rm b}$, obtained for the four HMXBs studied reveal that, in the framework of our clumpy wind model, the properties of the clumps of these sources are slightly different, independently of the orbital period. This discrepancy could be due to the different spectral type of the four supergiants, which could eject structurally inhomo-

geneous winds with slightly different properties. This hypothesis seems to be confirmed by the similar clumpy wind properties obtained for Vela X-1 and IGR J18483-0311, both hosting a B0.5 supergiant. I modelled an X-ray binary system to show a possible orbital configuration able to explain the outburst recurrence in SFXTs (following Sidoli et al. 2007). The configuration consists of an equatorial region with enhanced density, inclined to the plane of the neutron star orbit. The orbital plane intersects the equatorial wind component at two phases, producing two outbursts. A third outburst is produced at the periastron passage. This geometrical configuration has been used by Drave et al. (2010) to interpret the shape of the lightcurve of XTE J1739-302 folded on the orbital period, which shows three peaks (Figure 2.4).

Then I carried out a systematic analysis of all *INTEGRAL* observations from 2003 to 2009 of 14 SFXTs (confirmed and candidates), implying a net exposure time of about 30 Ms. This analysis led to discover several new outbursts from SFXTs. I discussed the effects of X-ray photoionization on the accretion in SFXTs, showing that the X−ray photoionization reduces the mass loss rate and the wind velocity towards the compact object with respect to the undisturbed case. Their simultaneous reduction leads to X−ray luminosities in agreement with those observed during the flaring activity; moreover, a lower wind velocity allows the formation of transient accretion disks from the capture of angular momentum, able to reproduce the quasi−periodic recurrent flares observed in some SFXTs.

The *INTEGRAL* analysis of these SFXTs has allowed to place constraints on the total population number of SFXTs in our Galaxy. Adopting a Bayesian inference method, I found that there could be up to $\approx 100^{+200}_{-70}$ SFXTs in our Galaxy: this result shows that SFXTs could be the dominant class of X-ray binaries with supergiants in our Galaxy.

I studied the HMXB IGR J16418-4532, for which I obtained a refined estimate of the orbital period of IGR J16418-4532 using the *Swift*/BAT lightcurve and I confirmed the presence of a time interval (with a duration of ~ 0.5 d) with low flux, probably due to an eclipse or due to the onset of the centrifugal inhibition of accretion. Then I found a spin period of $P_{\rm spin} = 1213.5 \pm 1$ s in the IBIS/ISGRI lightcurve (15-40 keV) of this source, with a probability of chance detection of 1.38436×10^{-6}. This measurement improves the previous estimate for the spin period found by Walter et al. (2006). From considerations involving the expected X-ray luminosities, the duration of the likely eclipse, and the onset of the centrifugal inhibition of accretion, I found that in all these cases it is possible to exclude the presence of a main sequence star, and the presence of a supergiant is favoured.

Appendix A

List of Publications

Reviewed publications:

• **Ducci L.**, Sidoli L., Paizis A., 2010, MNRAS accepted, arXiv:1006.3256: *INTEGRAL results on supergiant fast X-ray transients and accretion mechanism interpretation: ionization effect and formation of transient accretion discs*

• **Ducci L.**, Sidoli L., Mereghetti S., Paizis A., Romano P., 2009, MNRAS 398, 2152: *The structure of blue supergiant winds and the accretion in supergiant High Mass X-ray Binaries*

• Sguera V., **Ducci L.**, Sidoli L., Bazzano A., Bassani L., 2009, MNRAS 402, 49: *XMM-Newton and INTEGRAL study of the SFXT IGR J18483-0311 in quiescence: hint of a cyclotron emission feature?*

• Sidoli L., Esposito P., **Ducci L.**, 2010, MNRAS accepted, arXiv:1007.1091: *The longest observation of a low intensity state from a Supergiant Fast X-ray Transient: Suzaku observes IGRJ08408-4503*

• Romano P., Sidoli L., **Ducci L.**, Cusumano G., La Parola V., Pagani C., Page K. L., Kennea J. A., et al. 2009, MNRAS 401, 1564: *Swift/XRT monitoring of the Supergiant Fast X-ray Transient IGR J18483-0311 for an entire orbital period*

• Sidoli L., Romano P., **Ducci L.**, Paizis A., Cusumano G., Mangano V., Krimm H. A., Vercellone S. et al. 2009, MNRAS 397, 1528: *Supergiant Fast X-ray Transients in outburst: new Swift observations of XTE J1739-302, IGR J17544-2619, and IGR J08408-4503*

• Romano P., Sidoli L., Cusumano G., Evans P. A., **Ducci L.**, Krimm H. A., Vercellone S. et al. 2009, MNRAS 392, 45: *Multiple flaring activity in the supergiant fast X-ray transient IGR J08408-4503 observed with Swift*

• Romano P., Sidoli L., Cusumano G., La Parola V., Vercellone S., Pagani C., **Ducci L.**, Mangano V., Cummings J. et al. 2009, MNRAS 399, 2021:

Monitoring supergiant fast X-ray transients with Swift: results from the first year

Proceedings:

• **Ducci L.**, Sidoli L., Paizis A., Mereghetti S., Romano P., 2010, Proceedings of "The Extreme Sky: Sampling the Universe above 10 keV", Otranto, arXiv:1004.1896: *The role of structured OB supergiant winds in producing the X-ray flaring emission from High Mass X-ray Binaries*

• **Ducci L.**, Sidoli L., Mereghetti S., Romano P., Paizis A., 2010, AIPC 1248, 15, Proceeding of X-ray Astronomy 2009, Bologna, *Accretion of clumpy wind in supergiant HMXBs*

• **Ducci L.**, Sidoli L., Romano P., Paizis A., Mereghetti S., 2010, Proceedings of 'The Shocking Universe', Venice, arXiv:1003.5829: *The X-ray flaring emission from High Mass X-ray Binaries: the effects of wind inhomogeneities*

• **Ducci L.**, Sidoli L., Paizis A., Mereghetti S., 2008, Proceedings of the 7th INTEGRAL Workshop, arXiv:0810.5463: *Supergiant Fast X-ray Transients: interpretation of archival INTEGRAL data*

• **Ducci L.**, Sidoli L., Paizis A., Mereghetti S., Pizzochero P.M., 2008, Proceedings of the 7th INTEGRAL Workshop, arXiv:0810.5453: *INTEGRAL observes the 2007 outburst of the Be transient SAX J2103.5+4545*

• La Parola V., **Ducci L.**, Romano P., Sidoli L., Cusumano G., Vercellone S., Mangano V., Kennea J. A., et al., 2010, AIPC 1248, 177, Proceeding of X-ray Astronomy 2009, Bologna, arXiv:1001.3588: *The Swift SFXT monitoring campaign: the IGR J16479-4514 outburst in 2009*

• Sidoli L., Romano P., **Ducci L.**, Paizis A., Vercellone S., Cusumano G., La Parola V., Mangano V., et al., 2010, Proceedings of "The Extreme Sky: Sampling the Universe above 10 keV", Otranto, arXiv:1001.2407: *New results with Swift on Supergiant Fast X-ray Transients*

• Sidoli L., Romano P., **Ducci L.**, Paizis A., Vercellone S., Cusumano G., La Parola V., Mangano V., et al., 2010, AIPC 1248, 89, Proceeding of X-ray Astronomy 2009, Bologna, arXiv:1001.1670: *The Swift view of Supergiant Fast X-ray Transients*

• Romano P., Sidoli L., Cusumano G., La Parola V., Kennea J. A., Vercellone S., **Ducci L.** et al., 2010, Proceedings of 'The Shocking Universe', Venice, arXiv:1003.3041: *Supergiant fast X-ray transients: the Swift monitoring program*

Bibliography

Abbott, D. C. 1982, ApJ, 259, 282

Ables, J. G. 1968, Proceedings of the Astronomical Society of Australia, 1, 172

Angelini, L., Stella, L., & Parmar, A. N. 1989, ApJ, 346, 906

Ankay, A., Kaper, L., de Bruijne, J. H. J., et al. 2001, A&A, 370, 170

Arons, J. & Lea, S. M. 1976, ApJ, 207, 914

Bamba, A., Yokogawa, J., Ueno, M., Koyama, K., & Yamauchi, S. 2001, PASJ, 53, 1179

Barthelmy, S. D., Barbier, L. M., Cummings, J. R., et al. 2005, Space Science Reviews, 120, 143

Becker, P. A. & Wolff, M. T. 2005, ApJ, 630, 465

Becker, P. A. & Wolff, M. T. 2007, ApJ, 654, 435

Bildsten, L., Chakrabarty, D., Chiu, J., et al. 1997, ApJS, 113, 367

Bird, A. J., Bazzano, A., Bassani, L., et al. 2010, ApJS, 186, 1

Bird, A. J., Bazzano, A., Hill, A. B., et al. 2009, MNRAS, 393, L11

Blondin, J. M., Kallman, T. R., Fryxell, B. A., & Taam, R. E. 1990, ApJ, 356, 591

Blondin, J. M. & Pope, T. C. 2009, ApJ, 700, 95

Bondi, H. 1952, MNRAS, 112, 195

Bondi, H. & Hoyle, F. 1944, MNRAS, 104, 273

Bouret, J.-C., Lanz, T., & Hillier, D. J. 2005, A&A, 438, 301

Bozzo, E., Falanga, M., & Stella, L. 2008a, ApJ, 683, 1031

Bozzo, E., Stella, L., Israel, G., Falanga, M., & Campana, S. 2008b, MNRAS, 391, L108

Brown, G. E., Weingartner, J. C., & Wijers, R. A. M. J. 1996, ApJ, 463, 297

Brucato, R. J. & Kristian, J. 1972, ApJL, 173, L105+

Burrows, D. N., Hill, J. E., Nousek, J. A., et al. 2005, Space Science Reviews, 120, 165

Campana, S., Gastaldello, F., Stella, L., et al. 2001, ApJ, 561, 924

Campana, S., Stella, L., Mereghetti, S., & Colpi, M. 1995, A&A, 297, 385

Carlberg, R. G. 1980, ApJ, 241, 1131

Castor, J. I., Abbott, D. C., & Klein, R. I. 1975, ApJ, 195, 157

Chaty, S., Rahoui, F., Foellmi, C., et al. 2008, A&A, 484, 783

Chernyakova, M., Lutovinov, A., Capitanio, F., Lund, N., & Gehrels, N. 2003, The Astronomer's Telegram, 157, 1

Clark, D. J., Hill, A. B., Bird, A. J., et al. 2009, MNRAS, 399, L113

Clark, D. J., Sguera, V., Bird, A. J., et al. 2010, MNRAS, 406, L75

Clark, J. S., Goodwin, S. P., Crowther, P. A., et al. 2002, A&A, 392, 909

Coe, M. J., Fabregat, J., Negueruela, I., Roche, P., & Steele, I. A. 1996, MNRAS, 281, 333

Corbet, R., Barbier, L., Barthelmy, S., et al. 2006, The Astronomer's Telegram, 779, 1

Courvoisier, T., Walter, R., Beckmann, V., et al. 2003, A&A, 411, L53

Dalton, W. W. & Sarazin, C. L. 1995, ApJ, 440, 280

Davidson, K. & Ostriker, J. P. 1973, ApJ, 179, 585

Di Cocco, G., Caroli, E., Celesti, E., et al. 2003, A&A, 411, L189

Dicke, R. H. 1968, ApJL, 153, L101+

Drave, S. P., Clark, D. J., Bird, A. J., et al. 2010, ArXiv e-prints

Ducci, L., Sidoli, L., Mereghetti, S., Paizis, A., & Romano, P. 2009, MNRAS, 398, 2152

Ducci, L., Sidoli, L., & Paizis, A. 2010, MNRAS, 1262

Edgar, R. 2004, New Astronomy Review, 48, 843

Eggleton, P. P. 1983, ApJ, 268, 368

Elsner, R. F. & Lamb, F. K. 1977, ApJ, 215, 897

Fenimore, E. E. & Cannon, T. M. 1978, Applied Optics, 17, 337

Finger, M. H., Ikhsanov, N. R., Wilson-Hodge, C. A., & Patel, S. K. 2010, ApJ, 709, 1249

Fransson, C. & Fabian, A. C. 1980, A&A, 87, 102

Gehrels, N., Chincarini, G., Giommi, P., et al. 2004, ApJ, 611, 1005

Giunta, A., Bozzo, E., Bernardini, F., et al. 2009, MNRAS, 399, 744

Goldwurm, A., David, P., Foschini, L., et al. 2003, A&A, 411, L223

Gonzalez-Riestra, R., Santos-Lleo, M., Tomas, L., & Perez-Martinez, R. 2003, IAU Circ., 8202, 2

Gottesman, S. R. & Fenimore, E. E. 1989, Applied Optics, 28, 4344

Gotz, D., Mereghetti, S., Mowlavi, N., & Soldan, J. 2004, GRB Coordinates Network, 2793, 1

Gotz, D., Schanne, S., Rodriguez, J., et al. 2006, The Astronomer's Telegram, 813, 1

Grebenev, S. A. & Sunyaev, R. A. 2007, Astronomy Letters, 33, 149

Grimm, H., Gilfanov, M., & Sunyaev, R. 2002, A&A, 391, 923

Haberl, F. 1994, A&A, 288, 791

Haberl, F. & White, N. E. 1990, ApJ, 361, 225

Haberl, F., White, N. E., & Kallman, T. R. 1989, ApJ, 343, 409

Halpern, J. P., Gotthelf, E. V., Helfand, D. J., Gezari, S., & Wegner, G. A. 2004, The Astronomer's Telegram, 289, 1

Hamann, W.-R., Feldmeier, A., & Oskinova, L. M., eds. 2008, Clumping in hot-star winds

Hatchett, S. & McCray, R. 1977, ApJ, 211, 552

Heindl, W. A., Coburn, W., Gruber, D. E., et al. 1999, ApJL, 521, L49

Henrichs, H. F. 1983, in Accretion-Driven Stellar X-ray Sources, ed. W. H. G. Lewin & E. P. J. van den Heuvel, 393–429

Ho, C. & Arons, J. 1987, ApJ, 316, 283

Horne, J. H. & Baliunas, S. L. 1986, ApJ, 302, 757

Howarth, I. D., Prinja, R. K., Roche, P. F., & Willis, A. J. 1984, MNRAS, 207, 287

Howk, J. C., Cassinelli, J. P., Bjorkman, J. E., & Lamers, H. J. G. L. M. 2000, ApJ, 534, 348

Hoyle, F. & Lyttleton, R. A. 1939, in Proceedings of the Cambridge Philosophical Society, Vol. 34, Proceedings of the Cambridge Philosophical Society, 405

Illarionov, A. F. & Sunyaev, R. A. 1975, A&A, 39, 185

in 't Zand, J., Heise, J., Smith, M., et al. 1998, IAU Circ., 6840, 2

in't Zand, J. J. M. 2005, A&A, 441, L1

Jain, C., Paul, B., & Dutta, A. 2009, MNRAS, 397, L11

Jensen, P. L., Clausen, K., Cassi, C., et al. 2003, A&A, 411, L7

Jetzer, P., Strassle, M., & Straumann, N. 1998, New Astronomy, 3, 619

Jones, C., Forman, W., Tananbaum, H., et al. 1973, ApJL, 181, L43+

Kallman, T. R. & McCray, R. 1982, ApJS, 50, 263

Kaper, L., Hammerschlag-Hensberge, G., & Zuiderwijk, E. J. 1994, A&A, 289, 846

King, A. 1995, in X-ray Binaries, ed. W. H. G. Lewin, J. van Paradijs, & E. P. J. van den Heuvel, 419–456

Kinugasa, K., Torii, K., Hashimoto, Y., et al. 1998, ApJ, 495, 435

Kreykenbohm, I., Wilms, J., Kretschmar, P., et al. 2008, A&A, 492, 511

Krimm, H. A., Barthelmy, S. D., Markwardt, C. B., et al. 2006, in Bulletin of the American Astronomical Society, Vol. 38, Bulletin of the American Astronomical Society, 374–+

Kudritzki, R. P., Pauldrach, A., Puls, J., & Abbott, D. C. 1989, A&A, 219, 205

Kudritzki, R.-P. & Puls, J. 2000, Annu. Rev. Astro. Astrophys., 38, 613

La Parola, V., Cusumano, G., Romano, P., et al. 2010, MNRAS, 405, L66

Lamb, F. K., Fabian, A. C., Pringle, J. E., & Lamb, D. Q. 1977, ApJ, 217, 197

Lamers, H. J. G. L. M. & Cassinelli, J. P. 1999, Introduction to Stellar Winds (Introduction to Stellar Winds, by Henny J. G. L. M. Lamers and Joseph P. Cassinelli, pp. 452. ISBN 0521593980. Cambridge, UK: Cambridge University Press, June 1999.)

Lamers, H. J. G. L. M. & Waters, L. B. F. M. 1987, A&A, 182, 80

Leahy, D. A. 2002, A&A, 391, 219

Leahy, D. A. & Kostka, M. 2008, MNRAS, 384, 747

Lebrun, F., Leray, J. P., Lavocat, P., et al. 2003, A&A, 411, L141

Lefever, K., Puls, J., & Aerts, C. 2007, A&A, 463, 1093

Lépine, S. & Moffat, A. F. J. 2008, Astronomical Journal, 136, 548

Levine, A. M., Bradt, H. V., Chakrabarty, D., Corbet, R. H. D., & Harris, R. J. 2010, ArXiv e-prints

Levine, A. M. & Corbet, R. 2006, The Astronomer's Telegram, 940, 1

Leyder, J., Walter, R., Lazos, M., Masetti, N., & Produit, N. 2007, A&A, 465, L35

Liu, Q. Z., van Paradijs, J., & van den Heuvel, E. P. J. 2006, A&A, 455, 1165

Lomb, N. R. 1976, Astrophysics and Space Science, 39, 447

Longair, M. S. 1994, High energy astrophysics. Volume 2. Stars, the Galaxy and the interstellar medium., ed. Longair, M. S. (Cambridge University Press, Cambridge (UK), 1994, 410 p., ISBN 0-521-43439-4)

Lubinski, P., Bel, M. G., von Kienlin, A., et al. 2005, The Astronomer's Telegram, 469, 1

Lucy, L. B. & Solomon, P. M. 1970, ApJ, 159, 879

Lucy, L. B. & White, R. L. 1980, ApJ, 241, 300

Lund, N., Budtz-Jørgensen, C., Westergaard, N. J., et al. 2003, A&A, 411, L231

Lutovinov, A., Revnivtsev, M., Gilfanov, M., et al. 2005, A&A, 444, 821

Lutovinov, A., Rodrigues, J., Budtz-Jorgensen, C., Grebenev, S., & Winkler, C. 2004, The Astronomer's Telegram, 329, 1

MacGregor, K. B. & Vitello, P. A. J. 1982, ApJ, 259, 267

Makishima, K., Ohashi, T., Hayashida, K., et al. 1989, PASJ, 41, 697

Maraschi, L., Treves, A., & van den Heuvel, E. P. J. 1976, Nature, 259, 292

Markova, N., Prinja, R. K., Markov, H., et al. 2008, A&A, 487, 211

Markwardt, C. B., Swank, J. H., & Marshall, F. E. 1999, IAU Circ., 7120, 1

Martins, F., Schaerer, D., & Hillier, D. J. 2005, A&A, 436, 1049

Mas-Hesse, J. M., Giménez, A., Culhane, J. L., et al. 2003, A&A, 411, L261

Masetti, N., Mason, E., Morelli, L., et al. 2008, A&A, 482, 113

Masetti, N., Pretorius, M. L., Palazzi, E., et al. 2006, A&A, 449, 1139

Matsuda, T., Inoue, M., & Sawada, K. 1987, MNRAS, 226, 785

Meszaros, P. 1984, Space Science Reviews, 38, 325

Mészáros, P. 1992, High-energy radiation from magnetized neutron stars., ed. Mészáros, P. (University of Chicago Press, Chicago, IL (USA), 1992, 544 p., ISBN 0-226-52093-5)

Molkov, S., Mowlavi, N., Goldwurm, A., et al. 2003, The Astronomer's Telegram, 176, 1

Motch, C., Stella, L., Janot-Pacheco, E., & Mouchet, M. 1991, ApJ, 369, 490

Muno, M. P., Gaensler, B. M., Nechita, A., Miller, J. M., & Slane, P. O. 2008, ApJ, 680, 639

Negueruela, I. & Smith, D. M. 2006, The Astronomer's Telegram, 831, 1

Negueruela, I., Smith, D. M., & Chaty, S. 2005, The Astronomer's Telegram, 429, 1

Negueruela, I., Smith, D. M., Harrison, T. E., & Torrejón, J. M. 2006b, ApJ, 638, 982

Negueruela, I., Smith, D. M., Reig, P., Chaty, S., & Torrejón, J. M. 2006a, in ESA Special Publication, Vol. 604, The X-ray Universe 2005, ed. A. Wilson, 165

Negueruela, I., Smith, D. M., Torrejon, J. M., & Reig, P. 2007, ArXiv e-prints

Negueruela, I., Torrejón, J. M., Reig, P., Ribó, M., & Smith, D. M. 2008, in American Institute of Physics Conference Series, Vol. 1010, A Population Explosion: The Nature & Evolution of X-ray Binaries in Diverse Environments, ed. R. M. Bandyopadhyay, S. Wachter, D. Gelino, & C. R. Gelino, 252–256

Nespoli, E., Fabregat, J., & Mennickent, R. 2007, The Astronomer's Telegram, 982, 1

Nespoli, E., Fabregat, J., & Mennickent, R. E. 2008, A&A, 486, 911

Orlandini, M., dal Fiume, D., Frontera, F., et al. 1998, A&A, 332, 121

Orr, A., Torrejón, J. M., & Parmar, A. N. 2004, in ESA Special Publication, Vol. 552, 5th INTEGRAL Workshop on the INTEGRAL Universe, ed. V. Schoenfelder, G. Lichti, & C. Winkler, 361

Oskinova, L. M., Hamann, W.-R., & Feldmeier, A. 2007, A&A, 476, 1331

Owocki, S. P., Castor, J. I., & Rybicki, G. B. 1988, ApJ, 335, 914

Parmar, A. N., White, N. E., Stella, L., Izzo, C., & Ferri, P. 1989, ApJ, 338, 359

Pauldrach, A., Puls, J., & Kudritzki, R. P. 1986, A&A, 164, 86

Pellizza, L. J., Chaty, S., & Negueruela, I. 2006, A&A, 455, 653

Perna, R., Bozzo, E., & Stella, L. 2006, ApJ, 639, 363

Pfahl, E., Rappaport, S., Podsiadlowski, P., & Spruit, H. 2002, ApJ, 574, 364

Puls, J., Kudritzki, R.-P., Herrero, A., et al. 1996, A&A, 305, 171

Raguzova, N. V. & Lipunov, V. M. 1998, A&A, 340, 85

Rahoui, F. & Chaty, S. 2008, A&A, 492, 163

Rahoui, F., Chaty, S., Lagage, P.-O., & Pantin, E. 2008, A&A, 484, 801

Rappaport, S. A. & Joss, P. C. 1983, in Accretion-Driven Stellar X-ray Sources, ed. W. H. G. Lewin & E. P. J. van den Heuvel, 1–39

Reig, P. 2007, MNRAS, 377, 867

Reig, P., Negueruela, I., Buckley, D. A. H., et al. 2001, A&A, 367, 266

Reig, P. & Roche, P. 1999, MNRAS, 306, 100

Reynolds, A. P., Owens, A., Kaper, L., Parmar, A. N., & Segreto, A. 1999, A&A, 349, 873

Romano, P., Sidoli, L., Cusumano, G., et al. 2009a, MNRAS, 392, 45

Romano, P., Sidoli, L., Cusumano, G., et al. 2009b, MNRAS, 399, 2021

Romano, P., Sidoli, L., Cusumano, G., et al. 2009c, ArXiv e-prints

Romano, P., Sidoli, L., Ducci, L., et al. 2010, MNRAS, 401, 1564

Romano, P., Sidoli, L., Mangano, V., Mereghetti, S., & Cusumano, G. 2007, A&A, 469, L5

Romano, P., Sidoli, L., Mangano, V., et al. 2008, ApJL, 680, L137

Roming, P. W. A., Kennedy, T. E., Mason, K. O., et al. 2005, Space Science Reviews, 120, 95

Rubin, B. C., Finger, M. H., Harmon, B. A., et al. 1996, ApJ, 459, 259

Ruffert, M. 1999, A&A, 346, 861

Runacres, M. C. & Owocki, S. P. 2002, A&A, 381, 1015

Russeil, D. 2003, A&A, 397, 133

Sadakane, K., Hirata, R., Jugaku, J., et al. 1985, ApJ, 288, 284

Sako, M., Liedahl, D. A., Kahn, S. M., & Paerels, F. 1999, ApJ, 525, 921

Scargle, J. D. 1982, ApJ, 263, 835

Schönherr, G., Wilms, J., Kretschmar, P., et al. 2007, A&A, 472, 353

Searle, S. C., Prinja, R. K., Massa, D., & Ryans, R. 2008, A&A, 481, 777

Sguera, V., Barlow, E. J., Bird, A. J., et al. 2005, A&A, 444, 221

Sguera, V., Bassani, L., Landi, R., et al. 2008, A&A, 487, 619

Sguera, V., Bazzano, A., Bird, A. J., et al. 2006, ApJ, 646, 452

Sguera, V., Ducci, L., Sidoli, L., Bazzano, A., & Bassani, L. 2010, MNRAS, 402, L49

Sguera, V., Hill, A. B., Bird, A. J., et al. 2007, A&A, 467, 249

Shapiro, S. L. & Lightman, A. P. 1976, ApJ, 204, 555

Shimada, M. R., Ito, M., Hirata, B., & Horaguchi, T. 1994, in IAU Symposium, Vol. 162, Pulsation; Rotation; and Mass Loss in Early-Type Stars, ed. L. A. Balona, H. F. Henrichs, & J. M. Le Contel, 487

Sidoli, L. 2009, Advances in Space Research, 43, 1464

Sidoli, L., Esposito, P., & Ducci, L. 2010, ArXiv e-prints

Sidoli, L., Paizis, A., & Mereghetti, S. 2006, A&A, 450, L9

Sidoli, L., Romano, P., Mangano, V., et al. 2009, ApJ, 690, 120

Sidoli, L., Romano, P., Mangano, V., et al. 2008, ApJ, 687, 1230

Sidoli, L., Romano, P., Mereghetti, S., et al. 2007, A&A, 476, 1307

Smart, W. M. 1965, Text-book on spherical astronomy (Cambridge: University Press, 1965/71, 5th ed.)

Smith, D. M., Bezayiff, N., & Negueruela, I. 2006a, The Astronomer's Telegram, 773, 1

Smith, D. M., Heindl, W. A., Markwardt, C. B., et al. 2006b, ApJ, 638, 974

Smith, D. M., Heindl, W. A., Swank, J. H., Harrison, T. E., & Negueruela, I. 2003, The Astronomer's Telegram, 182, 1

Smith, D. M., Main, D., Marshall, F., et al. 1998, ApJL, 501, L181+

Smith, D. M., Negueruela, I., Heindl, W. A., Markwardt, C. B., & Swank, J. H. 2004, in Bulletin of the American Astronomical Society, Vol. 36, Bulletin of the American Astronomical Society, 954–+

Snow, Jr., T. P. 1981, ApJ, 251, 139

Stella, L., Campana, S., Colpi, M., Mereghetti, S., & Tavani, M. 1994, ApJL, 423, L47

Stevens, I. R. 1988, MNRAS, 232, 199

Stevens, I. R. 1991, ApJ, 379, 310

Stevens, I. R. & Kallman, T. R. 1990, ApJ, 365, 321

Stoyanov, K. A. & Zamanov, R. K. 2009, Astronomische Nachrichten, 330, 727

Sunyaev, R., Lutovinov, A., Molkov, S., & Deluit, S. 2003a, The Astronomer's Telegram, 181, 1

Sunyaev, R. A., Grebenev, S. A., Lutovinov, A. A., et al. 2003b, The Astronomer's Telegram, 190, 1

Swank, J. H., Smith, D. M., & Markwardt, C. B. 2007, The Astronomer's Telegram, 999, 1

Taam, R. E., Brown, D. A., & Fryxell, B. A. 1988, ApJL, 331, L117

Tarter, C. B., Tucker, W. H., & Salpeter, E. E. 1969, ApJ, 156, 943

Tauris, T. M. & van den Heuvel, E. 2003, ArXiv Astrophysics e-prints

Tomsick, J. A., Chaty, S., Rodriguez, J., et al. 2006, ApJ, 647, 1309

Tomsick, J. A., Lingenfelter, R., Corbel, S., Goldwurm, A., & Kaaret, P. 2004, The Astronomer's Telegram, 224, 1

Torii, K., Kinugasa, K., & Kitamoto, S. 1997, IAU Circ., 6678, 2

Trotta, R. 2008, Contemporary Physics, 49, 71

Truemper, J., Pietsch, W., Reppin, C., et al. 1978, ApJL, 219, L105

Ubertini, P., Lebrun, F., Di Cocco, G., et al. 2003, A&A, 411, L131

Ud-Doula, A., Owocki, S. P., & Townsend, R. H. D. 2008, MNRAS, 385, 97

Vacca, W. D., Garmany, C. D., & Shull, J. M. 1996, ApJ, 460, 914

van der Meer, A., Kaper, L., di Salvo, T., et al. 2005, A&A, 432, 999

van Kerkwijk, M. H., van Paradijs, J., Zuiderwijk, E. J., et al. 1995, A&A, 303, 483

Vedrenne, G., Roques, J., Schönfelder, V., et al. 2003, A&A, 411, L63

Vink, J. S., de Koter, A., & Lamers, H. J. G. L. M. 2000, A&A, 362, 295

Wainscoat, R. J., Cohen, M., Volk, K., Walker, H. J., & Schwartz, D. E. 1992, ApJS, 83, 111

Walborn, N. R. 1973, Astronomical Journal, 78, 1067

Walter, R., Bodaghee, A., Barlow, E. J., et al. 2004, The Astronomer's Telegram, 229, 1

Walter, R. & Zurita Heras, J. 2007, A&A, 476, 335

Walter, R., Zurita Heras, J., Bassani, L., et al. 2006, A&A, 453, 133

Wang, Y. 1981, A&A, 102, 36

Wang, Y. & Welter, G. L. 1981, A&A, 102, 97

Waters, L. B. F. M., de Martino, D., Habets, G. M. H. J., & Taylor, A. R. 1989, A&A, 223, 207

Waters, L. B. F. M., van den Heuvel, E. P. J., Taylor, A. R., Habets, G. M. H. J., & Persi, P. 1988, A&A, 198, 200

Wen, L., Levine, A. M., Corbet, R. H. D., & Bradt, H. V. 2006, ApJS, 163, 372

White, N. E., Kallman, T. R., & Swank, J. H. 1983, ApJ, 269, 264

Wijnands, R. 2003, The Astronomer's Telegram, 191, 1

Winkler, C., Courvoisier, T., Di Cocco, G., et al. 2003, A&A, 411, L1

Yamauchi, S., Aoki, T., Hayashida, K., et al. 1995, PASJ, 47, 189

Zarinelli, A., Walder, R., & Nussbaumer, H. 1995, A&A, 301, 922

Zel'Dovich, Y. B. & Shakura, N. I. 1969, Soviet Astronomy, 13, 175

Zhang, F., Li, X., & Wang, Z. 2004a, Chinese Journal of Astronomy & Astrophysics, 4, 320

Zhang, F., Li, X., & Wang, Z. 2004b, ApJ, 603, 663

Zurita Heras, J. A. & Chaty, S. 2009, A&A, 493, L1